Dark Matter γ-line search in the Galactic Centre with H.E.S.S. using an On-Off technique

Der Naturwissenschaftlichen Fakultät
der Friedrich-Alexander-Universität
Erlangen-Nürnberg

zur Erlangung des Doktorgrades Dr. rer. nat.

vorgelegt von

Johannes Veh

aus Berlin

Dark Matter γ-line search in the Galactic Centre with H.E.S.S. using an On-Off technique

Suche nach einem γ-Linien Signal von Dunkler Materie im Zentrum der Milchstraße mit H.E.S.S. unter Zuhilfenahme einer On-Off Analysetechnik

Als Dissertation genehmigt
von der Naturwissenschaftlichen Fakultät
der Friedrich-Alexander-Universität
Erlangen-Nürnberg

Tag der mündlichen Prüfung: 13.07.2018

Vorsitzender des Promotionsorgans: Herr Prof. Dr. Georg Kreimer

Gutachter: Prof. Dr. Christopher van Eldik

Dr. Henning Gast

Title page: Photo montage showing the gamma-ray sky over Namibia, as measured by H.E.S.S. telescopes during the last years, superimposed onto an optical image, with one of the small H.E.S.S. telescopes in the foreground (Credit: H.E.S.S. Collaboration, Fabio Acero https://www.mpi-hd.mpg.de/hfm/HESS/hgps/figures/hess_hgps_montage.jpg)

Dedicated to my mother

Martina Veh

Abstract

The High Energy Stereoscopic System (H.E.S.S.) is an Imaging Air Cherenkov Telescope located in Namibia. Since 2003 it has been taking data in its phase I configuration with four telescopes. In 2012 operation in phase II started with a much larger fifth telescope built in the centre of the array reducing the energy threshold. One of the scientific goals of H.E.S.S. is to search for Dark Matter. It is expected that a large amount of Dark Matter is located in a halo around the Galaxy with the highest density close to the centre. This makes the Galactic Centre a good target region for Dark Matter searches. If the Dark Matter particle mass is in the GeV to TeV range, H.E.S.S. might be able to find a signal of pair annihilating Dark Matter in γ rays. In this thesis a line-like signal from $\chi\chi \rightarrow \gamma\gamma$ was searched for. The exact shape of the Dark Matter distribution is unknown. Due to the chosen On-Off analysis technique it is possible to probe Cored and Cusped Dark Matter density distributions. With the chosen likelihood analysis it is possible to combine data from both phases of H.E.S.S. In this thesis upper limits on the velocity-weighted annihilation cross section using such a combined data set are shown for the first time. Furthermore, several systematic studies were performed to improve the understanding of data quality and the analysis results.

Kurzfassung

Das High Energy Stereoscopic System (H.E.S.S.) ist ein in Namibia aufgebautes System aus abbildenden Cherenkov-Teleskopen. Seit 2003 werden Daten in der ersten Ausbaustufe, bestehend aus vier Teleskopen, genommen. Im Jahr 2012 wurde der Betrieb in Phase zwei aufgenommen, in der ein weiteres, deutlich größeres Teleskop, welches die Energieschwelle reduziert, im Zentrum des Systems hinzugefügt wurde. Eines der wissenschaftlichen Ziele von H.E.S.S. ist es, die Natur von Dunkler Materie zu untersuchen. Es wird erwartet, dass eine große Menge an Dunkler Materie in einem galaktischen Halo in der Milchstraße existiert, mit besonders hoher Dichte nahe dem Zentrum der Galaxie. Dadurch ist es ein gutes Ziel für die Suchen nach Signalen von Dunkler Materie. Die Suche in dieser Region muss jedoch sehr behutsam durchgeführt werden, da viel γ-Strahlung durch astrophysikalische Quellen erzeugt wird. In dieser Arbeit wird nach einem linienartigen Signal aus Paarvernichtung ($\chi\chi \rightarrow \gamma\gamma$) gesucht. Wenn die Masse der Dunklen Materie-Teilchen im GeV- bis TeV-Bereich liegt, hat H.E.S.S. eine Chance, dieses Signal zu sehen. Die genaue Form des Dunkle-Materie-Halo ist unbekannt. Durch die in dieser Arbeit verwendete On-Off-Analyse ist es möglich, sowohl im Zentrum steil verlaufende als auch flache Dunkle-Materie-Dichte-Profile zu untersuchen. Mit der hier gewählten Maximum-Likelihood-Methode lässt sich, eine kombinierte Analyse von Daten aus beiden Phasen von H.E.S.S. erstellen. Mit dieser Analyse werden zum ersten Mal obere Limits für den geschwindigkeitsgemittelten Wirkungsquerschnitt mit einem kombinierten Datensatz errechnet. Des Weiteren wurden systematische Studien durchgeführt, um ein besseres Verständnis der Daten zu erhalten sowie die Ergebnisse besser verständlich zu machen.

Table of Contents

List of Figures

List of Tables

Chapter 1

Introduction

Since the discovery of cosmic rays by Victor Hess (Hess, 1912) we know that the universe is not only sending low energy photons towards the Earth but also charged particles and high energetic photons. While cosmic rays are deflected on their way to the Earth due to their charge, photons can be used to trace back to sources. Many experiments measured this radiation in different energy regimes trying to reveal these sources. One of these experiments is the High Energy Stereoscopic System (H.E.S.S.). With its approximate energy range of 0.1 – 100 TeV H.E.S.S. is able to detect γ-ray sources. Besides astrophysical sources such as PKS 2155–304 (an active galactic nucleus, Aharonian et al., 2005) or the Crab Nebula (a pulsar wind nebula, Aharonian et al., 2006b) H.E.S.S. can be used to search for a signal from self-annihilating Dark Matter. Physicists have been searching for Dark Matter for several decades to answer the question:

What is Dark Matter made of and how can we explain our observations with it?

It is predicted that two Dark Matter particles can annihilate each other. If they annihilate into a photon pair, a unique line-like signal with an energy equal to the Dark Matter particle mass is created. This unique signature can be distinguished from other sources of high-energy photons. It is also possible that a continuous photon spectrum is produced in the decay process of annihilation products. However this Dark Matter signature is not analysed within this work. Due to the rather faint expected signal the search is done either close to the Galactic Centre or at the direction of Dwarf galaxies. At these directions a high concentration of Dark Matter is predicted from simulations. H.E.S.S. took over 200 h of data close to the Galactic Centre. While the data from the first phase of H.E.S.S. was already analysed for a line-like signal (Abramowski et al., 2013) deriving upper limits for the velocity-weighted annihilation cross section, no results for the data from the second phase or an analysis combining data from both phases do yet exist.

Aim of this thesis

In this work I present my analysis of the Galactic Centre region using the advanced event reconstruction technique ImPACT (Parsons & Hinton, 2014), showing the first results of a Dark Matter line search combining data from both phases of H.E.S.S. In order to achieve this goal, an On-Off analysis technique was developed. This method was necessary to compensate the small field of

view of H.E.S.S. II and the resulting problem to find regions for background estimation in the Galactic Centre region due to the high density of γ-ray sources.
Furthermore a maximum Likelihood analysis was used, which made it possible to combine data from both phases of H.E.S.S.

Structure of the thesis

- An introduction to Dark Matter constraining observational evidence, candidates proposed by various theories, an overview of the Galactic Centre region and flux expectation for an indirect search.
- An introduction to Cherenkov Telescopes and a detailed description how H.E.S.S. data are analysed.
- A chapter describing the selection of data and systematic studies preparing the used On-Off analysis for the indirect Dark Matter search in the Galactic Centre.
- A summary of the used Likelihood analysis.
- Results of the analysis of the Galactic Centre data set.
- Followed by an outlook.

Chapter 2

Dark Matter

For a long time in human history celestial objects have been studied. In the early days astronomical observations were done with the naked eye, therefore limited to close and/or very bright objects. With the development of telescopes in the 16th century astronomers were for the first time able to study objects invisible to the human eye. The development of new techniques arose questions. With the introduction of Newton's laws of motion and their application to stellar motion within galaxies, astronomers noticed for the first time that the visible mass is not sufficient to explain the stars' observed velocities. This was first known as the missing mass problem and lead later to the introduction of Dark Matter.

In the following I will give a brief discussion of the history of Dark Matter physics mainly using the work of Bertone & Hooper (2016) as reference. Afterwards I will discuss the evidence for Dark Matter in more detail and conclude with possible explanations of their nature.

2.1 A short history of Dark Matter physics

It was in the middle of the 18th century when astronomers used Newton's laws to predict the position of undiscovered objects which led to the discovery of Neptune. In the following decades many more "dark objects" were discovered in the form of planets, stars and gas clouds. In 1933 Fritz Zwicky published a work on the coma cluster and stated that the observed velocities of galaxies within the cluster cannot be explained by the mass derived from the cluster's luminosity (Zwicky, 1933). He used the virial theorem as a relation between the kinetic energy and the potential energy of the galaxy cluster. According to his calculations, the mass needed to explain the gravitational pull was about 400 times higher than the mass estimated by the mass to luminosity ratio. An important assumption for this approach is that the cluster is in a steady state which is at least for the faster galaxies controversial. In that time various studies have been published by different scientists leading to the conclusion that non-luminous matter has to be in galaxy clusters, to be known as the missing mass problem. Later on the term Dark Matter was used to address the issue. By that time the predominant view was that Dark Matter consists of cold stars and gas (Zwicky, 1937).

Later on, Finzi (1963) ruled out the above mentioned Dark Matter candidates, and to explain the observations, proposed a modification of Newton's Laws to explain the experimental results. This extension of Newton's Laws is still discussed and today known as modified Newtonian dynamics (MOND). MOND is able to explain rotation curves of galaxies. However there are difficulties to describe systems like the Bullet cluster and effects like micro lensing.
The idea of non-baryonic Dark Matter arose in the 1980ies when the first supersymmetric theories predicted particles with fitting properties as Dark Matter candidates. With the first results from cosmological simulations of structure formation, from the early universe till today, and comparison with sky surveys (e.g. Centre for Astrophysics (CfA) Redshift Survey), it became clear that only non-relativistic particles (from here called Cold Dark Matter) can lead to the observed structures. Today the search for Dark Matter is mostly focussed on particles with the following properties:

- not electromagnetically interacting
- massive in order to be cold, i.e. non-relativistic
- possibly interacting with the weak force

A particle of this kind is called weakly interacting massive particle (WIMP). The standard model of particles does not provide a fitting candidate, but various extensions provide fitting candidates such as supersymmetry, Kaluza-Klein, sterile neutrinos and axions.

2.2 Evidence for Dark Matter

As already mentioned there is plenty of evidence for Dark Matter in our universe. They all come down to the argument that visible matter alone is unable to explain the observed gravitational pull.

2.2.1 Rotation curves of galaxies

With the assumption that stars are on stable orbits around the centre of their host galaxy, one can derive the gravitational pull, because it has to be equal to the centripetal force given by:

$$\begin{aligned} F_G &= F_C \\ G\frac{m_S m_G}{r^2} &= \frac{m_S v^2}{r} \end{aligned} \tag{2.1}$$

where r is the distance from the star with mass m_S to the galaxy centre, m_G the mass inside the radius r, G the gravitational constant and v the velocity of the star. Solving this equation for v gives the expression

$$v = \sqrt{\frac{Gm_G}{r}}. \tag{2.2}$$

Comparing this theoretical velocity distribution to observations, V. Rubin (see Figure 2.1; Rubin et al., 1980) noticed that for all 21 galaxies in their survey the velocity of stars is too high to keep

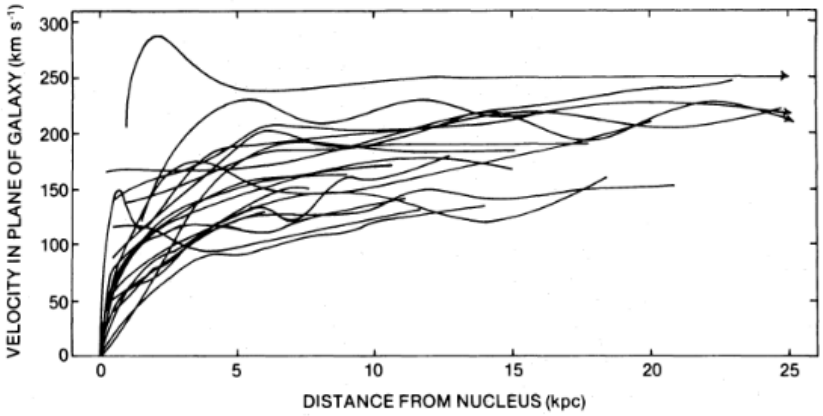

Figure 2.1: Superposition of the rotation curves of 21 galaxies. Outside the innermost part of galaxies the star velocity remains almost constant. This is in contradiction to the expectation of a declining velocity outside the innermost part (Rubin et al., 1980).

them on stable orbits and is almost constant as a function of distance from the centre outside the innermost part. To explain this observation the mass within a certain radius around the centre of the galaxy has to be proportional to r, i.e. $m(r) \sim r$. However, the luminosity of galaxies shows a different dependency which leads to the conclusion that the outer parts of galaxies must contain none luminous matter.

2.2.2 Gravitation lensing

Einstein described in his work about the general theory of relativity that light can be bent by gravity (Einstein, 1915). In a later work he calculated the order of the effect by considering two stars aligned with an observer. Einstein predicted that the image of the distant star will form a ring around the close star (Einstein, 1936). A sketch of the light rays can be seen in Figure 2.2.

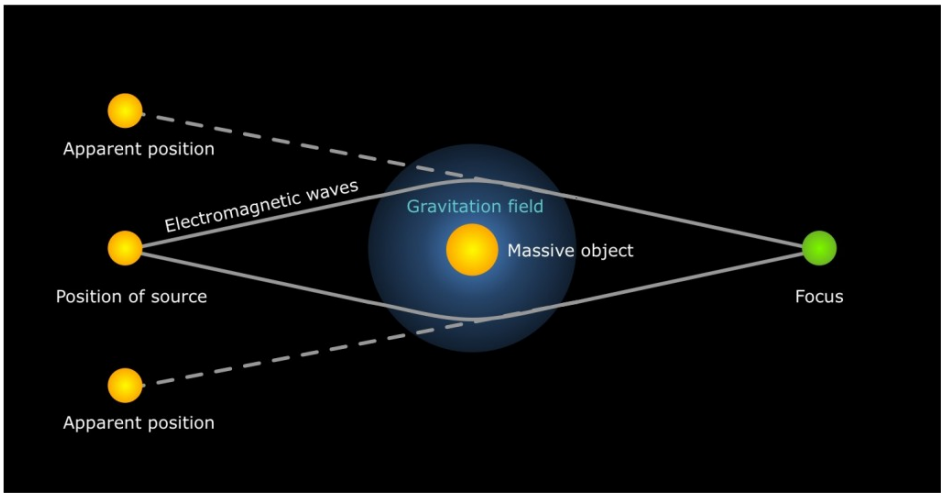

Figure 2.2: Sketch of gravitational lensing. The apparent light path is shown in dashed lines, the true path in continuous lines. Figure taken from Oneminuteastronomer[1].

[1] http://oneminuteastronomer.com/9237/gravitational-lens/

This phenomenon is known as Einstein ring. He came to the conclusion that the effect is too small to be observed. However, if the close object is not a star, but a galaxy or galaxy cluster, this light bending or gravitation lensing can be measured and used to determine the mass of the foreground object. Figure 2.3 shows an image of an observed Einstein Ring. If the objects are not in one line with the observer, the image of the background object will just be distorted. By the measurement of many background objects and a statistical analysis, the total mass and shape of the foreground object can be measured (Longair, 2011). Measurements of gravitational lensing provide additional evidence that there must be much more mass in the foregroung galaxies than expected from their luminosities.

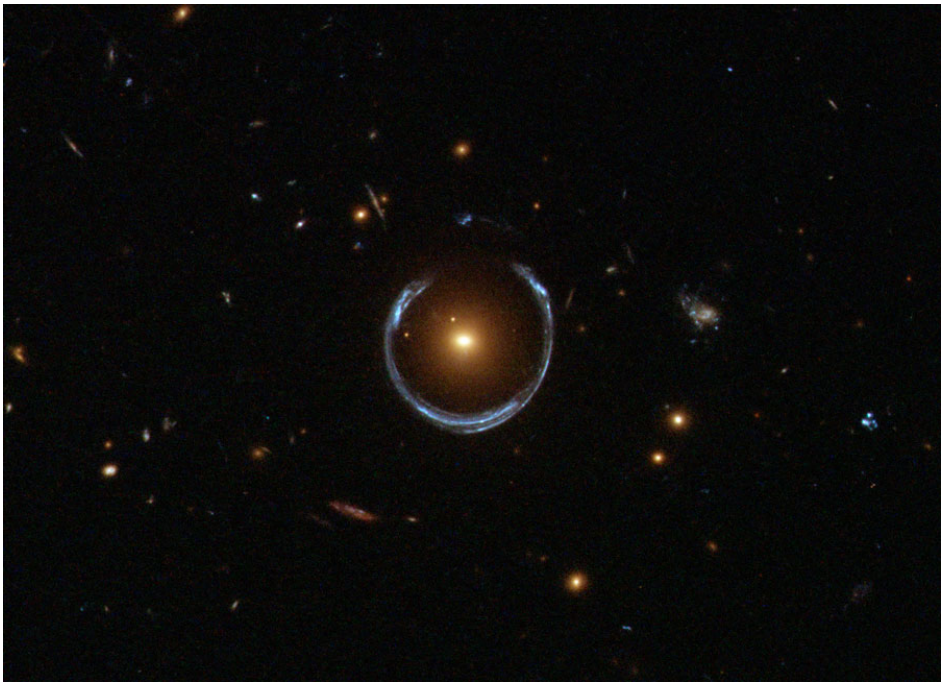

Figure 2.3: Hubble Space Telescope image of the galaxy LRG 3-757. Observing an almost closed Einstein Ring is very unlikely, since both galaxies and the observer have to be in one line. Image Credit: ESA/Hubble & NASA

The most remarkable object, where the mass distribution can be traced by gravitational lensing, is the Bullet Cluster. Clowe et al. (2006) published results of an analysis of the object 1E 0657-558, the Bullet Cluster. In this object two galaxy clusters collide. While the stars in galaxies act as collisionless particles and just pass by, the plasma in the clusters, however, interacts in the collision leading to a spatial separation of the stellar objects and the gas. In the left panel of Figure 2.4 the stars and galaxies follow the gravitational potential, but the majority of the baryonic mass in a galaxy cluster comes from gas. In the right panel of Figure 2.4 we can see that the plasma does not follow the gravitational potential. The conclusion is that the majority of the mass in the cluster has to be Dark Matter as the title of Clowe et al. (2006) states:

A DIRECT EMPIRICAL PROOF OF THE EXISTENCE OF DARK MATTER

This observation is not just evidence for the existence of Dark Matter, but also for its weakly interacting nature since it is collisionless.

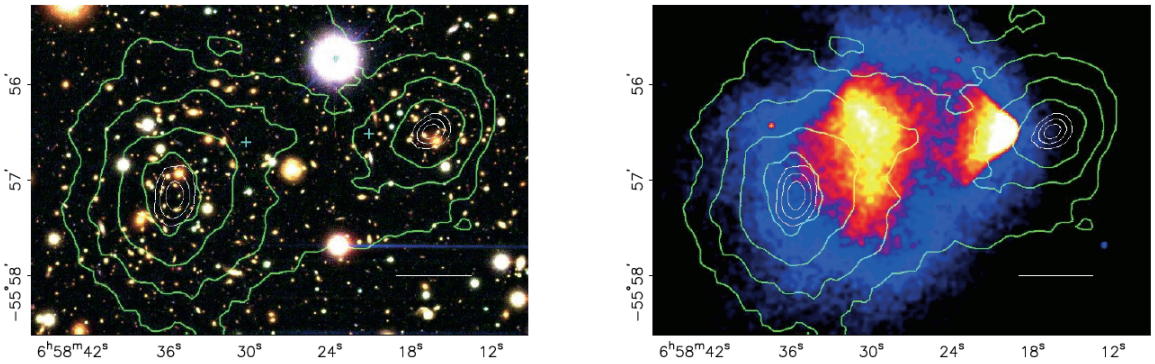

Figure 2.4: Images of the Bullet Cluster. Left: Image taken with the Magellan telescopes showing stars and galaxies. Right: Image taken with *Chandra*, the X-ray emission of the plasma is proportional to its density squared. The green contours trace the gravitational potential constrained with weak lensing. Figure taken from Clowe et al. (2006).

2.2.3 Cosmological evidence

Any cosmological model has the goal to describe the large-scale evolution (in time and space) of the universe with the help of the laws of general relativity and the cosmological principles. The predicted universe has to be homogeneous on large scales (no special place exists) and isotropic (no special direction). The Lambda Cold Dark Matter cosmological model (ΛCDM), also known as the cosmological standard model, is one way to describe the evolution. In this model the Friedmann equation is used to describe the evolution of the universe.

Friedmann Equation

The Friedmann equation describes the evolution of a homogeneous and isotropic universe in space time. Following the argumentation of Peacock (1999) and Schneider (2008) I will summarize the derivation of the Friedmann equation in Newtonian approximation and give an interpretation. In a homogeneous universe it is sufficient to consider only a small part. By doing so, we can apply the Newton Laws instead of general relativity. In the following all parameters with index "0" correspond to today's values. If we now consider a homogeneous expanding sphere with density $\rho(t)$ and a radius r_0, we can describe the mass of this sphere by

$$M(r_0) = \frac{4\pi}{3}\rho_0 r_0^3 \equiv M = \frac{4\pi}{3}\rho(t) r^3(t). \tag{2.3}$$

If space now expands, also the radius containing the mass M is expanding and we can derive

$$\ddot{r}(t) = -\frac{GM}{r^2} = -\frac{4\pi G}{3}\rho(t) r(t) = -\frac{4\pi G}{3}\frac{\rho_0 r_0^3}{r^2} \tag{2.4}$$

as the equation of motion of a test particle on the surface of the sphere. Now we can define $a(t) = \frac{r(t)}{r_0}$ as a dimensionless scaling parameter, multiply Equation 2.4 with $\frac{2da}{dt}$ and use $\rho(t) = \frac{\rho_0}{a^3}$. Solving the integral we end up with the Friedmann equation:

$$\dot{a}^2 = \frac{8\pi G}{3}\rho_0 \frac{1}{a} - Kc^2 = \frac{8\pi G}{3}\rho a^2 - Kc^2. \tag{2.5}$$

This equation can be interpreted as the conservation of energy for a test particle on the sphere. The integration constant K can be interpreted as the curvature of our three-dimensional space, leading to a flat ($K = 0$), open ($K < 0$) or closed ($K > 0$) universe. In case of an open universe the expansion goes on forever, in a closed universe the expansion stops ($a = a_{max} = \frac{8\pi G\rho_0}{3Kc^2}$) and is reverted into contraction. In the special case of a flat universe the expansion stops for $t \to \infty$. If the derivation of the Friedmann equation is done in the framework of the general relativity (GR), an additional term of $\frac{\Lambda a^2}{3}$ appears on the right side of Equation 2.5 (referred to as dark energy). For simplicity we define the Hubble parameter as:

$$H(t) = \frac{\dot{a}}{a} \quad ; \quad H_0 = \frac{\dot{a}(t_0)}{a(t_0)} = \dot{a}(t_0). \tag{2.6}$$

This parameter describes the expansion rate of the universe and can be measured. For the case of $K = 0$ we can write the critical density as

$$\rho_{cr} = \frac{3H_0^2}{8\pi G} = 1.88 \times 10^{-29}\,\mathrm{g/cm^3}. \tag{2.7}$$

This is the characteristic density of today's universe. It is useful to define the dimensionless density parameter $\Omega_0 = \frac{\rho_0}{\rho_{cr}} = 1$. Until now we did not care where the mass in our universe comes from. For further investigation we have to split the density parameter into

$$\begin{aligned} \Omega_0 &= \Omega_m + \Omega_r + \Omega_\Lambda = 1, \\ \Omega_m &\propto a^{-3}, \\ \Omega_r &\propto a^{-4}, \\ \Omega_\Lambda &= \frac{\Lambda}{3H_0^2}, \end{aligned} \tag{2.8}$$

where Ω_m is accounting for all matter that has non-relativistic velocity (baryonic and Dark Matter), Ω_r for relativistic matter and radiation. Ω_Λ comes from the Λ introduced by GR and can be expressed by $\frac{\Lambda}{3H_0^2}$. While the density of common matter Ω_m is proportional to a^{-3}, i.e. $\Omega_m \sim \frac{1}{\text{Volume}}$. For radiation (photons) the energy density Ω_r is proportional to a^{-4}, a factor of a^{-3} is equivalent to common matter while the fourth factor a comes from the fact that the wavelength is also scaling with a, known as redshift. These dependencies lead to the conclusion that the early universe was dominated by radiation. At a later stage, matter is dominating until the dark energy density (described by $\frac{\Lambda}{3H_0^2}$) takes over. From various measurements as well as some theoretical considerations we expect $\Omega_0 = 1$ in today's universe (Jungman et al., 1996). Observations are in agreement with a flat universe, however, the other cases can not be ruled out.

Measurements of cosmological parameters

The expansion rate of the universe (Equation 2.6) was originally measured from the radial velocity of distant nebulae according to Hubble's law (Hubble, 1929):

$$v = H_0 D \tag{2.9}$$

with v the velocity and D the distance of a nebulae. Today various methods are used to measure H_0. Using gravitation waves is one of them (Abbott et al., 2017). A recent measurement of the cosmic microwave background (CMB), which is a relic radiation from early stages of the universe evolution, results in $H_0 = 67.8\,\mathrm{kms}^{-1}\mathrm{Mpc}^{-1}$ (Planck Collaboration et al., 2016). The radiation follows a perfect black body law with a temperature of $(2.725\,48 \pm 0.000\,57)$ K (Fixsen, 2009). The origin of this radiation lies in the time when the universe expanded to a point at which matter and radiation were no longer in equilibrium. At that point a freeze out happened, so electrons were caught by nuclei and the mean free path of photons became almost infinite. Since then the spectrum was red shifted to its today's temperature. Figure 2.5 shows an all sky map of the CMB after subtraction of the average temperature. Furthermore it was corrected for the doppler effect due to the movement of the solar system and foreground emission from galaxies. From the size and amplitude of these deviations from the mean temperature one can conclude the values of the Ω parameters:

$$\Omega_m = 0.315 \pm 0.013$$
$$\Omega_\Lambda = 0.685 \pm 0.013$$
$$\Omega_r < 10^{-4}$$

Furthermore the content of baryonic matter in today's universe can be restricted to about $\Omega_b = 0.049 \pm 0.001$ which leaves $\Omega_{DM} = 0.25$ as non-baryonic matter, which is commonly referred to as Dark Matter. This is an important result of cosmology, since it is an evidence that a large fraction of all matter, in today's universe, is of non-baryonic nature. Another possibility to measure Ω comes from the observation of supernovae Type 1a. Results of such a measurement can be seen in Figure 2.6, which shows the Ω_m–Ω_Λ plain. A flat universe is in agreement with the measurements.

Relic abundance

One consequence of the ΛCDM is that Dark Matter is expected to be thermally produced in the early universe, resulting in an equilibrium between production and annihilation. With cooling of the universe, due to its expansion, production decreases and therefore the Dark Matter density is decreasing exponentially as well, in order to stay in equilibrium. At some point the annihilation becomes unlikely due to the falling density resulting in a freeze out. From here on the density remains almost constant. Figure 2.7 shows the Dark Matter density development with time.

Today's Dark Matter density can be explained with a Dark Matter particle mass $\sim 100\,\mathrm{GeV}$ and a typical velocity-weighted weak interaction cross section of $\sim 10^{-25}\,\mathrm{cm}^3/\mathrm{s}$. This is known as the "WIMP miracle" (Lisanti, 2017).

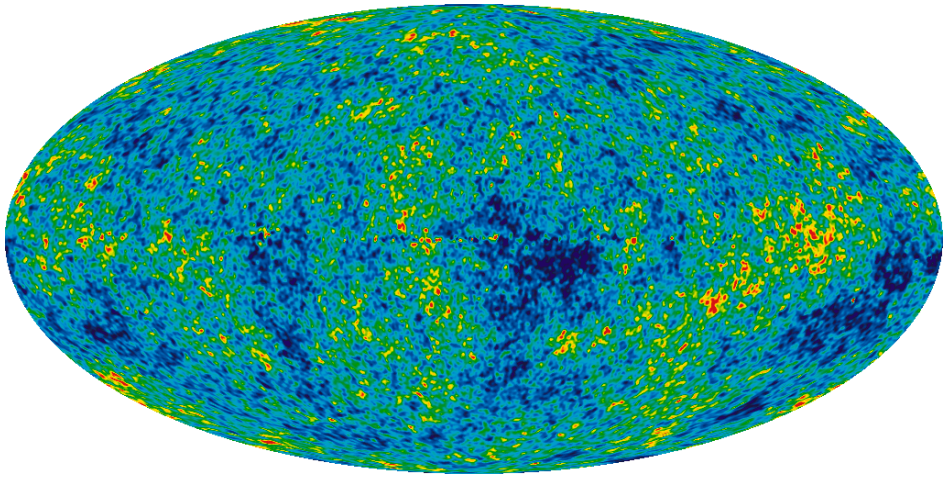

Figure 2.5: All sky image of nine years of WMAP data. The colour scale shows temperature fluctuations ±200 microKelvin after subtracting the mean temperature (Credit: NASA / WMAP Science Team).

2.3 Dark Matter candidates

In the past years different particles were discussed as candidates for Dark Matter. The most prominent among them are axions, neutrinos and WIMPs from supersymmetric models.

2.3.1 Neutrinos

From all particles contained in the standard model of particle physics the three neutrinos are the only particles which exclusively weakly interact and are stable, which makes them the only candidate for Dark Matter within the standard model. Due to a rather small neutrino mass ($m_{tot} \leq 0.3\,\mathrm{eV}$; Olive et al., 2014) Dark Matter consisting of neutrinos would have relativistic particle velocities (Hot Dark Matter). This would lead to a different structure formation than observed in today's universe. It is predicted that ,during the early universe, a cosmic neutrino background was formed similar to the CMB. However this can only account for a small fraction of the total Dark Matter mass (Schneider, 2008).

There are theoretical models predicting additional sterile neutrinos (Conrad & Shaevitz, 2016). These sterile neutrinos do not interact with the weak force. A priori the mass of a sterile neutrino is not given by theories. However a neutrino in the keV mass range has the expected properties of a Dark Matter particle and can be produced in the early universe evolution with properties accounting for the observed structure formation (Adhikari et al. (2017), Merle (2017)). For a very detailed overview on sterile neutrinos I recommend Adhikari et al. (2017).

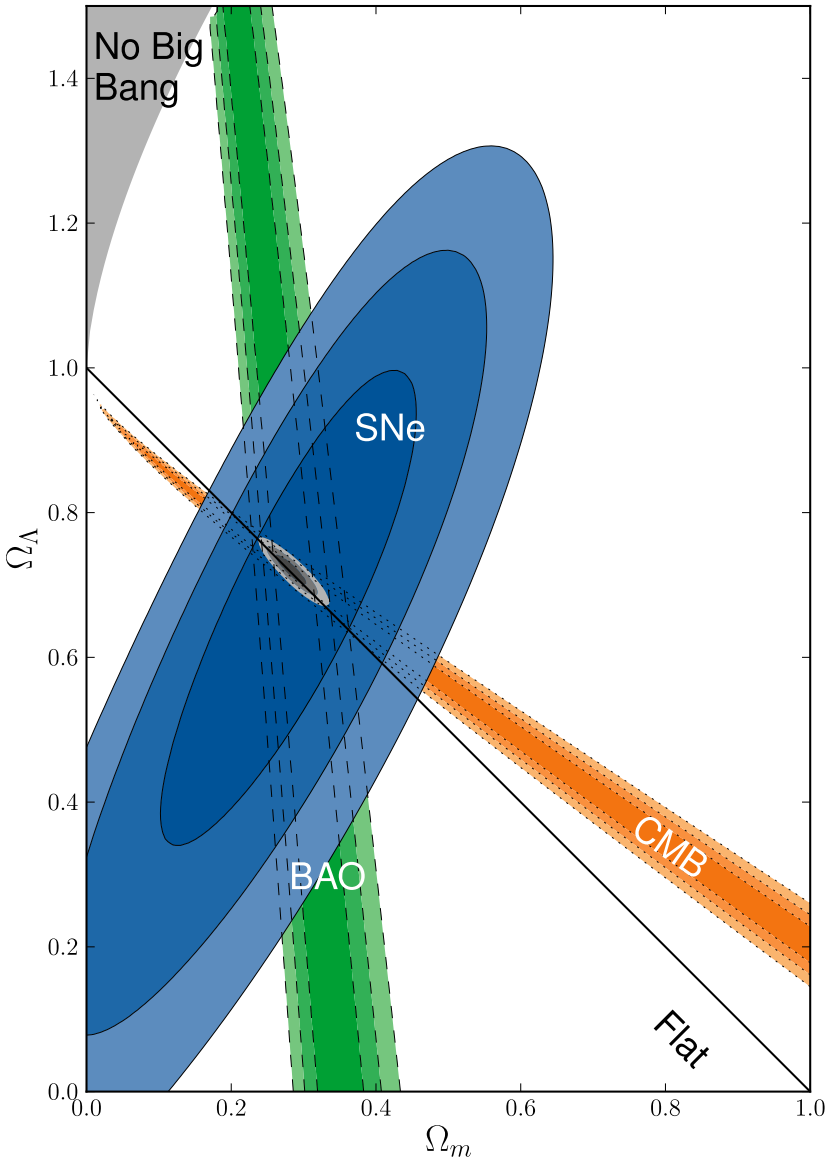

Figure 2.6: Results for Ω_m and Ω_Λ are shown for measurement of supernovae (SNe, blue), the cosmic microwave background (CMB, orange) and baryon acoustic oscillations (BAO, green). Figure taken from Suzuki et al. (2012).

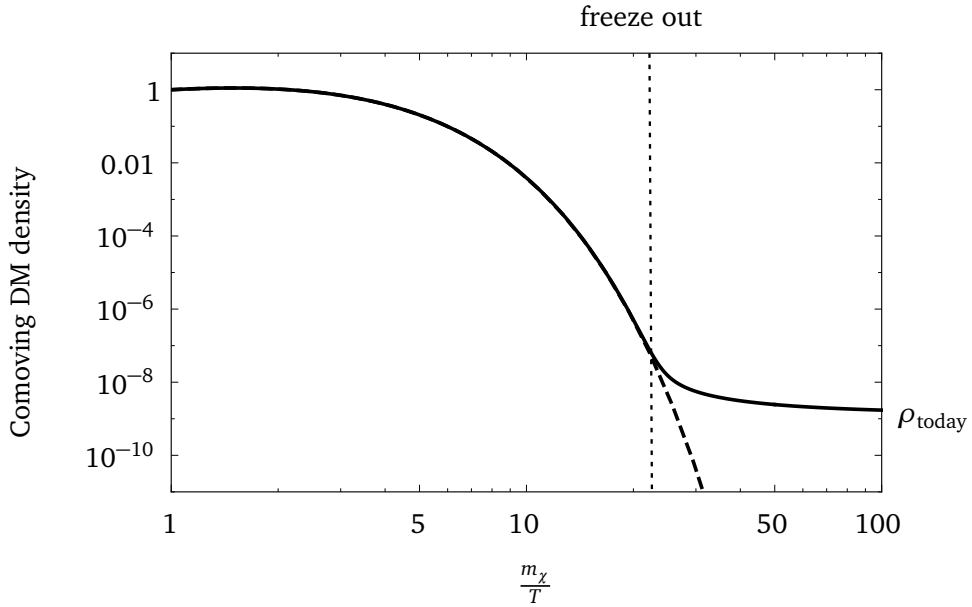

Figure 2.7: Evolution of the Dark Matter density with the cooling of the universe. The abscissa is given in $\frac{m_\chi}{T}$ with m_χ the Dark Matter particle mass and T the temperature; it can also be interpreted as time axis. First the density is falling exponentially according to the Boltzmann equation. After the freeze out the density remains almost constant. Figure adapted from Lisanti (2017).

2.3.2 Axion

The quantum chromodynamics (QCD) is a well-tested theory for the strong interaction. However, it has the problem of predicting strong charge-parity (CP) violating effects by the Lagrangian term:

$$\mathscr{L}_{QCD} \supset \bar{\Theta}\frac{g^2}{32\pi^2}G^{a\mu\nu}\tilde{G}^{a\mu\nu}. \tag{2.10}$$

With G being the gluon field strength tensor and $\bar{\Theta}$ a term related to the QCD vacuum. One would expect that $\bar{\Theta}$ is of the order of 1. However, such a value leads to a predicted dipole moment of the neutron 10^{10} higher than experimental limits. To explain observations $\bar{\Theta}$ has to be of the order of 10^{-10} which is theoretically not well motivated. In order to avoid this fine tuning issue Peccei & Quinn (1977) introduced a spontaneously broken symmetry resulting in a $\bar{\Theta}$ close to zero. A consequence of this symmetry is a new particle: the axion, which is electrically neutral and stable on cosmic timescales and has a very small cross section. These properties make the axion a reasonable Dark Matter candidate.

The Axion Dark Matter eXperiment (ADMX) is searching for axions in the μeV which might be able to explain Dark Matter (Stern & Experiment, 2016). So far no signal was found. The existence of an axion-like particle is still not proven, but some model realisations can be ruled out by accelerator experiments (Olive et al., 2014).

2.3.3 WIMP

The term WIMP, Weakly Interacting Massive Particle, does not refer to just one particle, but to a group of theoretically proposed particles with properties which fulfil the constraints given by Dark Matter. The WIMP term describes particles which only interact by the gravitational and weak force and have a mass of a few GeV to a few TeV. The standard model of particle physics does not provide a matching candidate, but many extensions of the standard model were developed over the past years. The two most prominent extensions with suitable WIMP Dark Matter candidates are the Kaluza-Klein theory and Supersymmetry.

Kaluza-Klein theory

In 1921, Theodor Kaluza invented a theory unifying gravity and electromagnetism by introducing an additional space dimension (Kaluza, 1921). The problem of this theory, however, was that the newly introduced space dimension is not observed. Later Oskar Klein extended this theory leading to its name (Klein, 1926). He solved the issue by compactifying the fourth space dimension: moving in this dimension is equivalent to moving on a very small circle with radius R. Due to the fact that we cannot observe this extra dimension, a particle with an excitation would be seen in our three observable dimensions as a new particle. The mass m of such a Kaluza-Klein (KK) state n can be written as:

$$m^2_{\chi^{(n)}} = \frac{n^2}{R^2} + m^2_{\chi^{(0)}} \tag{2.11}$$

with $\chi^{(0)}$ being a standard model particle (Hooper & Profumo, 2007). The mode n can be interpreted as a standing wave in the extra dimension (Corley & Lowe, 2001). The KK-parity, defined as $P = (-1)^n$, needs to be preserved in particle reactions; therefore the lightest Kaluza-Klein particle (LKP; $n = 1$) is stable. Pair annihilation of two KK particles however is possible. Servant & Tait (2003) discussed the $n = 1$ mode of the photon and neutrino as LKP candidate. At a mass in the TeV scale both may have annihilation cross sections which are in agreement with the Dark Matter mass density observed ($\Omega_{DM} \approx 0.25$).

Supersymmetry

In supersymmetric extensions of the standard model of particle physics a symmetry between fermions and bosons is introduced (Murayama, 2000). Due to this symmetry, for every fermion is assigned a bosonic superpartner, and for every boson a fermionic superpartner exists. This association of particles can be expressed by the space-time symmetry transformation Q^{SUSY}:

$$Q^{\mathrm{SUSY}}|\mathrm{fermion}> = \ |\mathrm{boson}> . \tag{2.12}$$

Today many different supersymmetric models exist. The Minimal Supersymmetric Standard Model (MSSM) is the minimal supersymmetric extension of the standard model in the sense that a minimum number of new particles is introduced. They are listed in Table 2.1.

Table 2.1: The table shows all particles and fields contained in the MSSM. The two left columns summarise the SM particles. The two columns in the middle show the interaction eigenstates of the MSSM particle while the two on the right show their mass eigenstates. After Edsjö (2014).

SM particles/fields		Supersymmetric particles/fields			
		Interaction eigenstates		Mass eigenstates	
Symbol	Name	Symbol	Name	Symbol	Name
u,s,t,d,c,b	quark	$\tilde{q}_L$,$\tilde{q}_R$	squark	$\tilde{q}_1$,$\tilde{q}_2$	squark
e, μ, τ	lepton	$\tilde{l}_L$,$\tilde{l}_R$	slepton	$\tilde{l}_1$,$\tilde{l}_2$	slepton
ν_e, ν_μ, ν_τ	neutrino	$\tilde{\nu}$	sneutrino	$\tilde{\nu}$	sneutrino
$g_{r,g,b}$	gluon	$\tilde{g}$	gluino	$\tilde{g}$	gluino
$W^\pm$	W-boson	$\tilde{W}^\pm$	Wino	$\tilde{\chi}^\pm_{1,2}$	chargino
$H^\pm$	Higgs boson	$\tilde{H}^\pm$	Higgsino		
B	B-field	$\tilde{B}$	Bino		
W^3	W	$\tilde{W}^3$	Wino	$\tilde{\chi}^0_{1,2,3,4}$	neutralino
$H^0_{1,2,3}$	Higgs boson	$\tilde{H}^0_{1,2}$	Higgsino		

In order to preserve baryon and lepton numbers in SUSY, an additional symmetry has to be introduced in form of R-parity:

$$P_R = (-1)^{3(B-L)+2s}, \tag{2.13}$$

where B is the baryon number, L the lepton number and s the spin. P_R is $+1$ for SM particles and -1 for SUSY particles (Bertone & Hooper, 2016)). Due to R-parity preservation the lightest supersymmetric particle has to be stable. In the MSSM, this particle is the neutralino ($\tilde{\chi}^0$), which is a linear combination of the Wino, Bino and Higgsinos. It carries no electromagnetic charge and does not interact strong. Predicted cross sections are in the right order of magnitude to explain the Dark Matter density. It is discussed in the literature that pair annihilation into photons is possible (Jungman et al., 1996). All these properties make the neutralino a good Dark Matter candidate.

2.3.4 Annihilation and decay spectrum of WIMPs

When WIMP pairs annihilate, a wide variety of particles can be created as annihilation products from e.g. (heavy) quark-antiquark pairs, lepton-antilepton pairs to $\gamma\gamma$ pairs. In consequent decays of unstable products further photons are produced. The resulting photon spectrum is a rather broad distribution with its exact shape depending on the underlying model and allowed processes. The continuous photon production can be written as (Cirelli et al., 2011):

$$\chi\chi \rightarrow ... \rightarrow \pi^0 \rightarrow \gamma\gamma. \tag{2.14}$$

There is also a monochromatic component:

$$\chi\chi \rightarrow \gamma\gamma \text{ or } \gamma Z. \tag{2.15}$$

In Figure 2.8 exemplary photon spectra are shown. No specific model was used. Therefore all channels have the same branching ratio. In a realistic model the $\gamma\gamma$ annihilation channel is loop suppressed and therefore contributes only to $\leq 10^{-3}$ of the total photon flux.

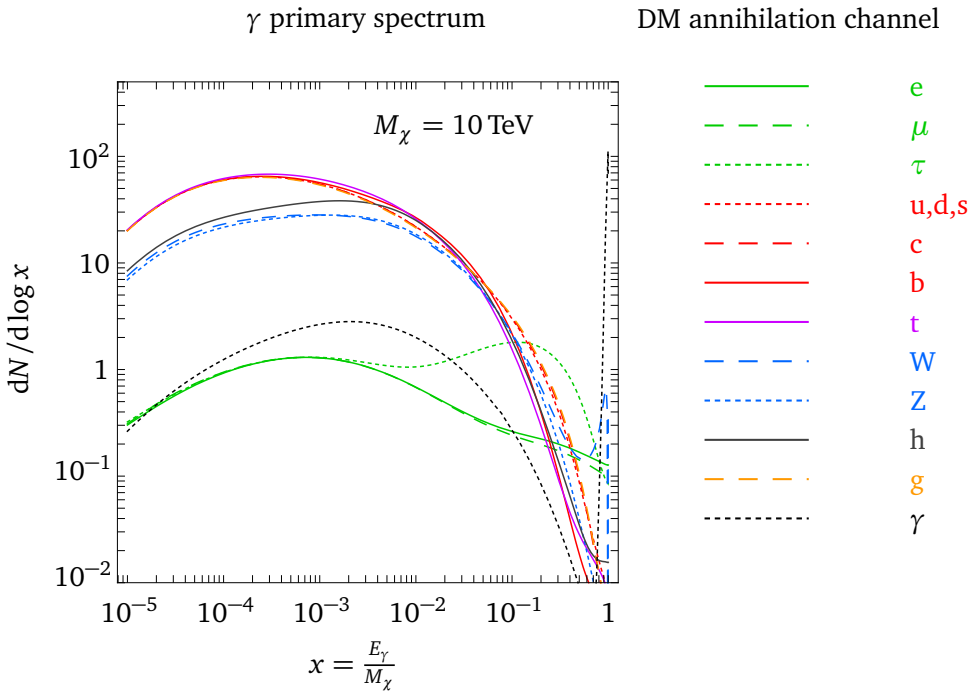

Figure 2.8: Photon spectrum from pair annihilation for a Dark Matter particle with the mass of 10 TeV in different annihilation channels. Contributions from leptons are in green, quark in red and purple, gluon in yellow, W and Z bosons in blue, Higgs in solid black and γ in dashed black. Figure adapted from Cirelli et al. (2011).

In the case of the $\gamma\gamma$ final state the photon spectrum can be described with a delta function:

$$\frac{\mathrm{d}N}{\mathrm{d}E_\gamma} = 2\delta(E_\gamma - m_\chi) \tag{2.16}$$

This is the so-called "smoking gun" signal, due to the fact that it is easily distinguished from astrophysical sources.

Some models also allow the decay of Dark Matter. In the case of decay the same products are produced as in pair annihilation. However, one has to scale the abscissa of Figure 2.8 by a factor of 0.5 to account for the change in the initial state from $\chi\chi$ to χ. Due to the fact that Dark Matter is still within the universe and not already decayed, the livetime has to be long on cosmological scale.

Furthermore internal bremsstrahlung can lead to photon production in the annihilation process (Bringmann et al., 2008), either in the form of final state radiation (FSR) or virtual internal bremsstrahlung (VIB). This leads to distortion of the photon spectrum resulting in more photons close to the Dark Matter particle mass. One example of a photon spectrum can be seen in Figure 2.9.

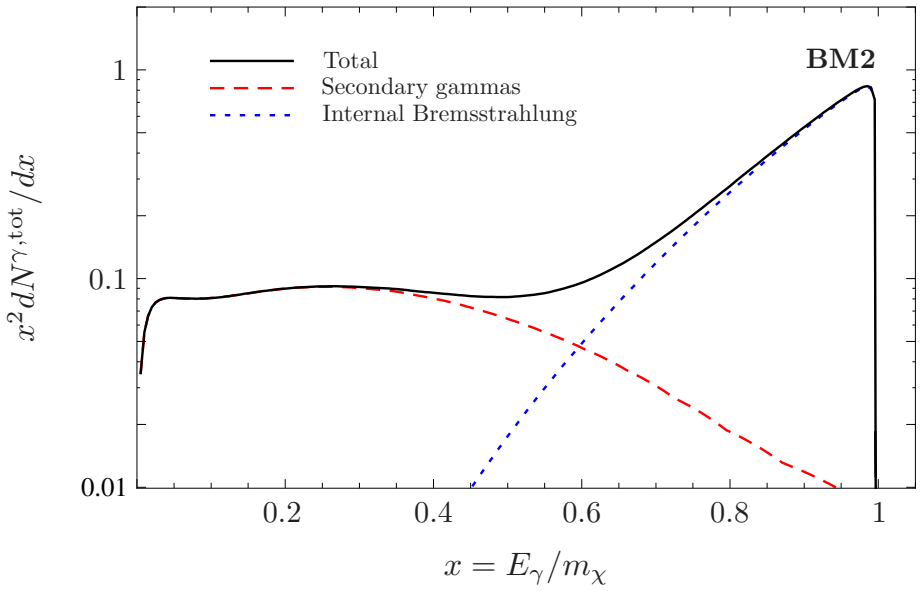

Figure 2.9: Photon spectrum from pair annihilating Dark Matter using a supersymmetric benchmark model with proper branching ratios. Line emission from $\chi\chi \to \gamma\gamma$ is not shown. Figure taken from Bringmann et al. (2008)

2.4 Modified Newtonian Dynamics

An alternative approach to explain the observations of galaxy rotation curves without the need of Dark Matter is the modification of Newton's mechanics in the limit of very small accelerations (with $a < a_0 \approx 1.2 \times 10^{-10}\,\mathrm{m\,s^{-2}}$). The role of the constant a_0 within MOND is comparable to the role of the speed of light in special relativity (Famaey & McGaugh, 2012). The well known second law $F = m \times a$ is modified to $F = ma^2/a_0$. In the early development of this theory modification were done to the 2. Law which does no longer preserve momentum or energy. Later theories like AQUAdratic Lagrangian theory got rid of this issue (Bekenstein & Milgrom, 1984). With this modification it is possible to explain rotation curves of Galaxies (see Figure 2.10). In the left panel the rotation curve of NGC 6503 is described by standard Newtonian mechanics using three components from gas, stars and Dark Matter. In the right panel Modified Newtonian Dynamics is used only relying on gas and stars to explain the observation.

While MOND is successful in describing the dynamics of galaxies, it is difficult to describe the dynamic of galaxy clusters, especially the Bullet Cluster. Furthermore it is difficult to explain the structure of the CMB and relativistic effects. There are attempts to address these problems; however, they all come at the expense of additional degrees of freedom in the theories and fine

tuning. For the interested reader I recommend Famaey & McGaugh (2012), a review on Modified Newtonian Dynamics and relativistic extensions.

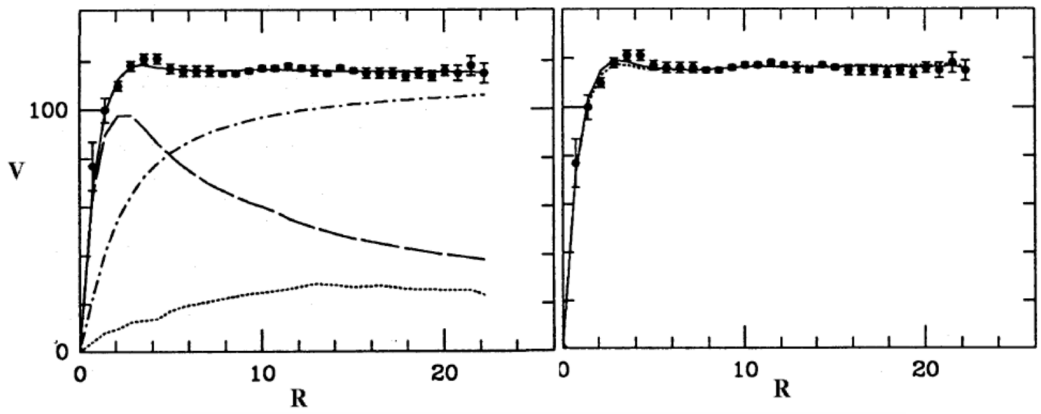

Figure 2.10: Rotation curve from the galaxy NGC 6503. The abscissa shows the distance to the centre of NGC 6503 in kpc and the ordinate shows the radial velocity of stars in km/s. Left: Fit of the data with a Dark Matter halo model showing three components: stellar (dashed line), gas (dotted line), and dark matter halo (dash dotted line). Right: Fit with MOND. Figure taken from Scarpa (2006).

2.5 Searching for a WIMP-like Dark Matter particle

The search for WIMPs can be done in three different ways, production at accelerators, direct and indirect search.
The production of WIMPs can be studied in accelerators like the LHC (Kahlhoefer, 2017). The idea is that according to crossing symmetry of the Feynman diagram (see Fig. 2.11) the annihilation process can be reversed into production. If the energy provided by the accelerator is sufficient, the reaction could take place although it will be hard to detect something since the produced WIMPs do not interact in the detectors and will only appear as missing energy. If, with the help of an accelerator, a WIMP-like particle is found in the future, we can learn something about the nature of the particle itself, but not about its distribution within the universe or if the particle found contributes to the Dark Matter density in the universe at all.

If a WIMP scatters with a nucleus inside a detector, the recoil energy can be measured. This is the idea behind direct WIMP search experiments. Inside the detector the recoil energy is converted into ionisation (electrons), scintillation light (photons) or heat (phonons) depending on the used detector material. Currently a large number of this type of experiments exist. They can be separated into two groups, one with liquid novel gas as detector material (e.g. DarkSide, XENON) and experiments using crystalline detectors (EDELWEISS, DAMA, CRESST) (Klasen et al., 2015). The results of these direct search experiments are contradictory, since some of them claim to have detected a signal while others exclude it (see Fig. 2.12). It is still under discussion where the detected signal comes from.

In indirect searches, decay or annihilation products of Dark Matter particles are looked for. Due to a very low expected rate this kind of search is carried out into the direction of an expected

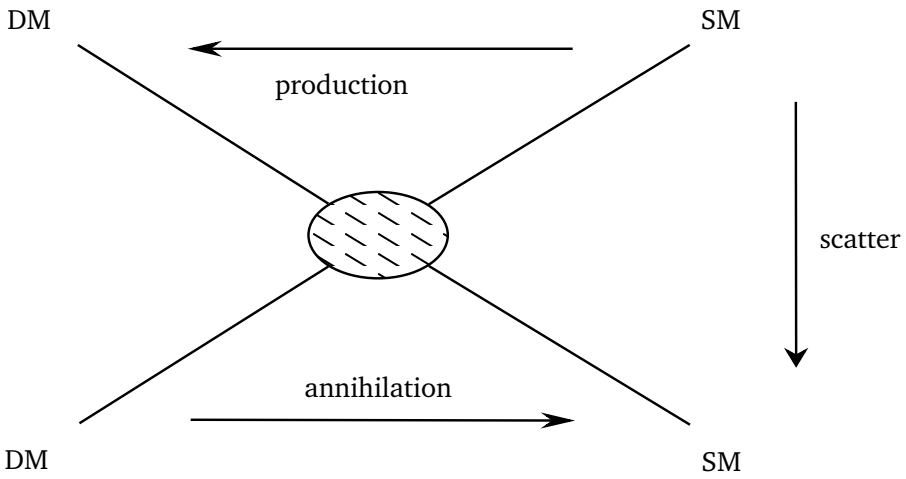

Figure 2.11: Feynman graph of the annihilation of Dark Matter into Standard Model particles. The graph can be read as scattering of a SM particle with a WIMP and production of a WIMP pair from a collision of SM particles.

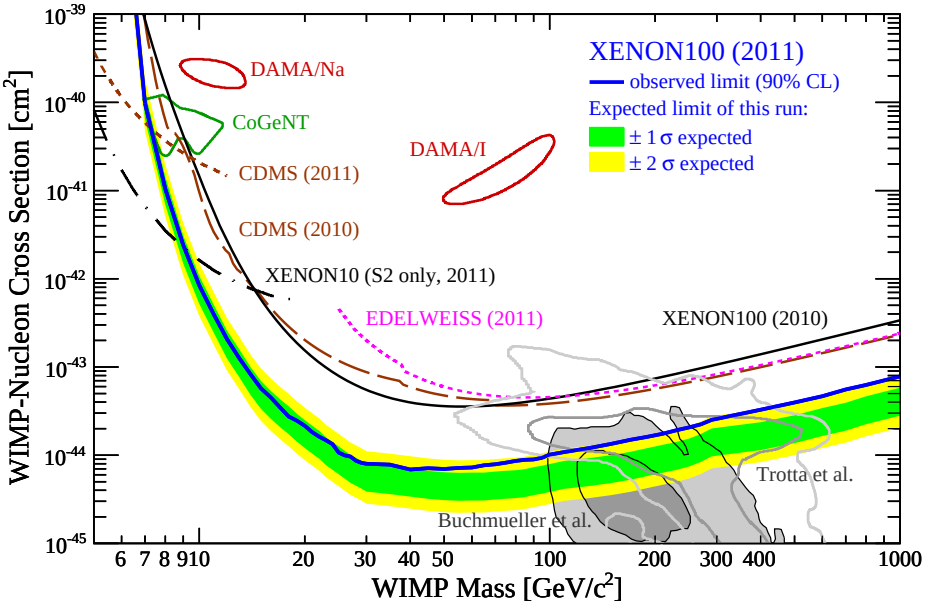

Figure 2.12: Shown are scattering cross section limits for different DM masses. The signal claimed by DAMA is excluded by EDELWEISS and XENON. Figure taken from Aprile et al. (2011)

high Dark Matter density. For instance, neutrino detectors like ANTARES or IceCube search for a neutrino signal from the direction of Earth centre, where due to scattering an enhanced Dark Matter density is expected (Albert et al., 2017b). Also searches towards the Galactic halo are performed (Albert et al., 2017a). Photon detection experiments (like *Fermi*-LAT and H.E.S.S.) search for a γ-ray signal from dwarf galaxies or the centre of the Milky Way. Photons might be produced in the annihilation process. Two contributions to the photon spectrum after annihilation are discussed in literature. Direct annihilation into a photon pair (or γZ_0), resulting in a line-like signal. Annihilation into charged particles (quarks, W-bosons) were photons are produced as decay products, resulting in a broad spectrum. The advantage of a search towards dwarf galaxies is the rather low background due to astrophysical γ-ray sources in the GeV to TeV energy range. The disadvantage, however, is a low expected Dark Matter density in comparison with the Galactic Centre.

The analysis presented in this work is using the Galactic Centre region for a search of a line-like signal from Dark Matter annihilation.

2.6 Galactic Centre

The Galactic Centre (GC) is one of the most violent places in the Milky Way. H.E.S.S. detected two very bright point sources, one located at the position of the supernova remnant / pulsar wind nebula G 0.9+0.1. The other is coincident with the super massive black hole Sgr A* (see Figure 2.13 top). If these two sources are subtracted from the observation (see Figure 2.13 bottom), a band of diffuse emission along the galactic plane becomes visible as well as the unidentified source HESS J1745-303 (van Eldik, 2015). In Abramowski et al. (2016) it is reported that H.E.S.S. discovered tracers for PeV particles in the inner few parsec of the galaxy. It is further argued that Sgr A* might be a PeVatron. Abdalla et al. (2017a) reported the discovery of a new source close to the Galactic Centre named HESS J1746-285. This source is located at the edge of the so-called GC radio arc and close to the pulsar wind nebula candidate G0.13-0.11. All these sources make the Galactic Centre a very comprehensive region in the GeV to TeV energy range.

The central region of the Galactic Centre is expected to host a large amount of Dark Matter. Therefore some searches for Dark Matter signals in the VHE range were carried out by H.E.S.S. No significant excess was found yet. However the latest upper limits on a line-like γ-ray signal from Dark Matter annihilation come from Abramowski et al. (2013) and can be seen in Figure 2.14. In the H.E.S.S. analysis data taken until 2008 was used, including only data from the first phase of H.E.S.S.

In 2012 the hint for a line-like signal (3.2σ) with an energy of 130 GeV was reported by Weniger (2012). The *Fermi*-LAT Collaboration investigated this reported line-like feature using an updated event reconstruction and selection on a larger data set (Ackermann, Ajello, et al., 2015). The significance of the signal went down to 0.72σ. As a follow-up the H.E.S.S. Collaboration performed an analysis towards this region (Abdalla et al., 2016a). No signal was found and the reported annihilation cross section was excluded with 95 % CL.

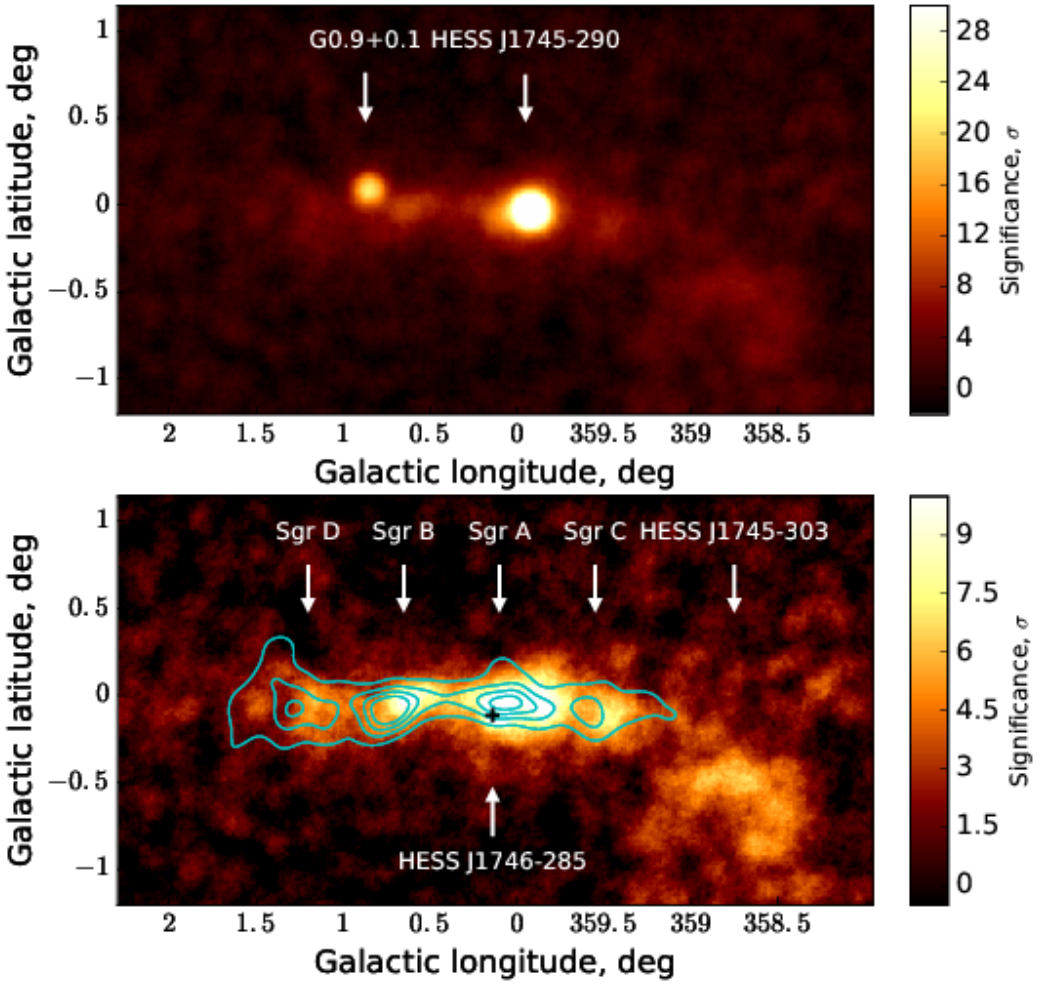

Figure 2.13: Galactic Centre map in VHE γ ray taken by H.E.S.S.. The image is smoothed with the H.E.S.S. PSF. Top: Significance map revealing two very bright sources G 0.9+0.1 and HESS J1745-290. Bottom: Residual significance map after subtraction of the two bright sources. Diffuse emission along the galactic plane is visible spatially coincident with molecular gas (cyan contours). The newly discovered source HESS J1746-285 is indicated by a black cross. Figure taken from Abdalla et al. (2017a).

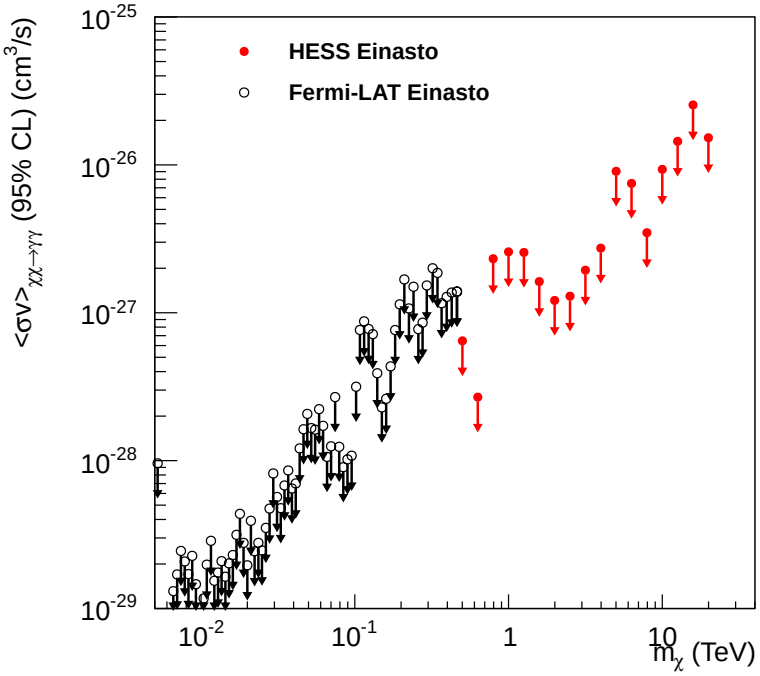

Figure 2.14: Upper limits on the velocity-weighted annihilation cross section for $\chi\chi \to \gamma\gamma$. *Fermi*-LAT data (black) was taken from Ackermann, Ajello, et al. (2015) and the H.E.S.S. data (red) taken from Abramowski et al. (2013). Both analyses assume a Cusped Einasto shaped density profile.

Also searches for a broad annihilation spectrum were carried out the latest results, using data from the first phase of H.E.S.S., can be found in Abdalla et al. (2016b), for Cusped density profiles, and Abramowski et al. (2015), for Cored density profiles. Figure 2.15 shows a selection of different analyses for the annihilation channel $\chi\chi \to b\bar{b}$. As one can see at low Dark Matter masses ($m_\chi < 500\,\mathrm{GeV}$) satellite experiments like *Fermi* provide the currently best limits (in red solid line). Above this energy H.E.S.S. provides the best cross section limits using data from the Galactic Centre (black solid line). Furthermore results for analyses of dwarf galaxies are shown (black dashed line and blue solid line). Due to a much lower Dark Matter density these limits are worse compared to limits for the Galactic Centre. Also shown are limits from IceCube (green line), however, currently the sensitivity of Cherenkov telescopes is several orders of magnitude higher.

2.7 Flux expectation

In order to calculate flux or annihilation cross section limits, we need to know the expected flux for a given cross section and dark matter density distribution. Therefore we have to understand how the geometry of the analysed region and particle physics of a WIMP contribute. The goal of the following derivation is to come up with an equation which gives the expected photon flux from self-annihilating Dark Matter. In order to accomplish this, we have to think about the Dark Matter distribution within the Milky Way and about the particle physics of a WIMP.

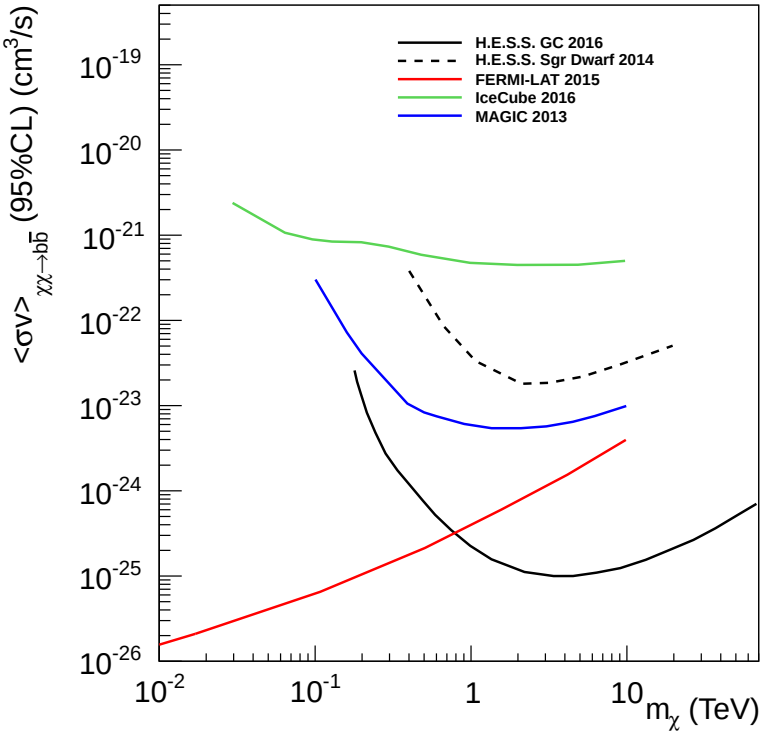

Figure 2.15: Upper limits on the velocity-weighted annihilation cross section for the annihilation channel $\chi\chi \to b\bar{b}$. H.E.S.S. GC limits are taken from Abdalla et al. (2016b). H.E.S.S. Sgr Dwarf limits are taken from Abramowski et al. (2014). *Fermi*-LAT limits are from Ackermann, Albert, et al. (2015). MAGIC limits are for the dwarf galaxy Segue 1 taken from Aleksić et al. (2014). IceCube limits are taken from Aartsen et al. (2016). In the analyses shown different Dark Matter halo profiles were used, this makes quantitative comparison problematic. However one can see that Galactic Centre analyses result in better limits compared to Dwarf galaxies.

2.7.1 Dark Matter distribution

The Dark Matter distribution inside of galaxies cannot be observed directly. To get an idea of the distribution one has to simulate Dark Matter or model rotation curves of galaxies. This leads to many different models and is one of the big uncertainties when calculating flux or upper limits for Dark Matter annihilation.

One common assumption for the modelling of the Dark Matter distribution of a galaxy is that the distribution is radial symmetric. In the following I will introduce the most commonly used models. As a result of studying the galaxy NGC 4650A, Sackett & Sparke (1990) came up with a so-called Isothermal model (see Fig. 2.16):

$$\rho_{\mathrm{iso}}(R) = \frac{\rho_0}{1 + \left(\frac{R}{r_s}\right)^2}. \tag{2.17}$$

With ρ_0 the characteristic density, r_s the scaling radius and R the distance of the galaxy's centre. Characteristic for this profile is the extended core of constant density (see Fig. 2.16).

Two commonly used profiles are the Navarro, Frenk and White (NFW) (Navarro et al., 1996):

$$\rho_{\mathrm{NFW}}(R) = \rho_0 \left[\frac{R}{r_s} \left(1 + \frac{R}{r_s} \right)^2 \right]^{-1}, \tag{2.18}$$

and the Einasto (Einasto, 1965):

$$\rho_{\mathrm{Einasto}}(R) = \rho_0 \exp\left\{ -\frac{2}{\alpha} \left[\left(\frac{R}{r_s} \right)^{\alpha} - 1 \right] \right\}, \tag{2.19}$$

with $\alpha = 0.17$, r_s the scaling radius, R the distance to the galaxy's centre and ρ_0 the characteristic density. Both profiles are successful in describing the results of simulations such as Aquarius (Springel et al., 2008) and Via Lactea II (Diemand et al., 2008). These simulations are cosmological N-body simulations, which try to investigate the structure formation in Milky Way-like galaxies. In these simulations only Dark Matter was simulated, leading to a rather high density at the centre of the galaxy (referred to as Cusped profiles hereafter).

If baryonic matter is included into such a simulation, the Dark Matter distribution becomes flat towards the centre of the galaxy (Governato et al. (2012) and Pontzen & Governato (2014)). The result is that in the inner 500 pc, the Dark Matter density remains almost constant for a Milky Way-like galaxy. The radial profile can still be described by a NFW or Einasto profile, but with a constant density in the inner part (referred to as Cored profiles hereafter).

It is unknown which of these profiles is best to describe the distribution of Dark Matter within the Milky Way. Therefore both the Einasto and the NFW profile are tested in both the Cored and Cusped configuration. For an easier comparison of results I am using values for ρ_0 and r_s which were already used by the H.E.S.S. Collaboration. The parametrisation for the Cusped profiles was used in Abramowski et al. (2013) and that for the Cored profiles in Abramowski et al. (2015). The parametrisation of the Isothermal profile is adapted from Kieffer (2015).

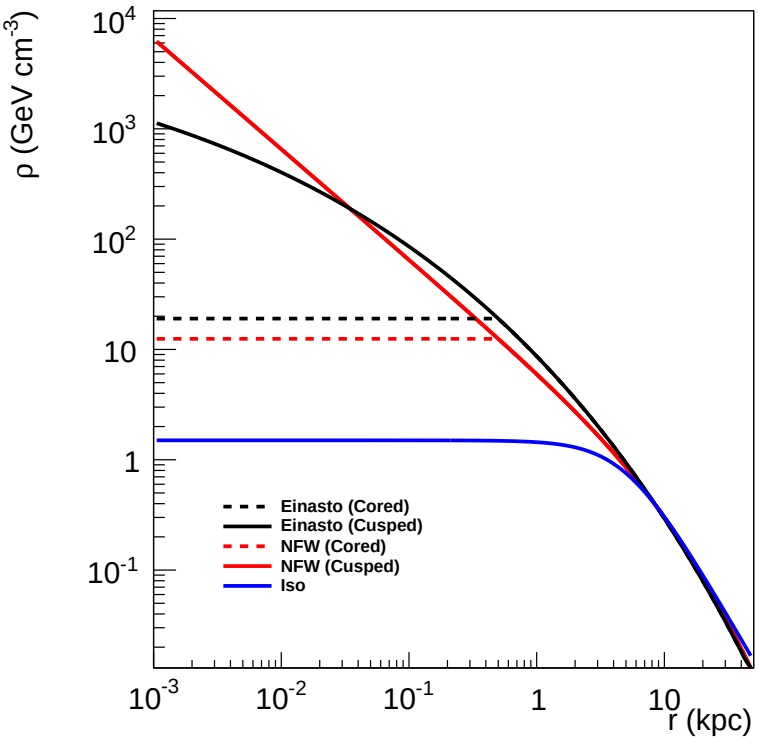

Figure 2.16: Dark Matter density profiles NFW (red), Einasto (black) and Isothermal (blue). All profiles are normalized to 0.39 GeV/cm^3 at 8.5 kpc according to the Dark Matter density in the solar system (Catena & Ullio, 2010).

2.7.2 Derivation of the photon flux expectation

This section follows the argumentation of Lohse (2014).
To derive the expected photon flux of self annihilating Dark Matter we can first consider a Volume V containing Dark Matter particles. A single Dark Matter particle χ, with velocity v, has an interaction volume ($\mathrm{d}V$), where the particle passes through in the time ($\mathrm{d}t$):

$$\mathrm{d}V = \sigma(v) \times v \mathrm{d}t, \tag{2.20}$$

with $\sigma(v)$ the velocity depending annihilation cross section. In order to obtain the annihilation rate Γ within the volume V we have to divide by $\mathrm{d}t$ and V:

$$\Gamma = \frac{\mathrm{d}V}{\mathrm{d}t \times V} = \frac{\sigma(v) \times v}{V} \tag{2.21}$$

Until now we only tracked one particle. To calculate the total annihilation rate we have to sum over all Dark Matter particles in the volume V:

$$\Gamma_{\mathrm{tot}} = \frac{1}{V} \times \sum_{\substack{\text{targets,} \\ \text{projectiles}}} \sigma(v) \times v = \frac{1}{V} \times C\langle\sigma v\rangle, \tag{2.22}$$

with $\langle\sigma v\rangle$ the velocity-weighted annihilation cross section and C the number of target-projectile pairs. We can write C as:

$$C = \begin{cases} N_{\overline{\chi}} N_{\chi} = \frac{N^2}{4} & , \chi \neq \overline{\chi} \\ \frac{N(N-1)}{2} \approx \frac{N^2}{2} & , \chi = \overline{\chi} \end{cases} \tag{2.23}$$

with N the total number of particles in the case of a Majorana Dark Matter particle, N_{χ} the number of particles and $N_{\overline{\chi}}$ the number of its antiparticles in case of a non-Majorana Dark Matter. In the following I will write only formulas for a Majorana Dark Matter particle ($\chi = \overline{\chi}$), however the only difference is a factor of 2^{-1} under the assumption $N_{\chi} = N_{\overline{\chi}}$.
The number of Dark Matter particles is unknown, however we can express it with the help of the density $N = \frac{\rho V}{m_{\chi}}$, where ρ is the Dark Matter mass density and m_{χ} the mass of a single particle.

$$\frac{\mathrm{d}\Gamma}{\mathrm{d}V} = \frac{\rho^2}{2m_{\chi}^2}\langle\sigma v\rangle. \tag{2.24}$$

We are interested in the photon flux form annihilations. Therefore we have to multiply Equation 2.24 by the photon spectrum $\frac{\mathrm{d}N_{\gamma}}{\mathrm{d}E}$:

$$\frac{\mathrm{d}\Gamma_{\gamma}}{\mathrm{d}V\mathrm{d}E} = \frac{\rho^2}{2m_{\chi}^2}\frac{\mathrm{d}N_{\gamma}}{\mathrm{d}E}\langle\sigma v\rangle. \tag{2.25}$$

Photons produced in the annihilation process are radiated isotropically. So we need to scale with the detector area (A) divided by the total area:

$$\mathrm{d}\Gamma_{\mathrm{detected}} = \frac{A}{4\pi s^2}\mathrm{d}\Gamma_{\gamma}, \tag{2.26}$$

with s the distance from the annihilation to the detector. The detected photon flux can now be written as:

$$\frac{\mathrm{d}\Phi}{\mathrm{d}E} = \frac{1}{A}\frac{\mathrm{d}\Gamma_{\mathrm{detected}}}{\mathrm{d}E} = \frac{1}{4\pi s^2}\frac{\rho^2}{2m_\chi^2}\frac{\mathrm{d}N_\gamma}{\mathrm{d}E}\langle\sigma v\rangle \mathrm{d}V. \tag{2.27}$$

The annihilation does not only take place in an isolated source ,but along the entire line of sight. As seen in the previous section, Dark Matter is distributed in a halo within the entire galaxy. Therefore we have to regroup Equation 2.27 and integrate the density along our line of sight (s) and the observed field of view (Ω):

$$\frac{\mathrm{d}\Phi}{\mathrm{d}E} = \underbrace{\frac{1}{4\pi}\frac{\langle\sigma v\rangle}{2m_\chi^2}\frac{\mathrm{d}N_\gamma}{\mathrm{d}E}}_{\text{particle physics}} \times \underbrace{\int_{\text{fov, los}}\int \rho^2 \mathrm{d}s\mathrm{d}\Omega}_{\text{J-Factor}}. \tag{2.28}$$

As we can see after the regrouping, Equation 2.28 can be separated into one term that contains all the particle physics. This term is depending on the underlying model for the photon spectrum from annihilations. In this work only pair annihilation into two photons ($\chi\chi \rightarrow \gamma\gamma$) is considered. The consequence is that $\frac{\mathrm{d}N_\gamma}{\mathrm{d}E}$ can be described by a delta function with its peak at the mass of the Dark Matter particle.
The second term contains information about the dependence of the Dark Matter distribution known as J-Factor.

With a similar thought process one ends up with a photon flux expectation for decaying Dark Matter with:

$$\frac{\mathrm{d}\Phi}{\mathrm{d}E} = \underbrace{\frac{1}{4\pi}\frac{\Gamma}{m_\chi}\frac{\mathrm{d}N_\gamma}{\mathrm{d}E}}_{\text{particle physics}} \times \underbrace{\int_{\text{fov, los}}\int \rho \mathrm{d}s\mathrm{d}\Omega}_{\text{J-Factor}}. \tag{2.29}$$

With Γ the decay width. As one can see, the J-Factor is now proportional to ρ resulting in a lower photon flux expectation compared to pair annihilation.

2.8 Analysis requirements

In order to perform a successful line-signal search from Dark Matter annihilation in the vicinity of the Galactic Centre, several requirements have to be fulfilled. For a WIMP search in the GeV to TeV energy range we can formulate the requirements as:

- A good energy resolution in order to resolve a line-like signal
- High sensitivity in the GeV to TeV energy range
- Good background suppression
- Careful selection of the analysis region

Chapter 3

H.E.S.S. and the working principle of Cherenkov telescopes

As already mentioned it is worth searching for a Dark Matter signal in den GeV to TeV range, since we expect particles in this mass range to be cold. Satellite experiments like *Fermi*-LAT are able to detect photons up to a few hundred GeV but do not provide the necessary detection area at higher energies. Therefore it is necessary to use a ground based technique such as Imaging Atmospheric Cherenkov Telescopes (IACT). Since the atmosphere is not transparent to photons at very-high energies, particles with the energy of interest can only be detected indirect with the help of Cherenkov light produced in the atmosphere.

In this chapter I will first introduce the detection principle of Imaging Atmospheric Cherenkov Telescopes followed by a detailed description on how the analysis of the data from the High Energy Stereoscopic System (H.E.S.S.) is done.

3.1 Air-shower development

Cosmic rays hitting the atmosphere will interact and produce a cascade of secondary particles, also known as a particle shower. For γ rays , e^+ and e^- a so-called electromagnetic shower is created, for the shower development the dominant processes are (after Heitler (1954)):

- e^+e^- pair production is the dominant interaction process for high energetic photons. Because of energy and momentum conservation this can only occur in the vicinity of another particle.
- Emission of Bremsstrahlung photons is the dominant process e^+ and e^- undergo in the Coulomb field of an atomic nuclear. This process is occurring while the energy of e^+ and e^- is above a critical energy (in air $E_c \approx 81\,\mathrm{MeV}$).
- Ionization is the dominant process once the average particle energy falls below E_c. Once this stage is reached the shower development comes quickly to an end.

A simplified model description of an electromagnetic shower is the so-called Heitler model. In this model only pair production and Bremsstrahlung are taken into account. Every photon undergoes

pair production after travelling a distance of X_0 producing a pair of e^+e^- with each half of the energy of the initial photon. The $e^\pm$ radiate a photon each with half of their energy after a distance of X_0. The characteristic length X_0 is the electromagnetic radiation length:

$$\frac{1}{X_0} = 4\alpha r_e^2 \frac{N_A}{A} Z^2 \ln(183 Z^{1/3}). \tag{3.1}$$

In dry air the radiation length is 36.7 g cm^{-2} (de Naurois, 2012). These two processes repeat until the energy of the shower particles drops below E_c. At this point the shower contains $N = 2^n$ particles with energy $E = \frac{E_0}{N}$ each. Figure 3.1 shows a sketch of such an air shower, where n is the number of interaction steps and E_0 the energy of the particle hitting the atmosphere.

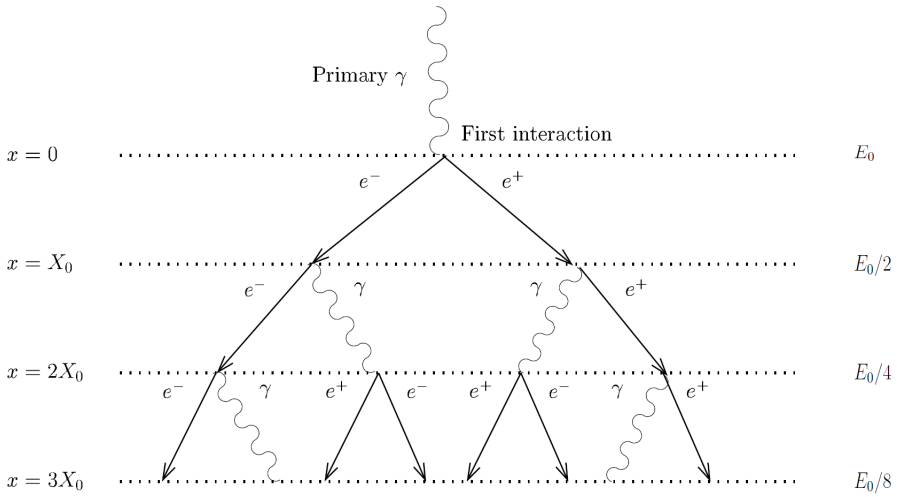

Figure 3.1: Sketch of an electromagnetic air shower according to the Heitler model. At each step of radiation length the particles undergo pair production and Bremsstrahlung. Figure taken from Funk (2005).

In showers induced by hadrons, mainly protons, not only the above mentioned electromagnetic processes happen, but also hadronic interactions (Funk (2005) and de Naurois (2012)). They lead to fragmentation of the primary particle and to the production of charged mesons ($\pi^\pm$, $K^\pm$) decaying dominantly into $\mu^\pm$ and neutrinos. Neutral mesons (π^0, K^0) decay in the case of K^0 into charged and uncharged pions and in the case of π^0 into $\gamma\gamma$. The γ from π^0 decay can lead to an electromagnetic sub-shower. Figure 3.2 shows the sketch of a hadronic air shower.

3.2 Emission of Cherenkov light

In 1934 Pavel Cherenkov discovered that charged particles, travelling faster than the speed of light in a medium, radiate light (Čerenkov, 1937). For this discovery, he was awarded the Nobel prize in physics in 1958 together with two fellow physicists[1].

[1] http://www.nobelprize.org/nobel_prizes/physics/laureates/1958/

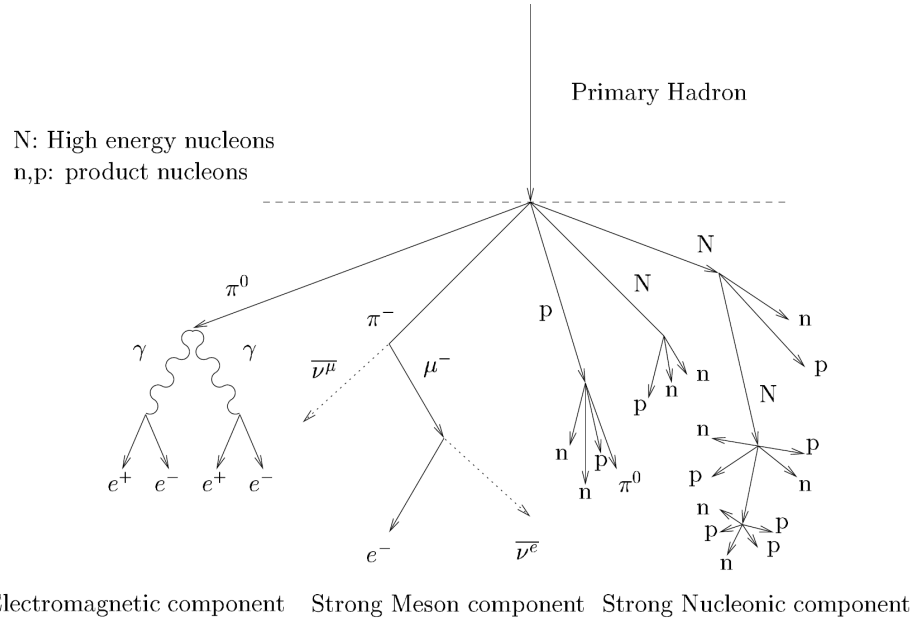

Figure 3.2: Sketch of a hadronic air shower. On the left an electromagnetic sub-shower is visible induced by a π^0. The rest of the shower is of hadronic nature. Figure taken from Funk (2005).

Cherenkov photons are emitted in a cone around the path of their parent particle. The opening angle can be written as:

$$\theta = \arccos\left(\frac{1}{\beta n_m}\right), \tag{3.2}$$

where β is the particle speed divided by the speed of light in vacuum, and n_m the refraction index of the medium. In the case of air θ is about 1°.2 (Holler, 2014). The number of photons emitted per unit path length and wavelength interval is given by the Franck-Tamm formula:

$$\frac{\mathrm{d}^2 N}{\mathrm{d}x\mathrm{d}\lambda} = 2\pi\alpha\frac{\sin^2\theta}{\lambda^2}. \tag{3.3}$$

Cherenkov light is predominantly emitted in a small wavelength range in visible and UV light. In the infrared and above the term $\frac{1}{\lambda^2}$ is suppressing the radiation and for a wavelength below the UV $n(\omega) \approx 1$ leads to suppression (Spengler, 2013).

3.3 Detection principle of air Cherenkov Telescopes

Due to the development of particle cascades and the resulting Cherenkov light, the atmosphere of the Earth can be used as a calorimeter for the detection of γ rays. The typical Imaging Atmospheric Cherenkov Telescope (IACT) has a mirror dish focussing the Cherenkov light onto a camera similar to telescopes used for optical observations. Figure 3.3 (left) shows how the light cone develops in the atmosphere and (right) the Cherenkov light distribution of a γ ray as seen on the ground. If a IACT is within this cone, a shower image can be seen (Figure 3.4 shows a sketch of an air shower projected into the camera plane). Since a Cherenkov light flash is very faint and only lasts for ~10 ns, a large collection area and a short read-out window is needed, otherwise the Cherenkov

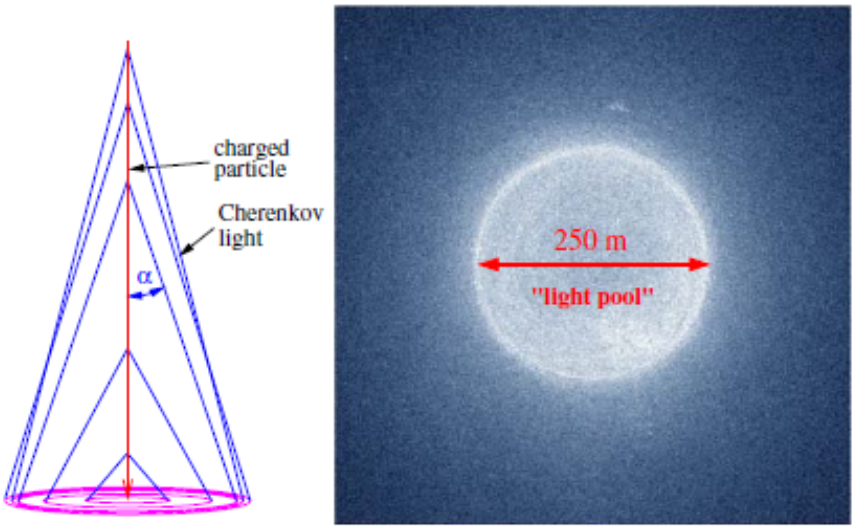

Figure 3.3: Left: Sketch of a charged particle emitting Cherenkov light (α in the figure corresponds to the angle θ in Equation 3.2 and 3.3). Right: Simulated Cherenkov light distribution on ground for a primary photon with 1 TeV energy at an altitude of 1800 m. Figure taken from Völk & Bernlöhr (2009).

light will be outshined by the night sky background (NSB). Currently the third generation of IACTs is in operation: H.E.S.S.[2], MAGIC[3] and VERITAS[4], with the fourth generation (CTA[5]) currently in construction. While the basic detection principle is the same for all Cherenkov telescopes, the technical implementations can be different. In the following I will discuss exclusively H.E.S.S., since all data used in this work have been recorded with H.E.S.S.

3.4 The High Energy Stereoscopic System

The High Energy Stereoscopic System (H.E.S.S.) is a γ-ray detection experiment located in the Khomas Highlands close to the Gamsberg in Namibia. The exact location of the telescope array is 23°.161 S, 16°.301 E at 1800 m N.N. (Hofmann & H.E.S.S. Collaboration, 2001). In the first phase (from here on called H.E.S.S. I) the array consisted of four Cherenkov telescopes (CT1 to CT4) with a focal length of 15 m and 108 m^2 reflective area each. These telescopes were built in 2002 and 2003. They are equipped with cameras each consisting of 960 photomultipliers (PMT) and have a field of view (FoV) of 5°. In 2012 H.E.S.S. started its operation in phase two (H.E.S.S. II hereafter) now extended by a fifth telescope (CT5) built in the centre of the existing array. This newly built telescope has a focal length of 36 m, a reflective area of 614 m^2, a FoV of 3°.2 and the camera consists of 2048 PMTs (all numbers are summarized in Table 3.1). Due to the addition of the fifth telescope the energy threshold was lowered and the effective area increased. A photo of the array in phase two is shown in Figure 3.5.

[2] https://www.mpi-hd.mpg.de/hfm/HESS/
[3] https://wwwmagic.mpp.mpg.de/
[4] http://veritas.sao.arizona.edu/
[5] https://www.cta-observatory.org/

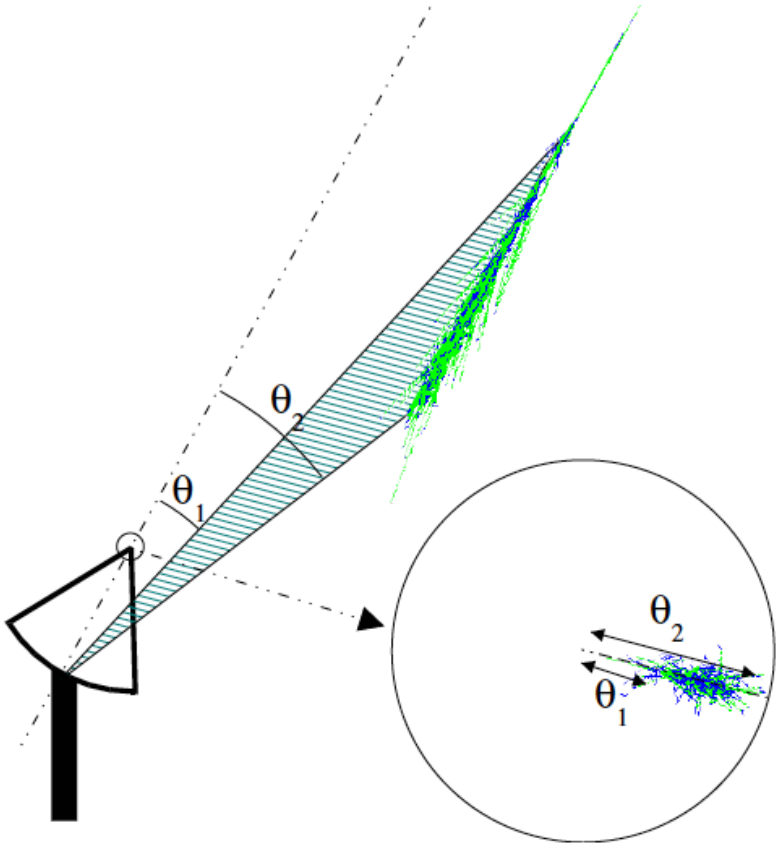

Figure 3.4: Sketch of a Cherenkov telescope seeing an air shower and its projected image in the camera plane. Figure taken from de Naurois (2012).

Table 3.1: The table shows the technical data for the two telescope types of the H.E.S.S. array (H.E.S.S. Collaboration, 2017). The field of view stated here is the optical field of view, for high level analyses a smaller region is used. Values marked with a (*) are given for events in stereoscopic reconstruction (also called hybrid mode).

	H.E.S.S. I (CT1–CT4)	H.E.S.S. II (CT5)
Reflector shape	Davies-Cotton	Parabolic
Focal length	15 m	36 m
Reflective area	108 m^2	614 m^2
Camera pixel	960	2048
Effective exposure time	16 ns	16 ns
Image recording rate	300 Hz	3600 Hz
Angular resolution	<0.°1	0.°24–0.°28
Energy range	100 GeV – ∼100 TeV	40 GeV (*) – ∼ 100 TeV
Energy resolution	15%	15% (*)
Field of View	5°	3.°2

In 2016 the cameras of the small telescopes were replaced with new ones, with the goal of a lower dead time, reduced system failure rate, and improved over all performance (Giavitto et al., 2015). This upgraded phase is called H.E.S.S. IU. Data from H.E.S.S. IU is not analysed within this work.

Figure 3.5: Photograph of the H.E.S.S. telescope array (with friendly permission of K. Valerius).

3.5 Data taking

Observations take place during moonless nights. Furthermore it is required that the atmosphere is in a good state, which means no clouds and no distant lightning are present. In the regular observation mode one observation takes 28 min, and is called a “run”. Most of the time a source of interest is not observed directly but with an observation offset of 0.°5 or 0.°7 (this is the so-called “wobble mode”) and the offset will be alternated in Right Ascension and Declination between runs. Technically it is possible to split the array into multiple sub-arrays to observe several sources at the same time. However this is only used to take observations with CT5 alone (called “mono mode”), while at the same time observations with CT1 to CT4 are done (called “stereo mode”). Joined observations with both telescope types are called hybrid mode.

The trigger system of H.E.S.S. has several stages. First within the telescope it is required that several pixels in a group of adjoining pixels are above a given threshold. If so, the telescope will send a trigger signal to the central array trigger. For CT5 mono events are allowed which means the central trigger will always send a read-out signal back to CT5 after receiving a trigger from it. For CT1-CT4 a read-out signals would only be sent, if at least two telescopes of CT1-CT5 triggered within a coincidence window of 60 ns (Abdalla et al., in preparation).

After receiving a read-out signal the cameras are read out. The analogue signal of the photo multiplier tubes (PMT) is converted by an analogue-to-digital converter (ADC) in the camera electronics. This is done in two channels using different amplifications to increase the range. These channels are called high gain (HG) and low gain (LG). The recorded camera image, containing the ADC information of each pixel, is sent to a central computer. Events from the single telescopes are merged according to their read-out pattern and stored to disk.

Within H.E.S.S. two independent calibration and analysis chains are available, the so-called Paris and HAP analysis. Some parameters are defined in a slightly different way.Within this work the HAP analysis was used. Therefore definitions and number given only apply to this chain.

3.6 Calibration

Before the recorded data can be analysed they have to be calibrated. During calibration the following tasks have to be completed:

- Converting ADC counts into photo electrons (p.e.)
- Identification of bad pixels
- Calculation of the optical efficiency

The ADC to p.e. conversion is done by the following equations:

$$A^{\mathrm{HG}} = \frac{\mathrm{ADC}^{\mathrm{HG}} - P^{\mathrm{HG}}}{\gamma_e^{\mathrm{ADC}}} \times \mathrm{FF},$$
$$A^{\mathrm{LG}} = \frac{\mathrm{ADC}^{LG} - P^{LG}}{\gamma_e^{\mathrm{ADC}}} \times \frac{\mathrm{HG}}{\mathrm{LG}} \times \mathrm{FF}. \tag{3.4}$$

P^{HG} and P^{LG} are the pedestal position. This is the signal read out, if no photons from a shower have been seen. The pedestal position is determined during observations in small time windows to account for changes in the position due to change of the temperature of the electronics or NSB conditions.

γ_e^{ADC} is the gain per photo electron in the high gain channel. It is determined in special calibration runs where the camera is illuminated with a defused LED or defused laser. The light intensity is roughly 1 p.e. per pixel.

$\frac{\mathrm{HG}}{\mathrm{LG}}$ is the ratio of the two gains of the two channels derived from the overlapping range. The cameras used in H.E.S.S. are read out in two channels to increase the dynamic range. The high gain channel is used for low illumination (< 150 p.e.) and the low gain for high illumination (> 200 p.e.). In the intermediate range a weighted average is used. The amplification of the low gain channel cannot be determined from single photon events, therefore the amplification ratio $\frac{\mathrm{HG}}{\mathrm{LG}}$ of both channels is used. For each event, if the charge measured is in the overlapping region, the ratio between the measurement HG and LG is computed.

FF is the flat-field coefficient, this is needed to account for relative efficiency of each pixel. It is determined from special flat-fielding runs, in such a run the camera is illuminated homogeneously from the different pixel response the coefficient is calculated (Aharonian et al., 2004).

Bad pixels, more commonly known as broken pixels, have various reasons. Some are caused by damaged or malworking hardware. Some pixels are turned off to prevent damage from intense starlight. Independent of the individual reason they have to be identified and excluded from further analysis.

The muon detection efficiency or optical efficiency is needed to determine the efficiency of the cameras to record Cherenkov light. A muon event has a very typical ring-like shape (see Fig. 3.6) and from the diameter of the ring it is possible to derive the kinetic energy of the muon. With this information the amount of Cherenkov photons produced by the μ in the atmosphere can be calculated. By comparing this number with the photons seen in the image, one can calculate the muon efficiency. For a detailed documentation I recommend Mitchell (2016).

After the calibration is done, DST files are written where the calibrated data is stored with all the additional information that is necessary for further analysis.

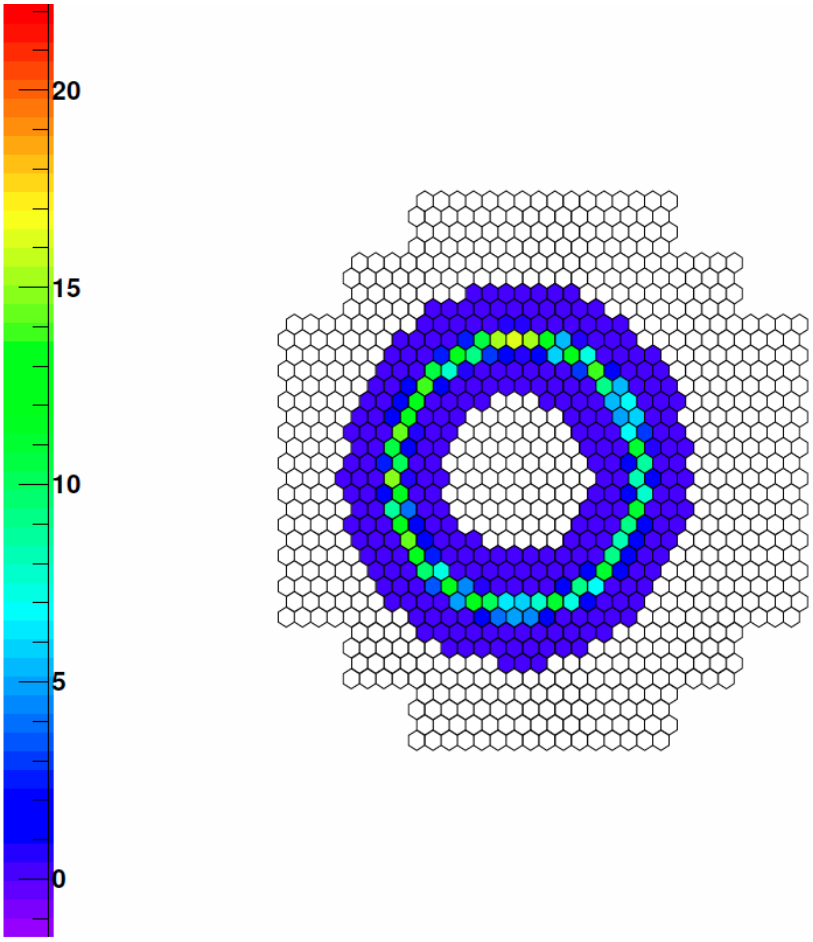

Figure 3.6: Image of a muon ring seen by CT1 in the camera plane. Figure taken from Mitchell (2016).

3.7 Data selection

Not every run can be used for high level analysis. Sometimes the quality of data is not sufficient. This can be due to hardware issues or an unstable atmosphere. In the following I will introduce the various parameters of interest for monitoring the data quality and explain which part of the system can be monitored by them.
The **Duration** of a run is 28 min. Reasons for shorter runs are: At the end of night one shorter run might be scheduled to use all the available dark time. In the regular operation, runs get aborted due to unexpected behaviour of telescopes. In the raining season observations have to be stopped to prevent damage by rain. The Duration is an array wide parameter.
The **Transparency Coefficient** is a calculated value containing information about pixel gain, muon efficiency and zenith corrected trigger rate. It characterizes the quality of the atmosphere (Hahn et al. (2013) and Hahn et al. (2014)).

The following parameters are monitored for each telescope individually:

- The **Telescope Participation fraction** (`Participation_frac`) is the fraction of events a telescope was triggered within an observation run. It can be used to monitor the homogeneous distribution of events across the system. A low value indicates either hardware problems or a lower optical efficiency of a single telescope.

- The **Tracking Precision**: For the tracking the mean deviation in Right Ascension (`RA_Dev_mean`) and Declination (`Dec_Dev_mean`) is monitored as well as the RMS of the deviation in altitude (`Alt_Dev_rms`) and azimuth (`Az_Dev_rms`). These values can be used to monitor that the drive system of the individual telescopes is working with the intended precision.

- The number of **Broken Pixels** is a criterion for how well the camera was working during a run. For the actual quality criteria it is separated into two parameters, `Num_HV_Turned_Off`, which is the number of pixels with the power supply turned off, and `Num_Hardware`, i.e. the number of pixels with unusual behaviour. A high number of broken pixels leads to information loss resulting in a worse event reconstruction.

- A change in the **Trigger Rate** can indicate clouds passing through the FoV (see Fig. 3.7). It can also be an indication for dust or haze. Two performance indicators are used: `True_Rate_Delta_1` which is a measurement of the relative change in trigger rate and `True_Rate_Delta_2`. The latter is a measurement of the fluctuation in the trigger rate (Hahn et al., 2013).

The standard cuts used in the HAP analysis are shown in Table 3.2. Currently no definition for the transparency coefficient exists for H.E.S.S. II data. Therefore a cut on this value is only applied to H.E.S.S. I data.

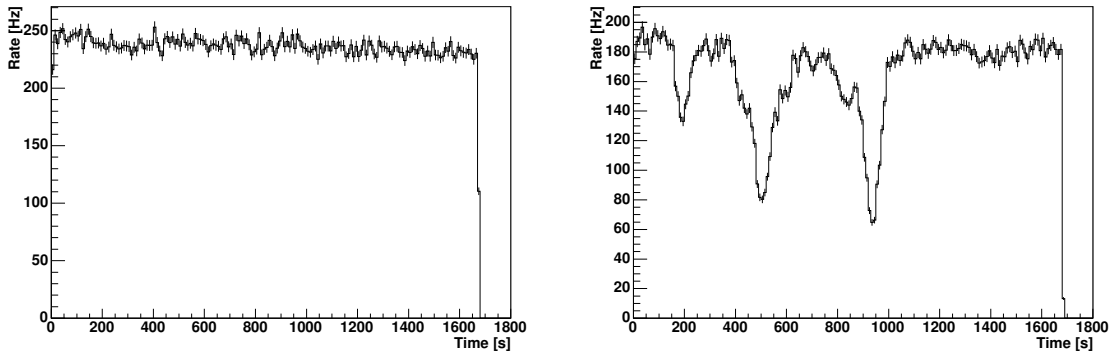

Figure 3.7: This graphic shows the trigger rate over time for two observation runs. On the left: The atmosphere was in a good condition, the rate is very stable. On the right: Several drops in the rate are visible, they can be associated with clouds moving trough the FoV (Aharonian et al., 2006b).

Table 3.2: Shown are the data quality cuts used in this work, all listed cut values are standard at the time of writing this thesis. The first two columns give the database table and parameter name. Column three gives the cuts applied to the four small telescopes. Column four shows cuts applied to CT5 in the H.E.S.S. II data set.

Table name	Parameter		
Monitor_Run_Data	Duration	>600 s	
Monitor_Run_Atmosphere	TransparencyCoefficient_mean	[0.8,1.2]	
		CT1-CT4	CT5
Monitor_Run_Tracking	RA_Dev_mean	±1’	±1’
Monitor_Run_Tracking	Dec_Dev_mean	±1’	±1’
Monitor_Run_Tracking	Az_Dev_rms	<10”	<10”
Monitor_Run_Tracking	Alt_Dev_rms	<10”	<10”
Monitor_Run_Trigger	True_Rate_Delta_1	±30%	±30%
Monitor_Run_Trigger	True_Rate_Delta_2	±10%	±10%
Monitor_Run_Trigger	True_Rate_mean	-	> 1200 Hz
Monitor_Run_Pixel	Num_HV_Turned_Off	<50	<80
Monitor_Run_Pixel	Num_Hardware	<120	<150

3.8 Image Cleaning

Before a recorded shower image is analysed, an image cleaning is performed. The purpose of this cleaning is to get rid of pixel noise. To remove noise one can take advantage of the fact that shower images are a cluster of pixels with compared to the noise, high photo electron values. For the cleaning, all recorded pixel values are set to 0 if the pixel itself is below 5 photo electrons (p.e.) and has no neighbour with at least 10 photo electrons and vice versa. Another often used cleaning is using the values 4 and 7 for pixel intensities. The standard cleaning is using 5 p.e. and 10 p.e. as values.

3.9 Event reconstruction

In order to derive information about the primary particle of a shower, it is necessary to reconstruct the shower images. Within the HAP software several methods can be selected. In this thesis the so-called Hillas and ImPACT reconstruction were used. Both methods make use of the fact that air-shower images from γ-ray events have a characteristic elliptical shape. In the following subsections I will introduce the two reconstruction methods.

3.9.1 Hillas reconstruction

The Hillas reconstruction is named after Michael Hillas who published a famous paper on how to separate γ-ray showers from hadronic background (Hillas, 1985). The shower image of a γ ray can be approximated by an ellipse.

Hillas Parameter

Important parameters for further analysis are:

- the Image Amplitude (A, sum over all photo electrons after image cleaning), used for energy reconstruction of the primary particle
- width (w) and length (l) of the photo electron distribution, used for γ/hadron separation
- nominal distance (d), the distance of the image centre of gravity to the camera centre
- orientation of the major axis (α), used for direction reconstruction (Aharonian et al., 2006b).

An illustration of these parameters can be seen in Figure 3.8.

The Hillas parameter can be calculated from the first and second moment of the intensity distribution (de Naurois, 2012):

$$\begin{aligned} \langle x\rangle &= \frac{\sum_i x_i a_i}{\sum_i a_i}, \langle y\rangle = \frac{\sum_i y_i a_i}{\sum_i a_i} \\ \langle x^2\rangle &= \frac{\sum_i x_i^2 a_i}{\sum_i a_i}, \langle y^2\rangle = \frac{\sum_i y_i^2 a_i}{\sum_i a_i}, \langle xy\rangle = \frac{\sum_i x_i y_i a_i}{\sum_i a_i} \end{aligned} \tag{3.5}$$

with x_i, y_i the coordinates of a pixel with intensity a_i. With the help of the variances and covariance:

$$\sigma_{x^2} = \langle x^2\rangle - \langle x\rangle^2, \sigma_{y^2} = \langle y^2\rangle - \langle y\rangle^2, \sigma_{xy} = \langle xy\rangle - \langle x\rangle\langle y\rangle \tag{3.6}$$

and the intermediate variables:

$$\begin{aligned} \Xi &= \sigma_{x^2} - \sigma_{y^2}, \qquad z = \sqrt{\Xi^2 + 4\sigma_{xy}} \\ b &= \sqrt{\frac{(1+\Xi/z)\langle x\rangle^2 + (1-\Xi/z)\langle y\rangle^2 - 2\sigma_{xy}\langle x\rangle\langle y\rangle}{2}} \end{aligned} \tag{3.7}$$

we can now write the Hillas parameters as:

$$
\begin{aligned}
d &= \sqrt{\langle x \rangle^2 + \langle y \rangle^2} \\
l &= \frac{\sigma_{x^2} + \sigma_{y^2} + z}{2} \\
w &= \frac{\sigma_{x^2} + \sigma_{y^2} - z}{2} \\
\alpha &= \arcsin \frac{b}{d} \\
A &= \sum_i a_i
\end{aligned}
\tag{3.8}
$$

Direction reconstruction

To reconstruct the direction of a shower one has to calculate the intersection point of the major axis seen in different cameras (see Fig. 3.9).

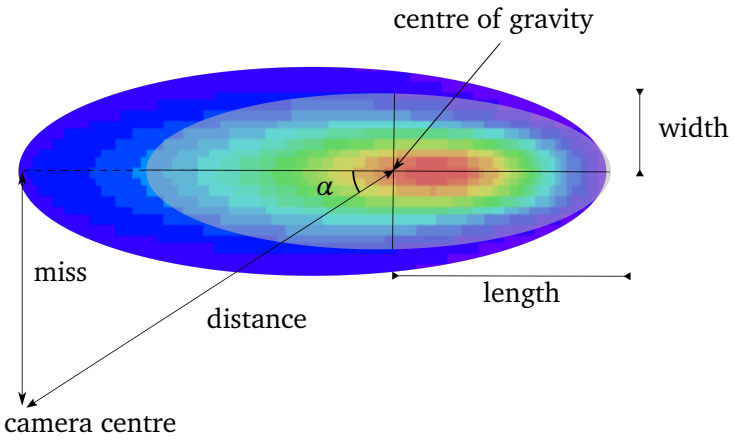

Figure 3.8: Shower image of a simulated γ ray, the color scale indicates the intensity of the image in arbitrary units. The most important shower properties after Hillas (1985) are shown.

In reality the major axes do not intersect at the same point, when the shower is seen by more than two telescopes. To account for that, a weighted sum is calculated according to Equation 3.9:

$$
S = \frac{\sum\limits_{\substack{j,k,\\ k>j}} S_{j,k} \cdot \sin\alpha \cdot \dfrac{1}{\frac{1}{A_j} + \frac{1}{A_k}}}{\sum\limits_{\substack{j,k,\\ k>j}} \sin\alpha \cdot \dfrac{1}{\frac{1}{A_j} + \frac{1}{A_k}}},
\tag{3.9}
$$

where $S_{j,k}$ is the intersection point of the axis seen by telescopes j and k, α the intersection angle, and A_j, A_k are the image amplitudes. Due to the weighting by the image amplitude bright images, the axis is well defined, are more impactful. The weighting by $\sin\alpha$ has the result that axes with

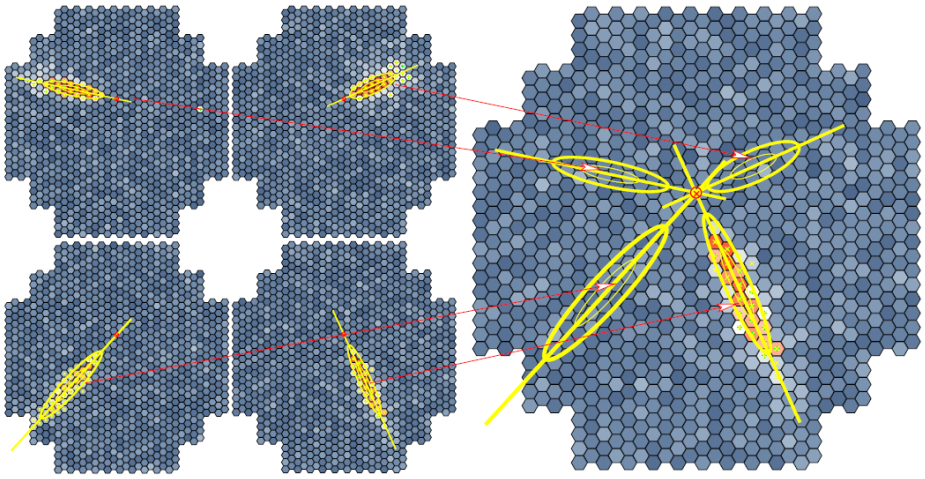

Figure 3.9: The left side shows images of a shower seen by four telescopes. The right side shows the Hillas ellipses projected into a common camera plane. The intersection point of the major axis indicates the reconstructed direction. Figure taken from Völk & Bernlöhr (2009).

small intersection angle have a smaller impact, in this case small deviations would result in a large shift of the intersection point.

As described in Hillas (1985) the length and width can be used to distinguish between γ and hadrons. γ-like showers are more elliptical.

Energy reconstruction

The energy can be reconstructed using the image amplitude, the zenith angle, optical efficiency, distance from the main shower axis to the telescope and the distance of the CoG to the camera centre. The information of the dependency of the energy on these values is stored in a look-up table which is produced from simulations. One example of such a table can be seen in Figure 3.10. The energy is obtained by interpolation of several neighboured tables. It is important to apply a correction taking the optical efficiency of the telescope into account. Otherwise the energy would be biased due to the fact that look-ups only exist for a fixed set of optical efficiencies.
After estimating the energy for every telescope the weighted mean value is calculated over all telescopes participating in the shower:

$$E = \frac{\sum_i E_i}{\sum_i \delta_i^{-2}}, \tag{3.10}$$

where E_i is the energy reconstructed in telescope i and δ_i the RMS of the reconstructed energy derived from simulations.

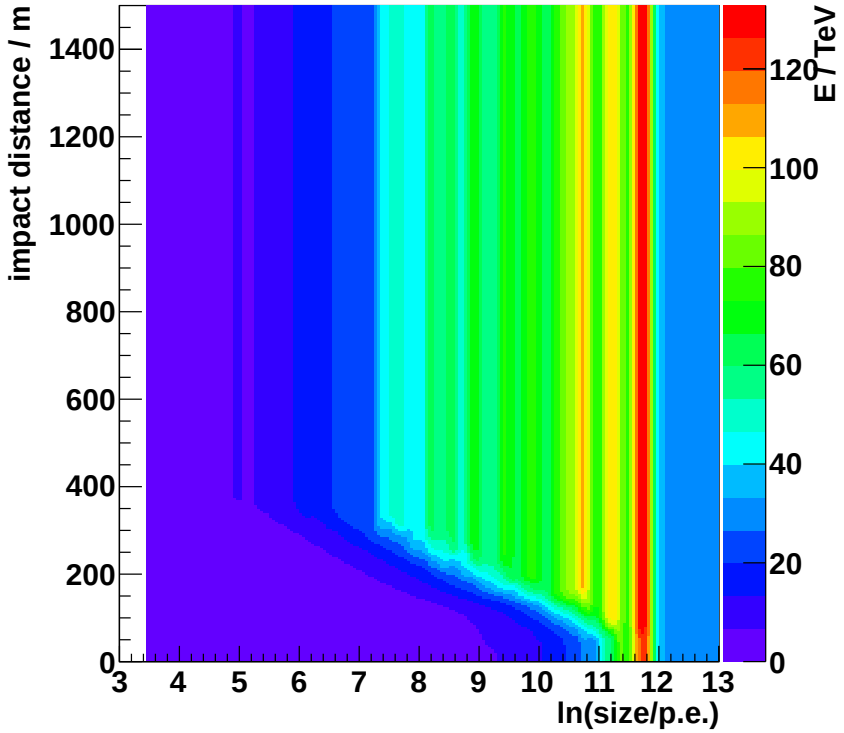

Figure 3.10: Energy look-up table for CT1. Shown is the energy depending on impact distance (distance of the shower axis in the atmosphere to the telescope) and image amplitude (size).

3.9.2 ImPACT

To improve the shower reconstruction over the Hillas reconstruction one can use more advanced techniques such as the Image Pixel-wise fit for Atmospheric Cherenkov Telescopes (ImPACT) (Parsons & Hinton, 2014). In this approach Monte-Carlo simulation-based shower-image templates are compared with the photo electron distribution in the camera plane using a likelihood function developed by de Naurois & Rolland (2009). In order to generate the image templates, a large number of Monte-Carlo generated events is needed. The probability to see s photo electrons in a pixel is given by:

$$P(s;\mu,\sigma_p,\sigma_\gamma) = \sum_n \frac{\mu^n e^{-\mu}}{n!} \times \frac{\exp\left(-\frac{(s-n)^2}{2(\sigma_p^2+n\sigma_\gamma^2)}\right)}{\sqrt{2\pi(\sigma_p^2+n\sigma_\gamma^2)}}, \tag{3.11}$$

with μ being the model expectation, σ_p being the pedestal width and σ_γ the width of the single photo electron distribution. The first term of the equation describes the Poisson probablity to detect n photo electrons when expecting μ from the model. The second term describes the resolution of the sensor. In the case of a large number of predicted photons the likelihood can be simplified to:

$$P(s;\mu \gg 0,\sigma_p,\sigma_\gamma) = \frac{1}{\sqrt{2\pi(\sigma_p^2+\mu(1+\sigma_\gamma^2))}} \times \exp\left(-\frac{(s-\mu)^2}{2(\sigma_p^2+\mu(1+\sigma_\gamma^2))}\right). \tag{3.12}$$

In this case the Poissonian signal term can be replaced by a Gaussian.
Using the ImPACT method energy and direction are reconstructed by finding the best fitting template.

Advantages of the ImPACT reconstruction over the Hillas are a better angular resolution leading to a better sensitivity and a better energy reconstruction, but it requires a very good understanding of the Monte Carlo simulations used to generate the image templates.

3.10 Background rejection

Since most air showers seen by H.E.S.S. are of hadronic nature, it is important to suppress this background. It is partly suppressed due to the stereoscopic trigger. Air-shower images from γ events have a characteristic elliptical shape, while hadronic shower images often contain several sub-showers resulting in a less regular shower shape and sometimes several isolated islands of high intensity within an image. This can be seen in Figure 3.11. Separation can be done in different ways. Within the HAP-software framework two methods are utilized to get rid of hadronic events. One is a simple cut on various shower parameters, where you require that the value of this parameter is in a typical range for γ-ray events. The most important parameters are the mean

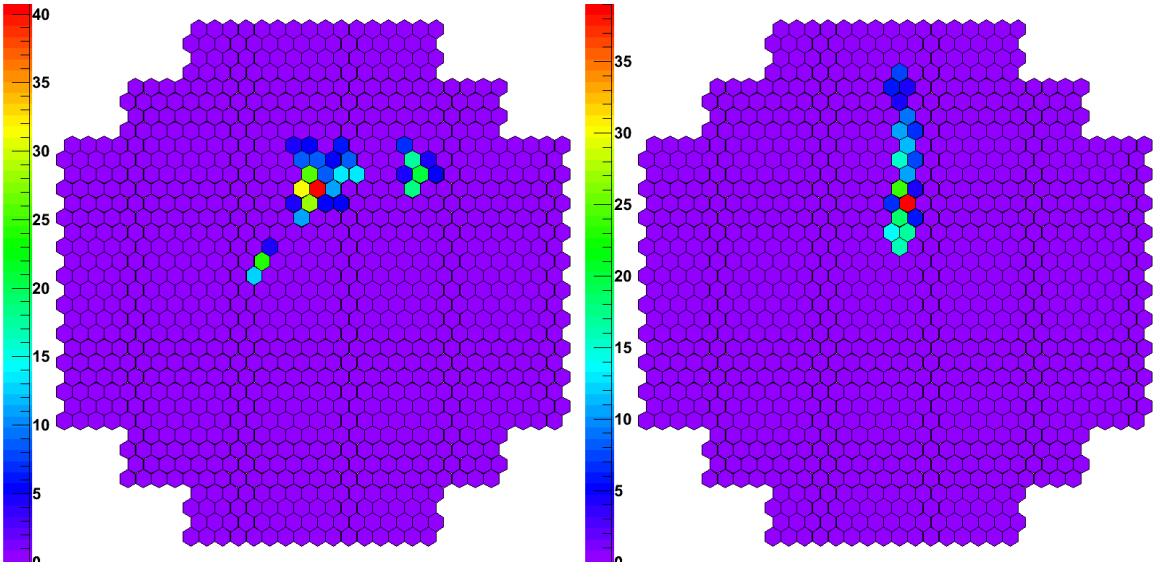

Figure 3.11: The shower on the left side is the image of a simulated proton with a primary energy of 0.9 TeV. The different islands in the image belong to several sub-showers. On the right side a simulated γ-ray image with 0.4 TeV energy can be seen. This image has the characteristic elliptical shape. Both images are shown after image cleaning.

reduced scaled width (MRSW) and the mean reduced scaled length (MRSL). They are defined as:

$$\begin{aligned} \text{MRSW} &= \frac{1}{N_{tel}} \sum_{\text{tel}} \frac{w - \langle w \rangle}{\sigma_w}, \\ \text{MRSL} &= \frac{1}{N_{tel}} \sum_{\text{tel}} \frac{l - \langle l \rangle}{\sigma_l}, \end{aligned} \tag{3.13}$$

with w/l being the Hillas width/length reconstructed from the image, $\langle w \rangle / \langle l \rangle$ the expected width/length determined from γ-ray simulations for showers with the same image amplitude, zenith angle and impact distance and σ_w/σ_l the scatter of the parameter (Aharonian et al., 2006b). One example for such a distribution of MRSW can be seen in Figure 3.12.

The other method used to suppress background is based on a boosted decision tree (BDT). The algorithm used within HAP is provided by the ROOT package Toolkit for Multivariate Data Analysis (TMVA) (Ohm et al. (2009) & Hoecker et al. (2007)). In this method a BDT is trained with γ-ray and hadron simulations. Training parameters are:

- Parameters derived from the Hillas length and width
- Depth of the shower maximum in the atmosphere
- The average spread for the reconstructed energy between telescopes $\frac{\delta E}{E}$

After the training the algorithm is able to distinguish both shower types to a certain degree. The output of the BDT can be seen in Figure 3.13 (bottom). With a cut on the ζ parameter, a separation can be achieved.

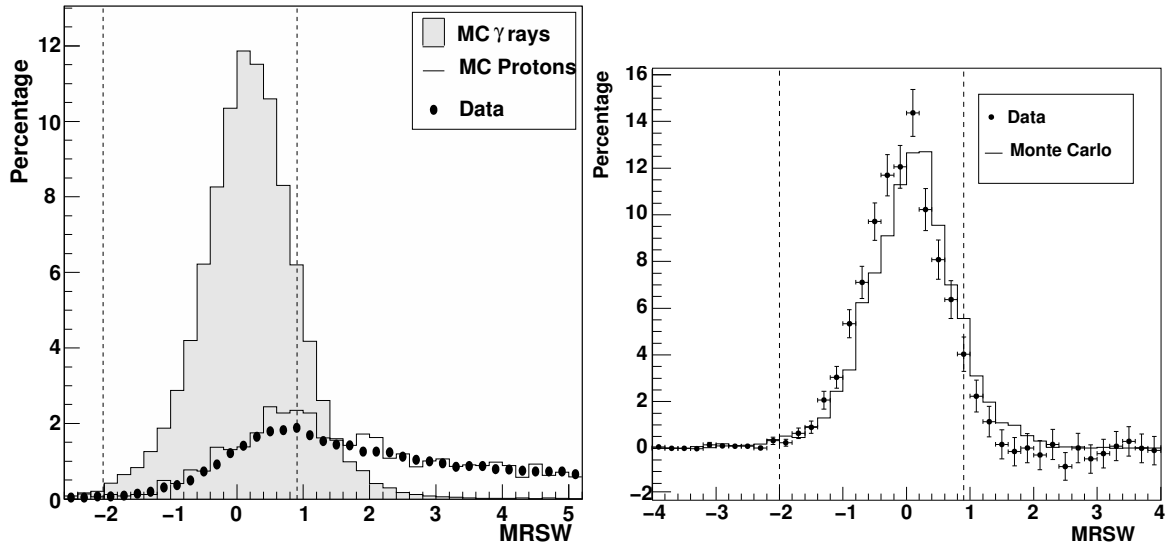

Figure 3.12: The distributions for the MRSW. The range where events are treated as γ-ray like is indicated by dotted lines. Left: Monte Carlo γ ray, MC protons and data from a region where no γ-ray source is located. Right: Data from the direction of the Crab nebula and Monte Carlo γ. The vertical dashed lines indicate the γ-like range used during the analysis. Figure taken from Aharonian et al. (2006b).

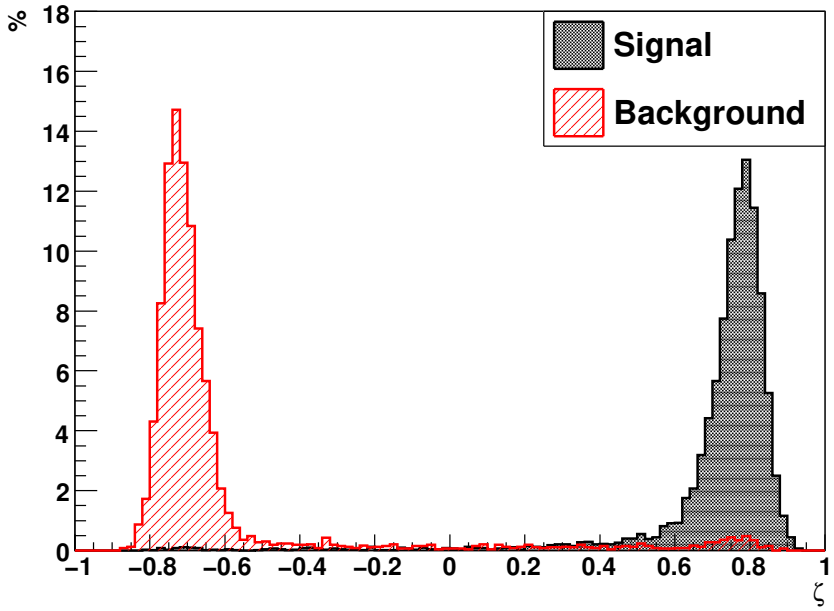

Figure 3.13: Distribution of the output parameter ζ from the BDT for a sample of signal and background events. Figures taken from Ohm et al. (2009).

In the analysis used here, a combination of both methods was utilized. In a first step simple cuts on the image amplitude and position of the shower within the camera were performed, so-called preselection cuts. This is done to remove images with insufficient quality and preselect showers. After that the TMVA algorithm is used to remove hadrons from the data sample.
Cuts are done on the following parameters:

- Image Amplitude – to ensure that the analysed camera images are bright enough for a well determined parametrisation
- local distance – to remove images too close to the edge of the camera, which might be partially cut by the edge
- Multiplicity – to ensure that only stereoscopic events are analysed
- ζ BDT – for the actual γ-hadron separation

Figure 3.14 (top) shows the energy resolution for analyses based on Hillas and ImPACT reconstruction. The resolution for the Hillas based analysis H.E.S.S. I std (black triangle) and H.E.S.S. II hybrid (red dashed curve) are almost the same. Only at energies above $\approx 12\,\text{TeV}$ the performance of the five telescope array is better than using only the four small telescopes. The ImPACT-based analysis (red dots) shows a better energy resolution in almost the entire energy range up to $\approx 60\,\text{TeV}$. When using the ImPACT configuration, using four and five telescope events only (green square), the resolution becomes better compared to the regular ImPACT configuration where events with multiplicity ≥ 2 are used. The resolution stays below 10 % in the relevant energy range (0.1 – 30 TeV).

All energy bias curves show the typical shape. At low energies the bias is above 0. This comes from the fact that only bright events are seen. Events with under fluctuation in the Cherenkov photon production end up below the threshold. At medium energies all events can be seen resulting in bias around 0 and at high energies shower images can become to large for the camera. This leads to an underestimation of the energy, since only a fraction of the produced light is collected. The energy bias (Fig. 3.14 bottom) is for both ImPACT based analyses almost identical. At low energies the bias is much smaller compared to the Hillas based analysis and therefore reducing the energy threshold.

The effective area (Fig. 3.15) above $\approx 1\,\text{TeV}$ is for all shown configurations almost the same. Below 1 TeV the ImPACT configuration using only high multiplicity events (green square) shows the smallest effective area. This behaviour is expected, due to the very restrictive event selection.

3.11 Background subtraction

After the γ-hadron separation the remaining event sample still contains events not induced by γ rays. This comes from e^-, which have almost the same shower shape as γ-ray shower and from hadronic shower, where in one of the first interactions a high energy photon was produced. The result is a shower which is dominated by the electromagnetic component and therefore similar in

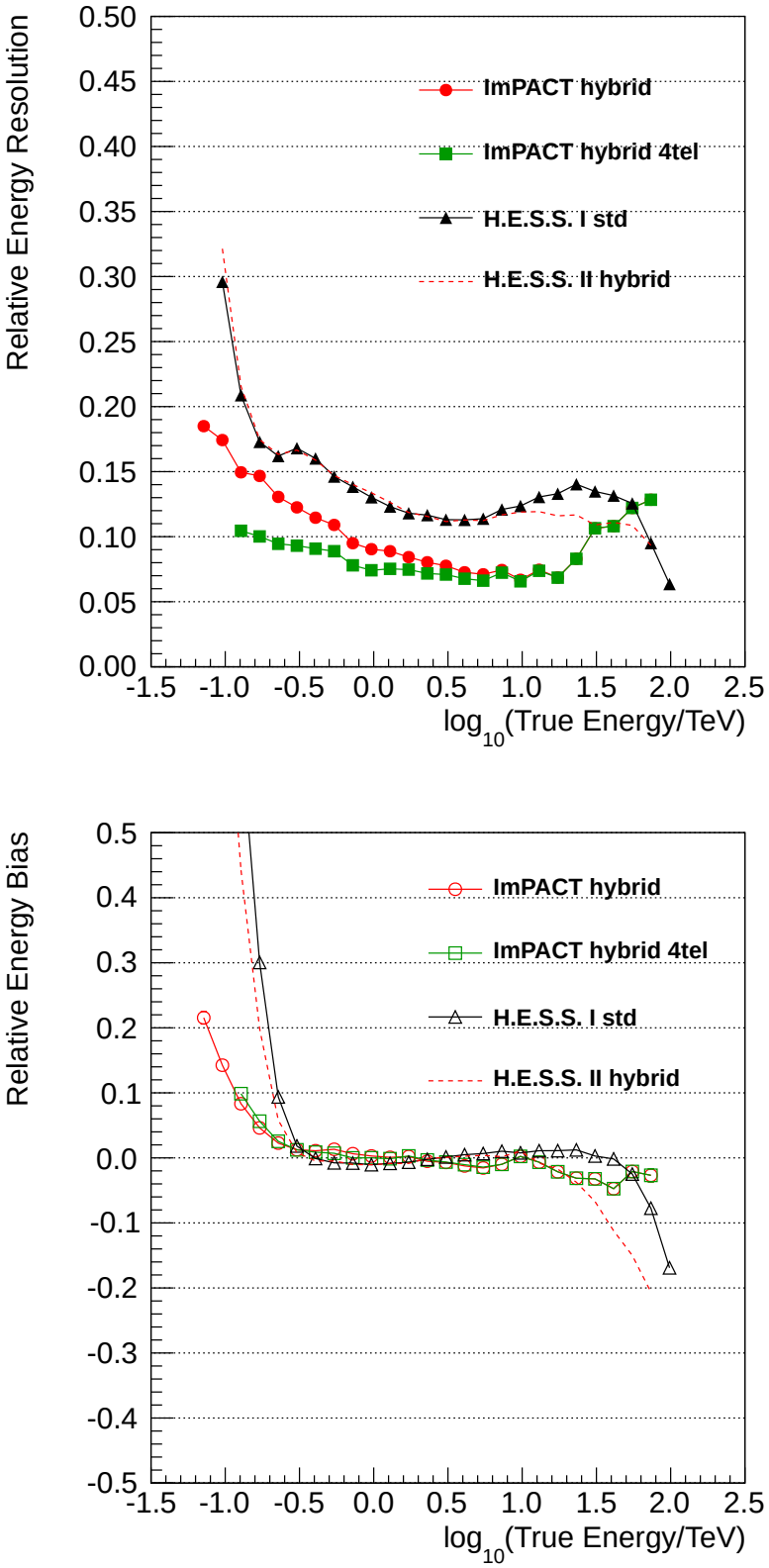

Figure 3.14: Energy resolution (top) and energy bias (bottom) curves for different cut configurations. All curves come from simulation of a point source at 10° zenith and 180° azimuth angle observed with a 0.°5 wobble offset.

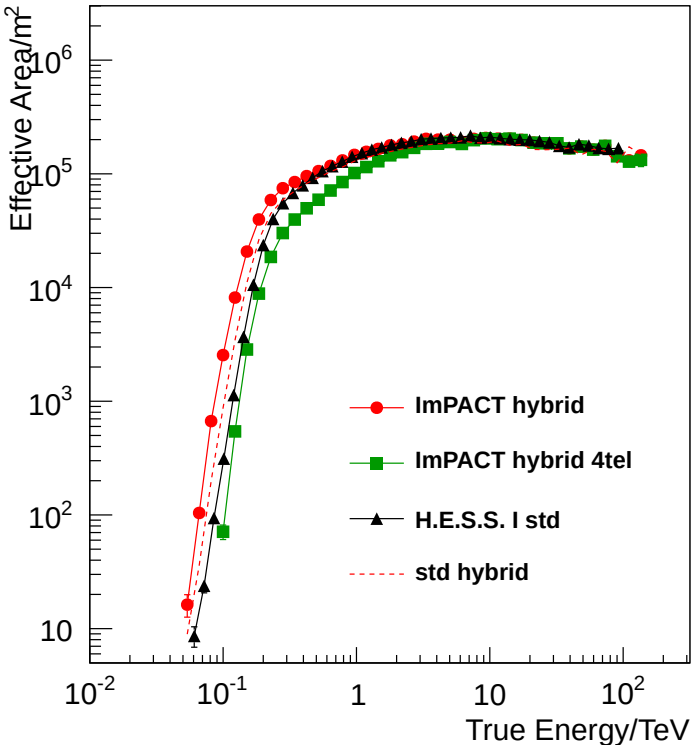

Figure 3.15: Effective area curves for different cut configurations. All curves come from simulation of a point source at 10° zenith and 180° azimuth angle observed with a 0.°5 wobble offset.

its shape as a pure electromagnetic shower. In order to take this into account, several background subtraction methods have been developed. They all have in common that an On region is defined which contains the source region of interest. In a second step the contamination is estimated by using Off regions considered to be free of γ-ray sources. The γ-ray excess can now be estimated by

$$N_{\text{excess}} = N_{\text{On}} - \alpha N_{\text{Off}} \tag{3.14}$$

where α is a normalization factor and $N_{\text{On/Off}}$ the number of events in the On/Off region. Depending on the background subtraction method the α factor absorbs information about the difference in area, livetime and acceptance between the On and Off regions.
The most commonly used background subtraction methods are the so-called RingBackground method, used to calculate sky maps, and ReflectedBackground method, used to calculate source spectra. In the analysis presented in this thesis I am also using another method called OnOffBackground, which can be used to calculate both maps and spectra.
In the following these three methods are introduced.

3.11.1 RingBackground

The RingBackground method is used to calculate excess and significance maps. For a particular position on the sky, a circular On region is defined and a ring shaped Off region which surrounds the On region. An example for such regions can be seen in Figure 3.16 left side.
By sliding these On and Off regions over the count map one can estimate the contamination at

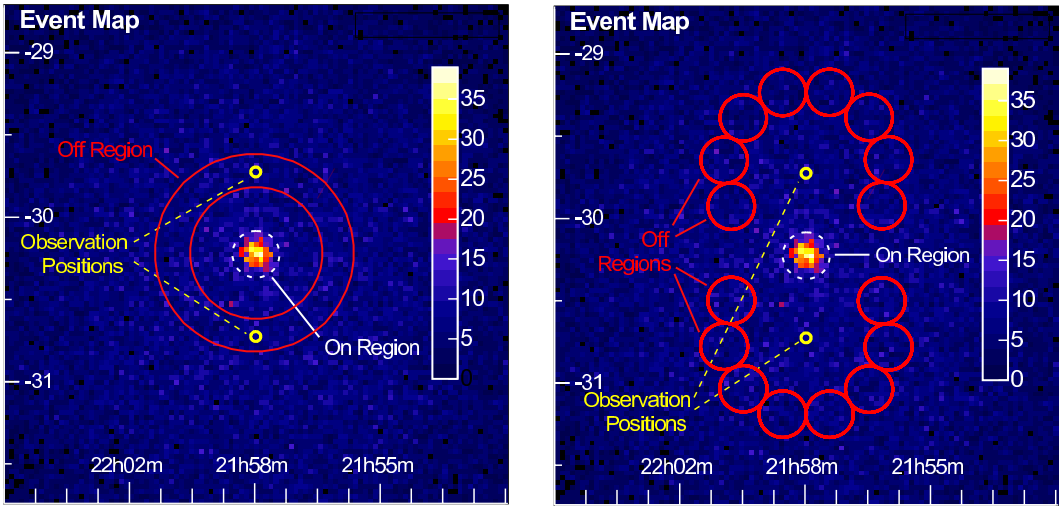

Figure 3.16: This Figure shows a count map for PKS 2155–304. Left: RingBackground method. The On-region is illustrated with a white dashed line, the corresponding Off-ring is shown with a red ring. Right: ReflectedBackground method. Two different pointings are shown and the corresponding reflected background regions are illustrated by red circles. Figures taken from Berge et al. (2007).

each position. However, with this procedure the On and Off region have different sizes and are at different angular distances from the observation position. Since the acceptance of the H.E.S.S. array is dependent on this angle, it is necessary to correct for this effect. Therefore a look-up table has to be filled, from source free regions, with a so-called radial acceptance curve. In Figure 3.17

an example for radial acceptance curves for three zenith angles is shown. As is clearly seen, the acceptance is falling steeply with increasing distance to the optical axis. From such a radial model

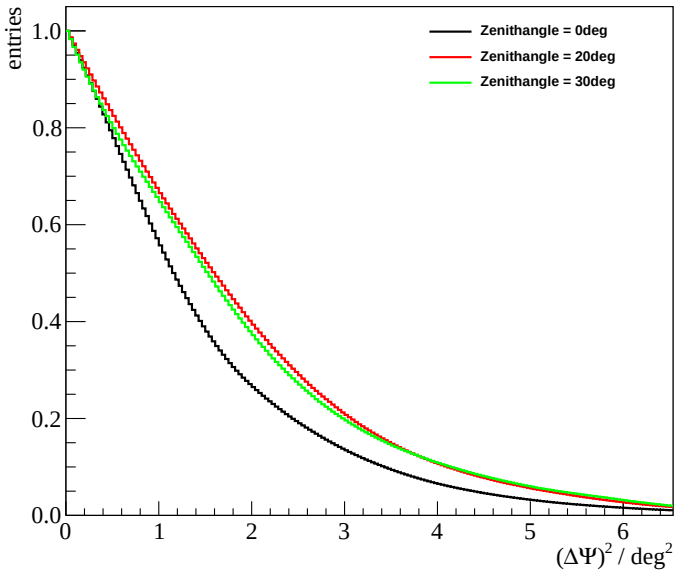

Figure 3.17: Radial Acceptance curves for different zenith angles. The abscissa shows the quadratic distance from the observation position. The ordinate shows the relative acceptance for background events, it is generated from regions in the sky where no known source is located.

we can calculate the so-called exposure map for the On and Off map (see Figure 3.18), containing in each bin the information of the relative exposure. By dividing the On exposure map by the Off exposure map we get the so-called alpha map (see Figure 3.19). The alpha map contains the scaling of the Off events to account for the falling acceptance, for every pixel in the map. In this case the α factor contains information about the area ratio corrected for the different acceptances. One can now calculate the excess for the bin (i,j) in the map as:

$$\text{Excess}(i,j) = \text{exposure}_{\text{On}}(i,j) \times \text{N}_{\text{On}}(i,j) - \alpha(i,j) \times \text{N}_{\text{Off}}(i,j), \tag{3.15}$$

with $\text{N}_{\text{On/Off}}$ the number of On/Off counts in the bin (i,j).
With the available information one can also calculate the significance in a bin (i,j) with the equations given in Li & Ma (1983). The significance in a bin is given by:

$$S = \sqrt{-2\ln\lambda} \tag{3.16}$$

With λ being the maximum likelihood ratio:

$$\lambda = \left[\frac{\alpha}{1+\alpha}\left(\frac{\text{N}_{\text{On}}+\text{N}_{\text{Off}}}{\text{N}_{\text{On}}}\right)\right]^{\text{N}_{\text{On}}} \times \left[\frac{1}{1+\alpha}\left(\frac{\text{N}_{\text{On}}+\text{N}_{\text{Off}}}{\text{N}_{\text{Off}}}\right)\right]^{\text{N}_{\text{Off}}} \tag{3.17}$$

The indices i, j for $N_{\text{On/Off}}$ and α were left out in order to make equation 3.17 easier to read.

The RingBackground method is used within this thesis to derive reference significance maps in the development process of the used On-Off analysis.

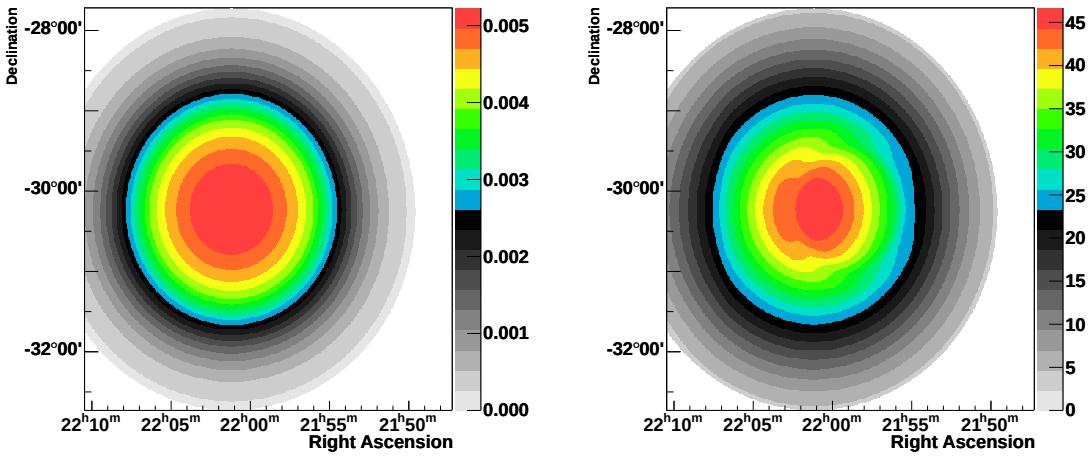

Figure 3.18: On (left) and Off (right) exposure map for an observation run taken in the vicinity of PKS 2155–304 using the RingBackground method. The asymmetry in the Off exposure map comes from regions in the sky containing a known γ-ray source, which are therefore excluded in the background estimation.

3.11.2 ReflectedBackground

The ReflectedBackground method is commonly used to calculate γ-ray spectra from sources. In this method a so-called On region is defined which contains the source to be analysed. In a second step Off regions are determined which have the same shape and offset from the centre of the FoV as the On region. By using Off regions with the same observation conditions many systematic effects cancel out. In the case of the ReflectedBackground, α (see Eq. 3.18) only carries information about the ratio of the area of the On region and the Off regions.

$$\alpha = \frac{A_{\mathrm{On}}}{\sum_i A_{\mathrm{Off}_i}} \tag{3.18}$$

with $A_{\mathrm{On/Off}}$ the area of the On/Off region. Figure 3.16 right side shows an example for two observation runs taken in the vicinity of PKS 2155–304. Red circles indicate the positions of Off regions and a dashed white circle indicates the On region. With the knowledge of α, N_{On} and N_{Off} one can calculate the detection significance of a source. From On- and Off-event lists or histograms one can calculate a source spectrum. This will be discussed in Section 3.12.

The ReflectedBackground method is used within this thesis to derive reference source spectra in the development process of the used On-Off analysis.

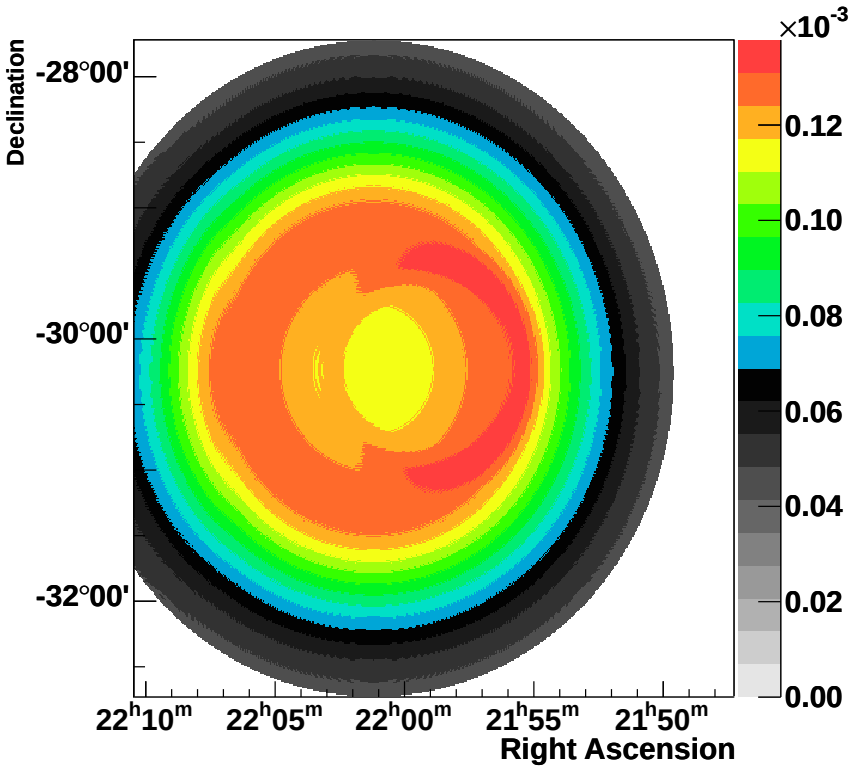

Figure 3.19: Alpha map for the same run as shown in Figure 3.18.

3.11.3 OnOffBackground

Sometimes the physics case demands an On region in a size that no Off regions can be constructed within the FoV of the run, or too many surrounding sources are within the FoV, so that no Off region can be found. In this case background can be estimated using the OnOffBackground method. Here Off regions are used from different runs than those of the actual observations of the source of interest. Most of the time this is done by dedicated observation pairs. One run is taken with the source of interest in the FoV. Immediately after the run has finished, another one is taken with as far as possible the same observation conditions. To satisfy the source conditions the run is carried out with exactly 30 min offset in Right ascension, which results in the same altitude and azimuth coverage as in the On run. An example for this observation scheme can be seen in Figure 3.20. In the scheme shown, two Off runs are taken, one immediately before the On run and one after.
For the analysis presented in this work no dedicated On-Off run pairs were taken, but runs with matching observation conditions were searched within the whole H.E.S.S. data. The method used to find matching runs will be discussed in Chapter 4.4. In order to produce maps with the On-Off method, exposure and alpha maps are produced in the similar way as for the RingBackground method.
For a spectral analysis the On events are derived from the analysis region within the On run. The Off events are derived from an Off region with the same size, shape and relative orientation to the observation position, however located in the FoV of the Off run.

Due to the fact that no dedicated run pairs are used in the analysis presented in this work, a more sophisticated method for Off event selection is discussed in Section 4.6.

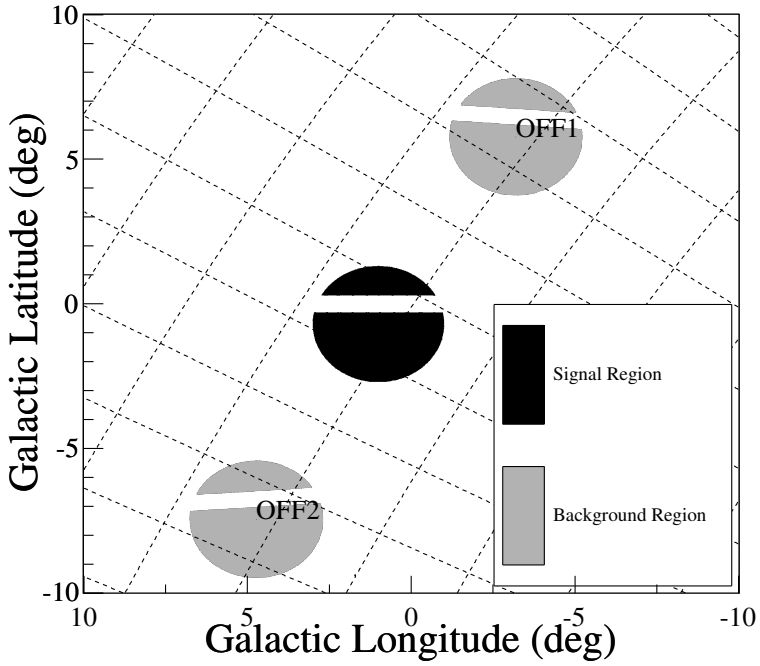

Figure 3.20: Skymap in Galactic coordinates showing the signal region (black) and the Off regions (grey) for dedicated On-Off observations done in the Galactic Centre region. Figure taken from Abramowski et al. (2015).

3.12 Spectrum reconstruction

From the event distributions as function of reconstructed energy derived with the ReflectedBackground or OnOffBackground method one can calculate the source spectrum. There are several methods to calculate a spectrum available within the HAP software framework. In this thesis the Forward folding method is used. Using Forward folding, the spectrum is fitted in bins of reconstructed energy, i.e. energy derived from the reconstruction (see Section 3.9). For simplicity a power law, given by:

$$F(E_{\mathrm{true}}) = n \times \left(\frac{E_{\mathrm{true}}}{E_0}\right)^{-\Gamma} \tag{3.19}$$

with $F(E_{\mathrm{true}})$ the differential flux at the energy E_{true}, n the flux normalization at reference energy E_0 and Γ the spectral index, is used as a model. In order to estimate for a given flux assumption the number of counts in a given bin (with bin edges E_1, E_2) in reconstructed energy (E_{reco}) we need to fold the model function with the energy migration (P) and multiply by the livetime (T) and effective area (A):

$$N(E_{\mathrm{reco}}) = \int_{E_1}^{E_2}\int_{0}^{\infty} P(E_{\mathrm{true}}, E_{\mathrm{reco}}) \times F(E_{\mathrm{true}}) \times A(E_{\mathrm{true}}) \times T(E_{\mathrm{true}})\, \mathrm{d}E_{\mathrm{true}}\mathrm{d}E_{\mathrm{reco}}. \tag{3.20}$$

For better readability, the dependence of P, A and T on different observation conditions (zenith angle, wobble offset, azimuth angle), used analysis cuts and telescope state were left out in Equation 3.20.
The livetime is the deadtime corrected observation time. An example for the effective area can be seen in Figure 3.15. The energy resolution matrix can be seen in Figure 3.21. Furthermore only events falling in the so-called safe energy range, the range where the energy bias is below 10 %, are used in the analysis. An exemplary bias curve can be seen in Figure 3.22. Once the expected counts for a bin in reconstructed energy are obtained, one can perform a χ^2 or a Likelihood fit to find the best values for n and Γ.
In the Dark Matter line search presented in this work a Likelihood fit is used which is introduced in Section 4.8.

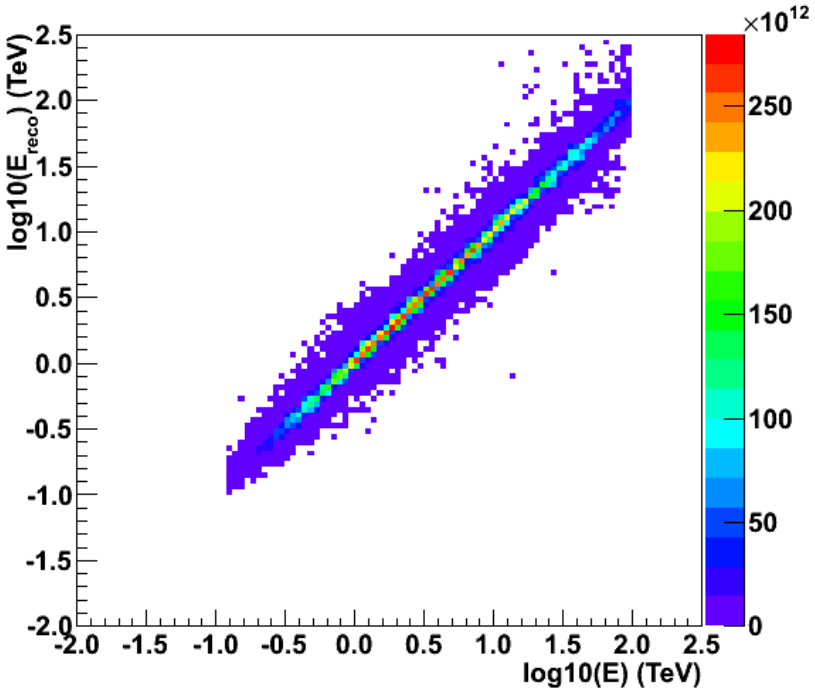

Figure 3.21: Livetime and effective area weighted Energy Migration Matrix. The abscissa shows the $\log_{10}$ of the true event energy and the ordinate shows the $\log_{10}$ of the reconstructed energy.

3.13 Analysis requirements - update

As discussed in Section 2.8 several requirements have to be fulfilled in order to perform a sensitive analysis. They were formulated as:

- A good energy resolution in order to resolve a line-like signal
- High sensitivity in the GeV to TeV energy range
- Good background suppression
- Careful selection of the analysis region

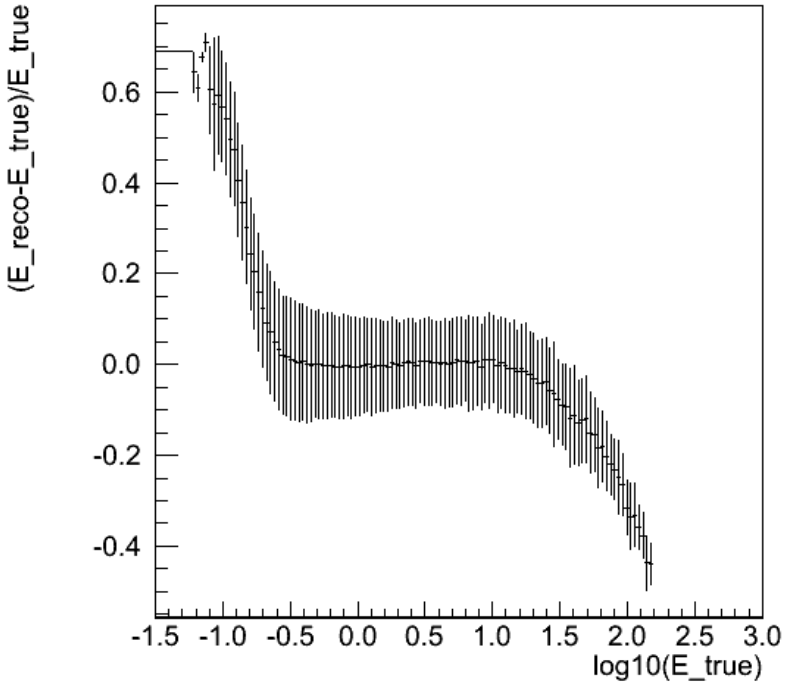

Figure 3.22: Energy Bias curve for the std_hybrid configuration. The abscissa is given in $\log_{10}(E_{\text{true}})$ and the ordinate in $\frac{E_{\text{reco}}-E_{\text{true}}}{E_{\text{true}}}$. Error bars indicate the 68 % containment region of the energy resolution. In the analysis only the range where the bias is below 10 % is used.

We have seen in Figure 3.14 that the ImPACT based analysis, using high multiplicity events only, has a low energy resolution of about 10 % over almost the entire energy range. A large effective area is provided above an energy of about 200 GeV (see Fig. 3.15) up to 100 TeV. This makes ImPACT reconstruction based analysis a good choice to fulfil the first two requirements.

Several methods can be utilized to achieve background suppression and subtraction. TMVA based γ-hadron separation provides the best separation power of the available analyses. In addition background subtraction methods can be used to achieve a better result.

With H.E.S.S. a large data set of the inner Galactic region was taken over the past years. How this data set can be used depends on the choice of an analysis region. The choice and its consequences for the analysis will be discussed in the next chapter.

Chapter 4

Development of an On-Off Analysis for a search of Dark Matter in the Galactic Centre

In this chapter I introduce the On-Off analysis developed and used in this thesis. Due to the fact that no scheduled run pairs are available for the background estimation, it is necessary to search for runs, for background estimation, with similar conditions as the runs taken in the vicinity of the Galactic Centre.
First the choice of the analysis region for the Dark Matter search is discussed, followed by the J-Factor calculation. Next I will introduce the chosen analysis configuration for event reconstruction and selection, the available data set, followed by the run selection and its results, followed by the introduction of the pairing method and the performance test of the analysis using the well known source PKS 2155–304.

4.1 Analysis region and J-Factor calculation

In order to analyse the Galactic Centre region searching for a line-like signal from Dark Matter annihilation it is necessary to carefully select the region to be analysed and either exclude known sources of γ ray or provide a reliable model for them. Due to the difficulty of developing a model precise enough for all sources in the Galactic Centre, it was decided to exclude regions with known sources.
To be sensitive to the shape of the density profile it was furthermore decided to use several analysis regions (On regions). Due to the radial symmetry of the tested profiles, a circular shape was chosen with its centre at (0,0) in Galactic Coordinates. The shapes of the individual analysis regions can be seen in Figure 4.1. The Galactic plane is excluded with a box of height 1° to account for diffuse emission along the plane. The radius of the analysed regions is from 0.°6 to 1.°5 in steps of 0.°1. Furthermore known sources were excluded and masked with circular regions.

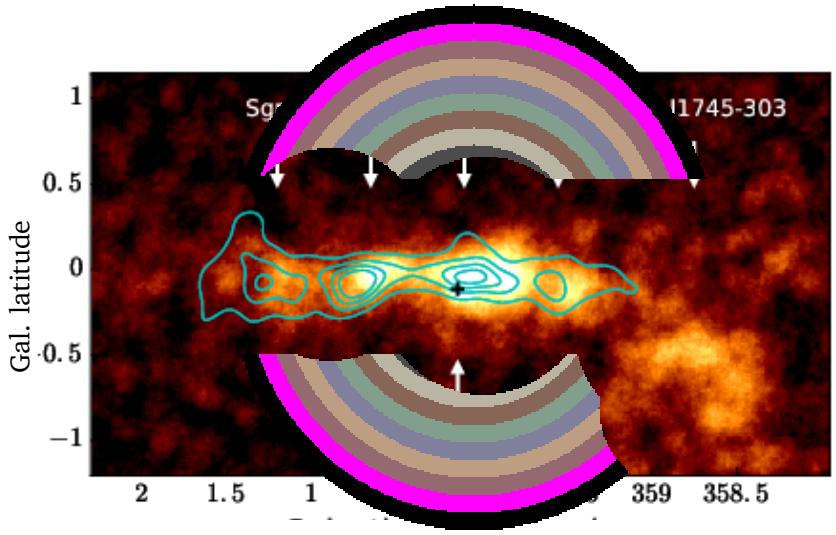

Figure 4.1: Shown is a map of the Galactic Centre in Galactic coordinates. Superimposed are the final analysis regions used in this work. The regions are counted from small (grey, 1) to largest (black, 9). All known sources of γ ray are excluded from the analysis regions. Figure adapted from Abdalla et al. (2017a).

To determine the J-Factor of each analysis region the squared density profile of the Dark Matter distribution has to be integrated along the line of sight (r) and over the solid angle of the observed region (Ω).

$$J = \int_{\text{fov}} \int_{los} \rho^2 \mathrm{d}r \mathrm{d}\Omega \tag{4.1}$$

The distance s of any point to the centre of the Milky Way is given by:

$$s = \sqrt{r^2 + s_{\text{GC}}^2 - 2r \times s_{\text{GC}} \times \cos(\alpha)}, \tag{4.2}$$

with $s_{\text{GC}} = 8.5\,\text{kpc}$, r being the distance of the point from the Earth and α the angle between the considered point and the direction to the Galactic Centre. The geometry is shown in Figure 4.2. Since there is no easy analytical solution to Equation 4.1, the integration was performed numerically. In order to find an abort criterion for the line of sight integration, different integration depths were tested. A circular test region with radius R = 0.°5 centred at the Galactic Centre was used. The inner part was cut out with a box of height 0.°6 to give the region a similar shape as the regions used in the Dark Matter search. The integral along the line of sight was calculated with the lower limit positioned at Earth and the upper limit increasing in steps of 8.5 kpc. In Table 4.1 the results for the integration can be seen. As it turns out, the J-Factor does not change by more than 1 % after two steps. However to be conservative the integration for the analysis presented here was done for five steps for both the NFW and the Einasto profile. In the following all integrations will be aborted at 5×8.5 kpc.

Due to the size of the analysis region, it is not possible to find background regions within the same H.E.S.S. FoV. This makes analysing the data using the RingBackground or ReflectedBackground

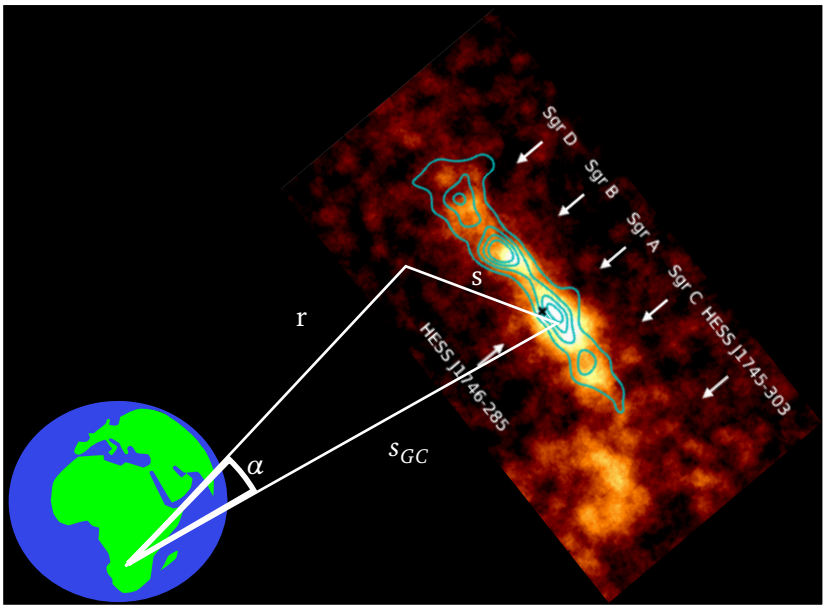

Figure 4.2: Illustration of J-Factor integration geometry. All parameter shown correspond to Equation 4.2.

Table 4.1: This table shows the results for different integration depths for the J-Factor. Results are given for two profiles (Einasto Cusped, NFW Cusped) and given in 1×10^{20} GeV^{2}kpc sr cm^{-6}. The change δ_J refers to the difference to the previous integration step.

Depth in 8.5 kpc	J_{Einasto}	δ_J in %	J_{NFW}	δ_J in %
1	0.122 455	-	0.070 858	-
2	0.243 905	99.2	0.140 999	99.0
3	0.243 933	1.1×10^{-6}	0.141 029	2.1×10^{-6}
4	0.243 936	1.2×10^{-7}	0.141 033	2.8×10^{-7}
5	0.243 937	4.1×10^{-8}	0.141 034	7.1×10^{-8}
6	0.243 937	$<1.0 \times 10^{-8}$	0.141 034	$<1.0 \times 10^{-8}$

method impossible. However, one can still use the OnOffBackground, where regions for background estimation are located in special Off runs. For the analysis presented no dedicated run pairs were taken with H.E.S.S. Therefore a procedure to find appropriate runs was developed. It was decided to use only runs with at least 10° distance to the Galactic Centre. For the NFW and Einasto profile this results in a J-Factor of about 10 % compared to the analysis region (see Fig 4.3) for runs with 10° distance. Due to the low Dark Matter density for distances larger than 10° the J-Factor in Off runs can be neglected. For the isothermal profile a larger distance to the Galactic Centre is needed in order to provide a reasonable change of the J-Factor between the On and Off region. However, this would reduce the amount of found run pairs. Therefore only the NFW and Einasto profile are studied. Now the J-Factor of the analysis regions (also "region of interest", RoI) can be calculated. The results are shown in Table 4.2.

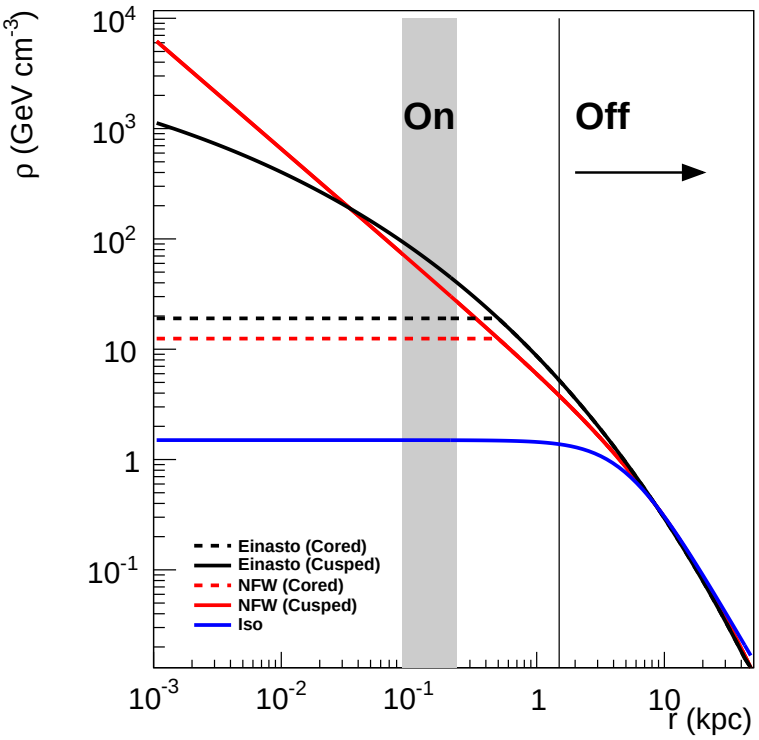

Figure 4.3: Dark Matter density profiles used in this work; NFW (red) and Einasto (black). As a reference the Isothermal profile is also shown (blue). All profiles are normalized to 0.39 GeV/cm^3 at 8.5 kpc according to the Dark Matter density in the solar system (Catena & Ullio, 2010). The gray area indicates the position of the On regions used. The area to the right of the vertical black line, corresponding to 10° offset to the galactic plane, shows potential Off regions.

Table 4.2: This table shows the different On regions with their parametrization and the resulting J-Factor in 1×10^{20} GeV^{2}kpc sr cm^{-6}. Only the inner ring radius is given. Each ring has a thickness of 0.°1. The area given is corrected for excluded regions.

RoI number	Ring Radius (deg)	area (sr)	J_{Einasto}		J_{NFW}	
			Cusped	Cored	Cusped	Cored
1	0.6	1.9039×10^{-5}	1.480	0.363	0.749	0.165
2	0.7	6.5980×10^{-5}	4.630	1.256	2.284	0.569
3	0.8	9.0928×10^{-5}	5.754	1.727	2.775	0.782
4	0.9	1.0473×10^{-4}	5.996	1.982	2.838	0.898
5	1.0	1.2014×10^{-4}	6.270	2.265	2.925	1.027
6	1.1	1.3653×10^{-4}	6.534	2.564	3.015	1.163
7	1.2	1.5310×10^{-4}	6.753	2.862	3.089	1.298
8	1.3	1.7174×10^{-4}	7.015	3.195	3.187	1.450
9	1.4	1.9200×10^{-4}	7.295	3.552	3.296	1.612

4.2 Analysis software and event selection

To be able to analyse data from H.E.S.S. I and H.E.S.S. II the software version HAP-15-12-pl02 was used. Some modifications were needed in order to perform the presented data analysis. For the H.E.S.S. I data the cut configuration std_ImPACT_4tel_fullEnclosure version 32 was used. This configuration takes advantage of the ImPACT event reconstruction (Parsons & Hinton, 2014) and performs the event selection using a boosted decision tree.
For H.E.S.S. II data the configuration std_ImPACT_hybrid_4tel_fullEnclosure version 35 was used. This configuration also takes advantage of the ImPACT event reconstruction and event selection using a BDT.
Cuts for both configurations used in this work are summarized in Table 4.3. Cuts on the image amplitude ensure that the analysed camera images are bright enough for a well determined parametrisation. A cut on the local distance removes images with a centre-of-gravity position close to the camera edge; this removes shower images that are only partly contained within the camera. The high multiplicity cut of 4 ensures that only events with information from four telescopes at least are reconstructed which improves the reconstruction quality. The separation of γ-like events and background-like events is carried out by a cut on ζ BDT.

Table 4.3: Analysis cut configurations used within this work and the cuts applied to data.

	H.E.S.S. I	H.E.S.S. II
Configuration name	std_ImPACT_4tel _fullEnclosure	std_ImPACT_hybrid_4tel _fullEnclosure
Configuration version	32	35
parameter	cut value	
Image amplitude CT1-CT4	$\geq$ 60 p.e.	$\geq$ 40 p.e.
Image amplitude CT5	-	$\geq$ 80 p.e.
Local distance	$\leq$ 0.525	$\leq$ 0.525
Multiplicity	$= 4$	≥ 4
ζ BDT	[0,0.83]	[0,0.75]

4.3 Data selection

It is important to carry out a so-called run selection to remove observations which were taken under bad conditions (weather and/or instrument). In Section 3.7 the standard run selection of H.E.S.S. was described. To ensure that the analysis results are as stable as possible. Additional, more restrictive selection criteria were used within this work. These will be described in the following.

In order to achive the best possible energy reconstruction, only events with four telescopes participating in the data taking were analysed. This means at least four telescopes have to work during observation. By restricting the data set to observations with low zenith angles the selected runs have a relatively low energy threshold. The mean zenith angle of a run was restricted to be below 40°. All runs fulfilling these requirements are considered.

Runs with their observation position within 5° around the Galactic Centre are considered as On-Runs. All runs with a distance of at least 10° to the galactic plane are considered as Off region candidates. This ensures that the J-Factors of the Off regions can be neglected, since they are in the order of 1 % of the J-Factor expected in the On region. Contamination from diffuse γ-ray emission along the galactic plane is excluded as well. The H.E.S.S. II data set was split into two samples, one with all five telescopes participating and one with four telescopes. In the latter, CT1 was missing due to a camera upgrade taking place in 2015 and 2016. The data set for H.E.S.S. I was taken between December 12, 2005 (run 30000) and January 2, 2013 (run 80000). The H.E.S.S. II data set was taken from May 21, 2014 (run 94951) to March 7, 2016 (run 116872). Table 4.4 shows the number of remaining runs after applying the standard selection criteria and the additional cuts on number of telescopes and zenith angle.

Table 4.4: List of runs passing through standard run selection criteria and the additional cut on zenith angle and number of telescopes.

	H.E.S.S. I		H.E.S.S. II 4tel		H.E.S.S. II 5tel	
	Runs	Livetime	Runs	Livetime	Runs	Livetime
On candidate	210	99.5 h	90	40.3 h	131	59.2 h
Off candidate	3147	1429.7 h	393	174.5 h	659	289.1 h

4.4 Run pairing

Due to the large size of the selected analysis region, no regions for background estimation can be found within the FoV of the Galactic Centre observations. It is therefore necessary to find observations (with large distance to the GC, Off run) with similar background conditions as the GC observations (On run). In order to fulfil this requirement a procedure was developed to pair runs from the GC region with Off run candidates. A model is developed to predict the rate of background events depending on several observables. With the help of this model a pairing function can be developed to find suitable Off runs for the On data set. A comparable approach was previously

employed by Glück (2011) for a Hillas-based analysis and Jahn (2013) for a Model++ analysis[1]. In both cases only H.E.S.S. I data were analysed.

4.4.1 Parameters of interest

In this section the parameters included in the pairing will be introduced. The selection of parameters was influenced by the results of the previous studies.

The rate of background events depends on the observation direction, atmosphere and telescope condition. For weather monitoring, a weather station is installed at the H.E.S.S. site, providing measurements of temperature and relative humidity at ground. Each telescope is equipped with a radiometer which measures the temperature of the upper atmosphere.

The state of the telescopes themselves will be characterized with the help of the muon efficiency and broken pixel fraction. Furthermore the observation direction in zenith and azimuth and the NSB rate is included in the study. The last parameter of this study is the event rate. This number describes the rate of events which are read out with at least four telescopes participating. For a study of events with high multiplicity of telescopes this number is superior to the trigger rate, due to the intrinsic inclusion of dead time. In Table 4.5 the trigger and read-out rates for different telescope multiplicities are shown, for a H.E.S.S. II run in which all five telescopes participated. As one can see for stereoscopic triggers with CT1-CT5 6.5 % are read out as CT5 mono events and 0.5 % of the events are dropped. For stereoscopic triggers with CT1-CT4 about 8 % of the events are dropped. In case of triggers with at least 4 telescopes 84.7 % are also read out in at least four telescopes. Due to the high rate of CT5 mono events only a small fraction of events is triggered with at least four telescopes (3.3 %). Events are read out only in not busy telescopes, resulting in a total fraction of events with four or five telescopes of 2.8 %. For a H.E.S.S. I run this number is 17.5 % and for a H.E.S.S. II run with four active telescopes it is 1.7 % (the full tables can be found in Appendix A).

Table 4.5: The different trigger pattern and readout pattern for all events within an observation run with all five telescopes active (Run 95324, mean zenith angle 14°). Multi 4+ corresponds to events with at least four telescopes participating.

Trigger type	Total triggers	CT5 mono read-outs	CT1-5 stereo read-outs	CT1-4 stereo read-outs	dropped	multi 4+ read-outs
CT5 mono	77.7%	95.9%	0.0%	0.0%	4.1%	0.0%
CT1-CT5 stereo	18.5%	6.5%	89.3%	3.6%	0.5%	14.3%
CT1-CT4 stereo	3.7%	0.0%	0.0%	91.7%	8.3%	5.1%
Sum	100%	75.7%	16.6%	4.1%	3.6%	2.8%
Multi 4+	3.3%	1.6%	87.4%	10.7%	0.3%	84.7%

Most of these parameters are measured or calculated continuously over the duration of a run. However, in the study only the averaged values will be taken into account. This averaging is done over the duration of the run and participating telescopes. The only exceptions are the muon

[1] In the Model++ analysis events are reconstructed by comparing the camera image with a prediction from a semi-analytical model (de Naurois & Rolland, 2009).

efficiency and NSB rate. Here, the averaging is only done for CT1 to CT4, and CT5 is treated separately. These two parameters are the only ones included in the study depending on the telescope type. In Table 4.6 all parameters included in the study are listed with their accepted parameter range and the subsystem they are determined from.

Table 4.6: Parameters that have an expected impact on the background rate and that are studied in this work. Also shown are the approximate value range and the origin.

Parameter	Range		Category
Event rate	0 Hz	to 200 Hz	DAQ
Zenith angle	0°	to 40°	Tracking
Azimuth angle	0°	to 360°	Tracking
Air Temperature	0 °C	to 30 °C	Weather station
Relative humidity	0 %	to 100 %	Weather station
Radiometer temperature	− 60 °C	to − 20 °C	Radiometer
Broken pixel fraction	0 %	to 10 %	Calibration
Muon efficiency	0 %	to 10 %	Calibration
NSB	0 MHz	to 300 MHz	Calibration

4.4.2 Background rate

As discussed in Section 3.11.3 the important characteristic of an On-Off run pair is that both runs have compatible observational conditions which should lead to similar count rates for diffuse background events. The background rate (BG rate) will be introduced in the following. Figure 4.4 shows an example of one observation and the corresponding FoV of this run. All events falling into the FoV (for H.E.S.S. II data 1.°5 radius, H.E.S.S. I data 2° radius) and not coming from known sources are summed. The area which is used for the calculation of the rate is the area of the FoV corrected for excluded regions and the time used is given by the difference between the first and the last event within a run. Since the radial dependence of the acceptance is not corrected for in this calculation of the BG rate, it is only a reasonable value to use for runs with small excluded regions. Therefore, all runs which exclude more than 25 % of the FoV were excluded from this study. The BG rate is written as:

$$\text{BG rate} = \frac{\#\text{events}}{\text{time} \times \text{area}} \tag{4.3}$$

The unit of the Background rate is $\text{deg}^{-2}\text{s}^{-1}$.

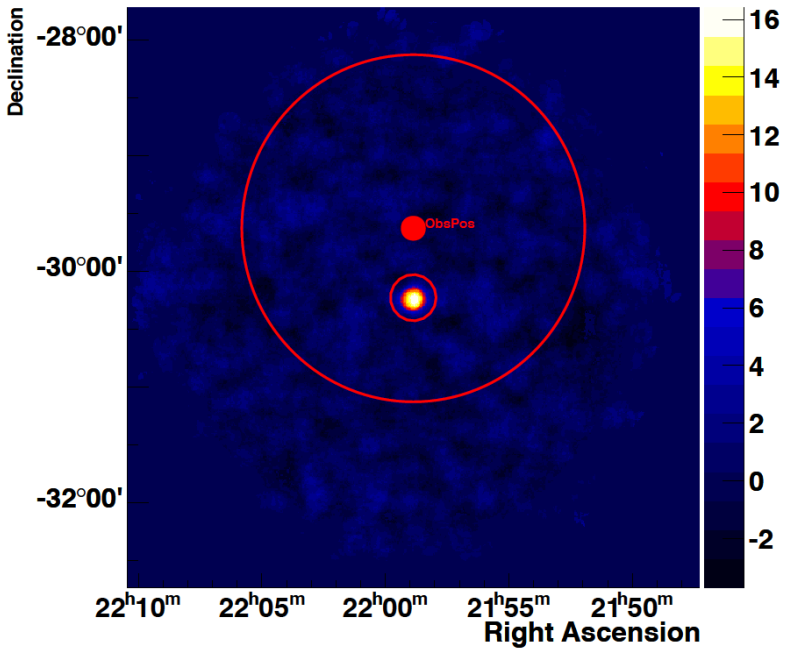

Figure 4.4: Skymap for PKS 2155–304. One exemplary pointing (red dot) is shown with the corresponding FoV (large red circle). The excluded region extension is indicated by a small red circle. All events falling into the FoV outside the excluded region are used for the BG rate calculation.

Correlation between different parameters

Before the dependency of the background rate can be studied, it is important to understand whether the parameters of interest are correlated or not. For this purpose, the correlation coefficient for each parameter pair was calculated. For the H.E.S.S. II data set with all telescopes the results

are summarized in Table 4.7. For the two other data sets the correlation coefficients are listed in Appendix B.

Most correlation coefficients for this data set are reasonably low, however the correlation between the NSB rate of CT1-CT4 and CT5 is very high with $\rho = 0.85$ ($\rho = 0.88$ for the H.E.S.S. II four telescope data set). This is expected, since all telescopes have the same stars within the FoV. The plot used to derive the correlation can be seen in Figure 4.5. Even though these two parameters are so strongly correlated, they were not merged due to the fact that the NSB rate of CT5 is on average higher than the mean rate in the small telescopes. Furthermore the correlation between the air temperature and radiometer temperature is high ($\rho \sim 0.6$). Also the correlation of the event rate and the mean muon efficiency in CT1-CT4 is high. This can be understood considering that a high muon efficiency indicates that the telescopes are more sensitive and therefore able to see more showers.

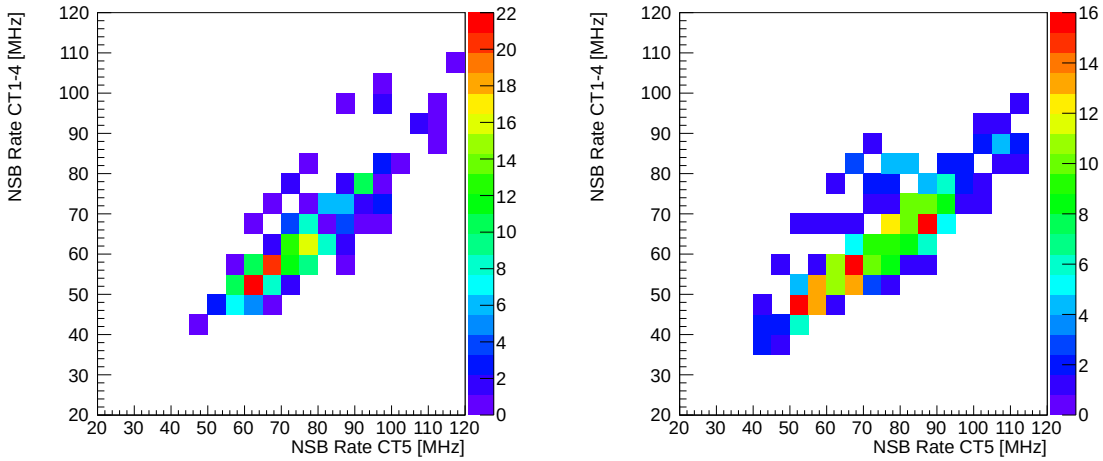

Figure 4.5: NSB rate for different telescope types (H.E.S.S. II data). On the abscissa the rate for CT5 is given, on the ordinate the mean rate of CT1-CT4 is drawn, both values are from the same run. The left plot shows the data for runs with four telescopes. The right plot shows data for runs with five telescopes. The colour scale indicates the frequency.

Table 4.7: Correlation coefficients for the H.E.S.S. II data set with five telescopes active. For the parameter 3 to 6 the mean value over all telescopes is used. For parameter 9 and 11 the mean value for the four small telescopes is used.

	Air Temperature	Relative humidity	Zenith angle	Azimuth angle	Radiometer Temperature	Broken pixel fraction	event rate	NSB rate CT5	NSB rate CT1-CT4	Muon efficiency CT5	Muon efficiency CT1-CT4
(1) Air Temperature	1	−0.36	0.24	−0.06	0.64	0.10	−0.08	0.43	0.53	−0.16	0.12
(2) Relative humidity		1	0.08	0.09	0.10	−0.09	0.18	0.08	−0.15	0.33	0.13
(3) Zenith angle			1	−0.31	0.39	−0.01	0.22	0.33	0.32	0.10	0.17
(4) Azimuth angle				1	−0.12	0.01	0.08	−0.02	−0.06	−0.07	0.06
(5) Radiometer Temperature					1	0.10	−0.08	0.43	0.33	−0.06	0.17
(6) Broken pixel fraction						1	0.08	0.09	0.12	−0.08	0.06
(7) event rate							1	0.41	0.42	0.44	0.61
(8) NSB rate CT5								1	0.85	0.40	0.29
(9) NSB rate CT1-CT4									1	0.20	0.52
(10) Muon efficiency CT5										1	0.22
(11) Muon efficiency CT1-CT4											1

4.5 Background rate dependency study

To determine the dependency of the background rate on the different parameters, the correlation of the rate with the parameters of interest is studied. Table 4.8 shows the correlation parameters of all three data sets. As one can see, the correlation varies from values close to 0 to up to $\rho \sim 0.8$. However it is unclear whether the background rate only depends on the high correlation values or the correlation is hidden for some parameters. In order to test this a function depending on the zenith angle and event rate is fitted to the BG rate. Afterwards one can calculate the expected BG rate from the function and draw $\frac{\text{BG rate}_{\text{measured}}}{\text{BG rate}_{\text{expected}}}$. This corrects the influence of the zenith angle and event rate revealing the dependence of the remaining parameters.

Table 4.8: This table lists all studied parameters and the correlation coefficients with the Background rate. Correlation coefficients for all three data sets are listed.

	H.E.S.S. I	H.E.S.S. II 4tel	H.E.S.S. II 5tel
event rate	0.81	0.65	0.43
Zenith angle	0.50	−0.04	−0.61
Air Temperature	−0.20	−0.16	−0.33
Relative humidity	0.10	−0.04	0.12
Azimuth angle	0.07	0.10	0.27
Radiometer Temperature	−0.12	−0.43	−0.41
Broken pixel fraction	−0.20	0.15	0.02
NSB rate CT5	-	−0.30	−0.07
NSB rate CT1-CT4	0.07	−0.17	−0.07
Muon efficiency CT5	-	0.10	0.26
Muon efficiency CT1-CT4	0.37	0.42	0.18

For the H.E.S.S. II set with five telescopes the dependency of the BG rate on the zenith angle and event rate shows the existence of two regimes (see Fig. 4.6). They are indicated with ellipses. It is unclear why the data set shows different behaviour above and below 15° zenith, however for the study of the rate it is important to take the effect into account. In order to do so, the data set is separated at 15° zenith. In order to model the dependence of the BG rate on the zenith angle and event rate the data set is fitted with:

$$BG_{\text{exp}}(\text{Zenith}, \text{event Rate}) = \begin{cases} a_1 + b_1 \times \text{event Rate} + c_1 \times \text{Zenith} & \text{if Zenith} \leq 15^\circ \\ a_2 + b_2 \times \text{event Rate} + c_2 \times \text{Zenith} & \text{if Zenith} > 15^\circ \end{cases} \tag{4.4}$$

The parameters were determined as $a_1 = -4.569 \times 10^{-2}\,\text{deg}^{-2}\text{s}^{-1}$, $b_1 = 2.896 \times 10^{-3}\,\text{deg}^{-2}$, $c_1 = -5.895 \times 10^{-4}\,\text{deg}^{-3}\text{s}^{-1}$, $a_2 = -1.375 \times 10^{-2}\,\text{deg}^{-2}\text{s}^{-1}$, $b_2 = 1.591 \times 10^{-3}\,\text{deg}^{-2}$ and $c_2 = -3.839 \times 10^{-4}\,\text{deg}^{-3}\text{s}^{-1}$.

To test the quality of the model the quantity $\frac{\text{BG rate}_{\text{measured}}}{\text{BG rate}_{\text{expected}}}$ is shown as a function of the event rate and zenith angle in Figure 4.7. As one can see in both cases the straight line fit results in a small slope and an offset close to 1.

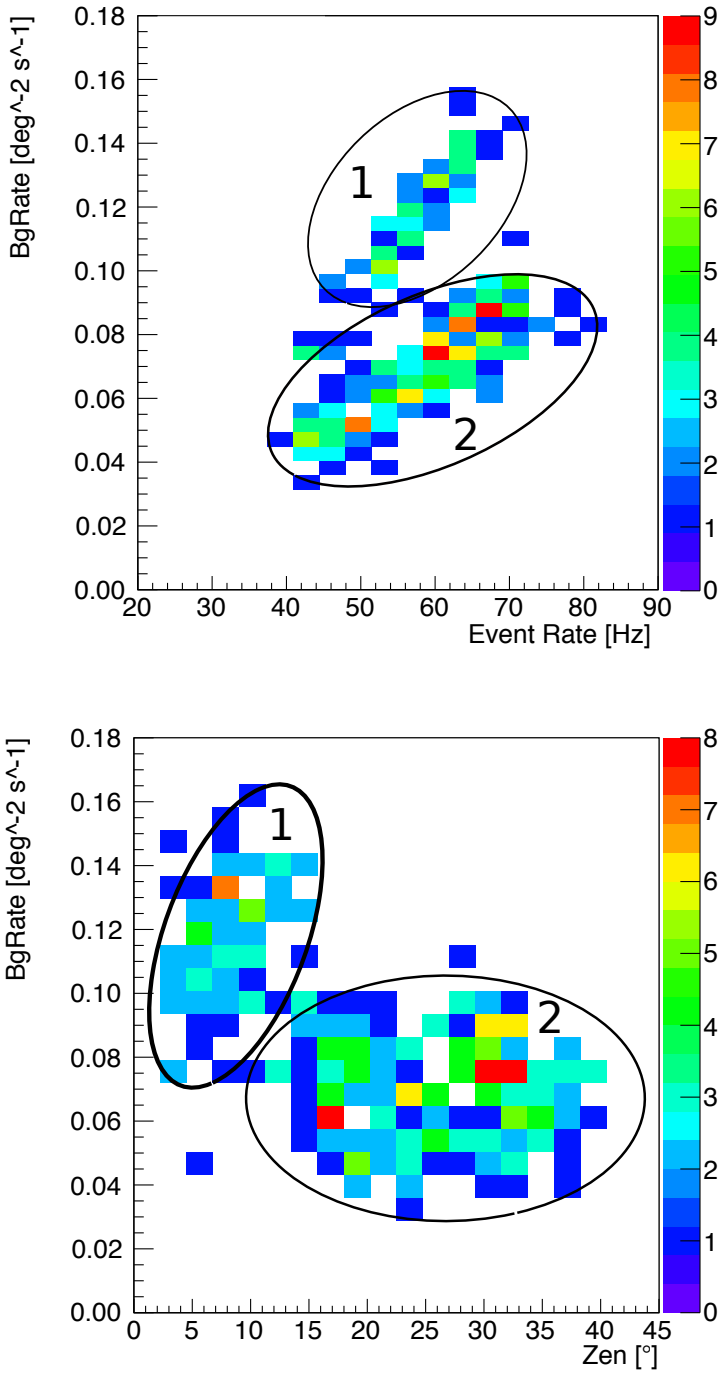

Figure 4.6: Top: This figure shows the BG rate and the event rate for the H.E.S.S. II five telescope data set. Two populations of runs are visible. Bottom: The BG rate depending on the zenith angle is shown.

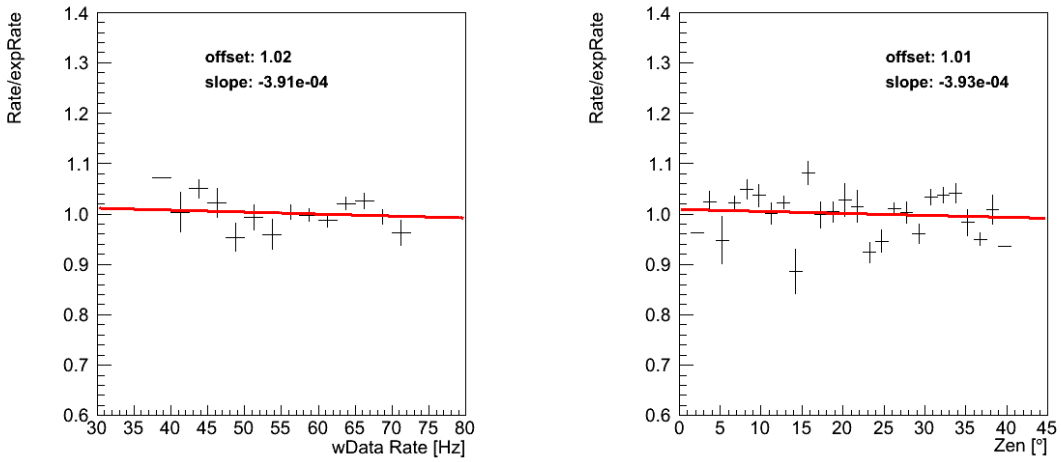

Figure 4.7: Left: $\frac{\text{BG rate}_{\text{measured}}}{\text{BG rate}_{\text{expected}}}$ depending on event rate of CT1-CT5 in H.E.S.S. II five telescope data. Right: $\frac{\text{BG rate}_{\text{measured}}}{\text{BG rate}_{\text{expected}}}$ depending on the zenith angle in H.E.S.S. II five telescope data.

To determine the dependency of the remaining parameters, a straight line is fitted to the $\frac{\text{BG rate}_{\text{measured}}}{\text{BG rate}_{\text{expected}}}$ as a function of the parameter. The resulting plots can be seen in Appendix C.3. One exemplary dependency of the radiometer temperature can be seen in Figure 4.8. The slope of the line fit will be used as a weighting for the run pairing process.

In order to describe the H.E.S.S. II data set with four telescopes, the function g (Eq. 4.5) was used:

$$g(\text{Zenith}, \text{event rate}) = \begin{cases} a_1 + b_1 \times \text{event rate} + c_1 \times \text{Zenith} + d_1 \times (\text{event rate})^2 & \text{if Zenith} \leq 12° \\ a_2 + b_2 \times \text{event rate} + c_2 \times \text{Zenith} + d_2 \times (\text{event rate})^2 & \text{if Zenith} > 12° \end{cases} \tag{4.5}$$

The parameters were determined to $a_1 = -8.125 \times 10^{-2}\,\text{deg}^{-2}\text{s}^{-1}$, $b_1 = 5.375 \times 10^{-3}\,\text{deg}^{-2}$, $c_1 = -7.107 \times 10^{-4}\,\text{deg}^{-3}\text{s}^{-1}$, $d_1 = -3.954 \times 10^{-5}\,\text{deg}^{-2}\text{s}^{1}$, $a_2 = -2.428 \times 10^{-2}\,\text{deg}^{-2}\text{s}^{-1}$, $b_2 = 1.310 \times 10^{-3}\,\text{deg}^{-2}$, $c_2 = -1.892 \times 10^{-4}\,\text{deg}^{-3}\text{s}^{-1}$ and $d_2 = 1.060 \times 10^{-5}\,\text{deg}^{-2}\text{s}^{1}$.

The dependency plots derived with this model function can be seen in Appendix C.2. Overall the model description is worse than in the case of the 5 telescope data set. This is probably caused by the fact that this data set contains two different run types: one where all five telescopes were turned on during the observation and one telescope was later discarded due to not passing quality selection and the other one where only four telescopes were participating in the observation. This leads to a difference in the trigger pattern and read-out pattern. Data from the first case seem to have a larger dead time due to a telescope being removed from the data post-data taking.

For the H.E.S.S. I data set the function given in Equation 4.4 was used again. However the definition range for the two ranges is from 0° to 35° and 35° to 40°. The separation into different regimes is less prominent than in the H.E.S.S. II data set (see Fig 4.9). However, splitting the sample improved the model description. The parameters were determined as $a_1 = -1.579 \times 10^{-2}\,\text{deg}^{-2}\text{s}^{-1}$,

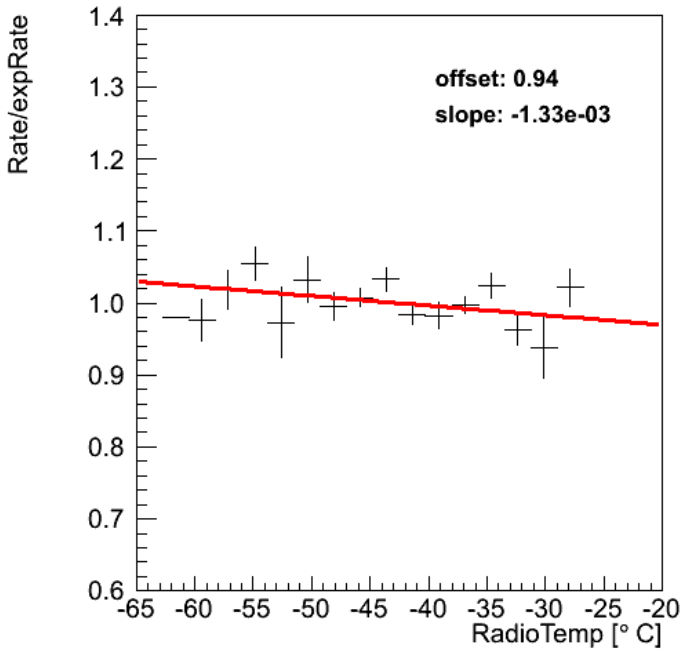

Figure 4.8: This figure shows the $\frac{\text{BG rate}_{\text{measured}}}{\text{BG rate}_{\text{expected}}}$ dependency of the mean radiometer temperature, for the H.E.S.S. II five telescope data set.

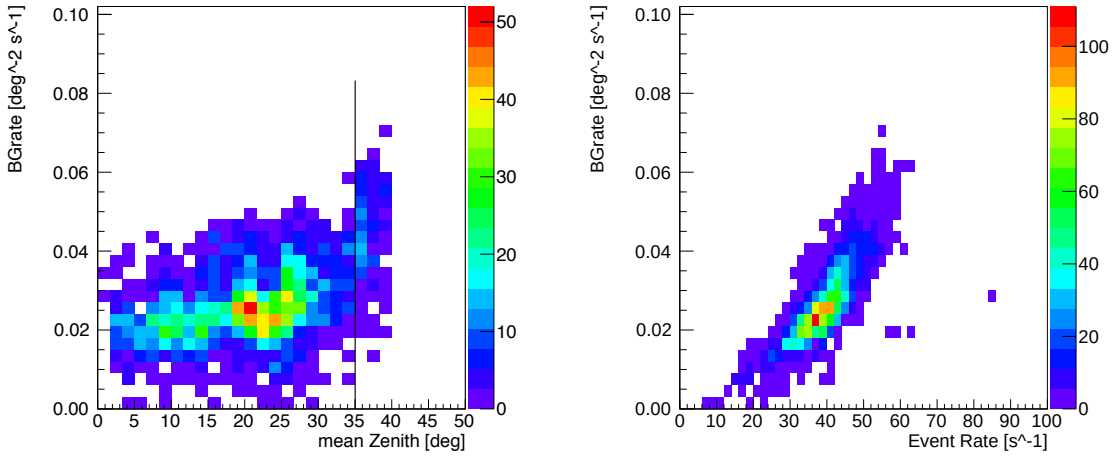

Figure 4.9: Left: This figure shows the BG rate and the zenith angle for the H.E.S.S. I data set. The value were the data set is separated is indicated by a line. Right: The BG rate depending on the event rate is shown.

$b_1 = 1.051 \times 10^{-3}\,\mathrm{deg}^{-2}$, $c_1 = 1.932 \times 10^{-5}\,\mathrm{deg}^{-3}\mathrm{s}^{-1}$, $a_2 = -4.083 \times 10^{-3}\,\mathrm{deg}^{-2}\mathrm{s}^{-1}$, $b_2 = 1.171 \times 10^{-3}\,\mathrm{deg}^{-2}$ and $c_2 = -1.501 \times 10^{-4}\,\mathrm{deg}^{-3}\mathrm{s}^{-1}$.

4.5.1 Run pairing function

In order to pair runs from the On and Off data set one has to develop a function to describe how well two runs match. As mentioned we are interested in run pairs with similar BG rates. With this in mind we can construct a function comparable to a χ^2-test:

$$S = \sum_P w^2 \times (p_{\mathrm{On}} - p_{\mathrm{Off}})^2. \tag{4.6}$$

The sum is over all parameters of interest (P) with p_{On} the corresponding value of an On run (p_{Off} for Off candidates) and S the score. In order to account for different impact of parameters and different values a weighting w is introduced. This weighting is calculated from the slope of line fits to the $\frac{\text{BG rate}_{\text{measured}}}{\text{BG rate}_{\text{expected}}}$ distributions, and rescaled so that the weighting of the zenith angle is 1. The weightings w can be found in Table 4.9. The large difference in weightings come from the different parameter ranges (the zenith angle is in the range 0° to 40° while the Muon efficiency is <0.1).

Table 4.9: Weighting parameters used for the run pairing. Parameters are scaled so that the weighting for the zenith angle is 1. The unit of the weighting parameters is given in the second column.

	Unit	H.E.S.S. I	H.E.S.S. II 4tel	H.E.S.S. II 5tel
Zenith angle	deg^{-1}	1	1	1
Air Temperature	$^\circ\mathrm{C}^{-1}$	1.5	0.17	6.4
Relative humidity	-	7	0.92	1.7
Azimuth angle	deg^{-1}	0.14	0.22	9.1×10^{-2}
Radiometer Temperature	$^\circ\mathrm{C}^{-1}$	3	5.65	3.4
Broken pixel fraction	-	9.5×10^3	1×10^3	2.4×10^3
event rate	s	7	0.71	1
NSB rate CT5	MHz^{-1}	-	1.71	3.6
NSB rate CT1-CT4	MHz^{-1}	7	1.37	4
Muon efficiency CT5	-	-	1.51×10^3	6.0×10^3
Muon efficiency CT1-CT4	-	6.9×10^3	4.3×10^3	1.4×10^4

For each pair of On run and Off-run candidate the score S is calculated and the Off candidates ordered according to score. Small values of S indicate a good agreement of the parameters of interest. For the pairing only scores below a threshold (80 for H.E.S.S. I and 200 for H.E.S.S. II data) are used. This is done to ensure that only runs pairs with sufficient agreement in the studied parameters are used. Furthermore run pairs with a separation of more than 3° in zenith angle are discarded. This ensures that the energy threshold does not change significantly between the On and Off run. Now all On runs with only one matching Off candidate are grouped into a pair until only On runs with several matched Off candidates remain. For On runs with several matching Off runs the match with the lowest score is selected. After every assignment of a pair it will be

checked if an On run which had multiple matches has only one remaining match. This procedure maximises the amount of pairs found and at the same time minimizes the overall scores. Off runs are only used once to prevent correlated background.

4.6 Coordinate transformation for Off events to On run coordinates

In order to be able to analyse the Off data, one has to transform the coordinates of every Off event to corresponding coordinates within the FoV of the On run. The coordinate transformation used in this work is given by:

$$\begin{pmatrix} x \\ y \\ z \end{pmatrix}_{\text{new}} = \begin{pmatrix} \cos(\lambda_{\text{On}}) & \sin(\lambda_{\text{On}}) & 0 \\ -\sin(\lambda_{\text{On}}) & \cos(\lambda_{\text{On}}) & 0 \\ 0 & 0 & 1 \end{pmatrix} \begin{pmatrix} \cos(-\beta_{\text{On}}) & 0 & -\sin(-\beta_{\text{On}}) \\ 0 & 1 & 0 \\ \sin(-\beta_{\text{On}}) & 0 & \cos(-\beta_{\text{On}}) \end{pmatrix} \begin{pmatrix} \cos(\beta_{\text{Off}}) & 0 & -\sin(\beta_{\text{Off}}) \\ 0 & 1 & 0 \\ \sin(\beta_{\text{Off}}) & 0 & \cos(\beta_{\text{Off}}) \end{pmatrix} \begin{pmatrix} \cos(-\lambda_{\text{Off}}) & \sin(-\lambda_{\text{Off}}) & 0 \\ -\sin(-\lambda_{\text{Off}}) & \cos(-\lambda_{\text{Off}}) & 0 \\ 0 & 0 & 1 \end{pmatrix} \begin{pmatrix} x \\ y \\ z \end{pmatrix}_{\text{old}} \tag{4.7}$$

with x, y, z the direction of an event from the Off run and λ_{On} the Right ascension of the observation direction from the On run and β_{On} the Declination. λ_{Off} and β_{Off} are the respective coordinates of the observation direction of the Off run. The used transformation will not lead to field rotation or distortion of the FoV from the Off run. The disadvantage of this method is that the non-uniform camera properties (e.g. zenith angle dependence across the FoV) are not reproduced correctly. However, due to the pairing of runs with similar zenith angle, this effect is rather small.

4.7 Performance of the On-Off Analysis

In order to verify that the run pairing is working as intended, a test field was analysed. The chosen source for this test is PKS 2155–304. It is a reasonable choice due to a large number of available observations and a similar distribution in zenith angle as for the Galactic Centre. In H.E.S.S. II data, 26 run pairs were found with 7 taken with 5 telescopes. In H.E.S.S. I 60 pairs were found. The two important aspects of the performance test are:

- How well is the background normalised in the FoV?
- How well is the spectrum reconstructed using the On-Off technique?

In order to answer the first question excluded significance maps are produced, using the On-Off analysis, and compared to results from the standard method (RingBackground). The second question will be investigated by comparing the source spectrum with the result of a standard analysis (ReflectedBackground).

4.7.1 Low level checks

Before the high level analysis results like sky maps and spectra are produced a series of low level checks were performed to test whether or not the run pairing works as intended. As already mentioned the goal is to find run pairs with similar background contamination and similar energy threshold since these are the most important characteristics in order to reconstruct a spectrum. In Figure 4.10 the background rates of the found pairs are shown. As one can see for both H.E.S.S. I and H.E.S.S. II the agreement in the rates is very good. In order to take differences in the energy

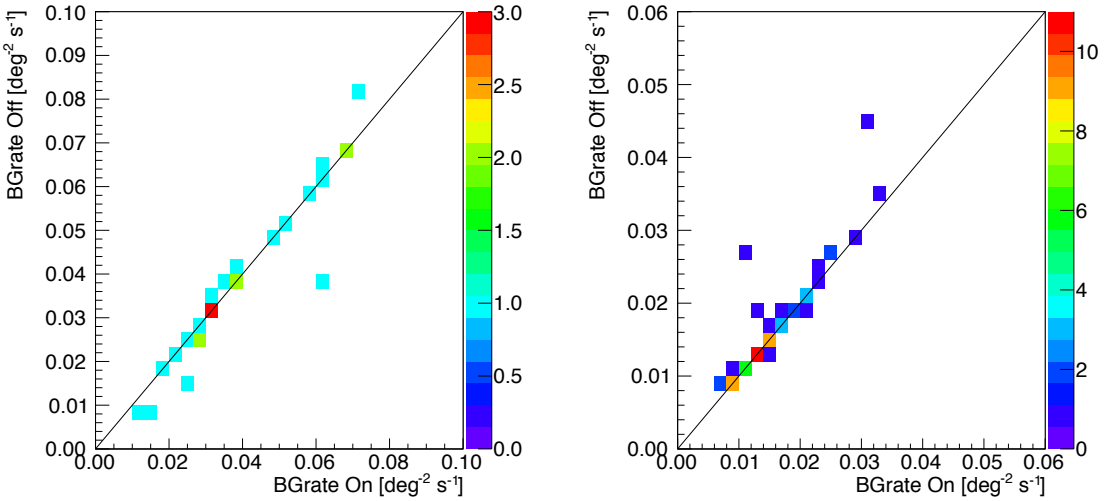

Figure 4.10: BG rate for PKS 2155–304 On-Off pairs. The abscissa shows the BG rate from On runs and the ordinate from Off runs. A straight line with BG rate (On) = BG rate (Off) was drawn to guide the eye. Left: H.E.S.S. II data set, combining four and five telescope runs. Right: H.E.S.S. I data set.

threshold into account, the maximum value of the threshold from an On-Off run pair is used within the analysis. Figure 4.11 shows the energy threshold of the found run pairs. For the H.E.S.S. II data set the agreement is very good. For the H.E.S.S. I data set the difference in the energy threshold within run pairs is slightly higher resulting in a higher loss of statistics.

4.7.2 Skymap

The quality of significance maps can be quantified by the so-called entry distribution where all pixel entries of a map are written into a histogram counting the frequency of significance values. If this is done for a source-free region, within each pixel of the map the background is Poisson distributed. If no systematic effects occur, the entry distribution has a Gaussian shape with mean 0 and width 1. However, such an entry distribution is not able to resolve gradients or clusters of excess or deficit within a map. Therefore the actual map has to be examined as well.

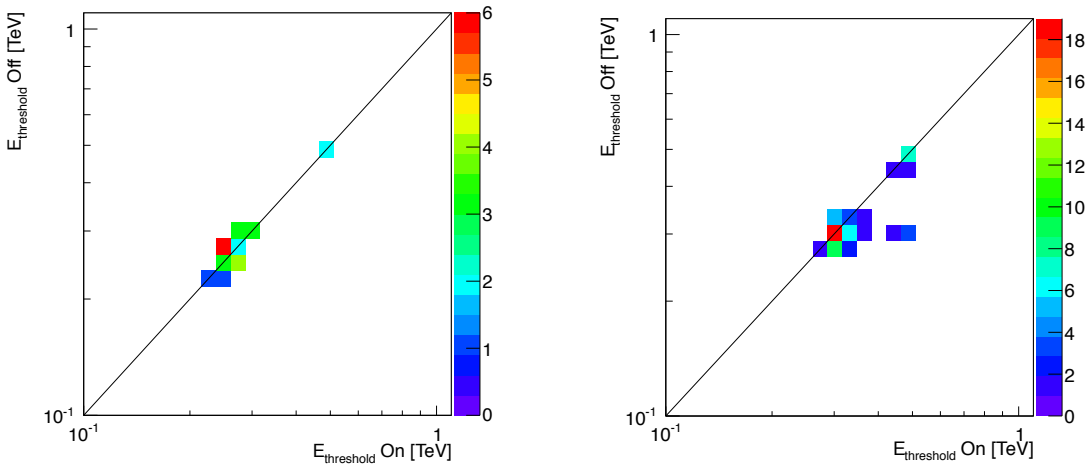

Figure 4.11: Energy threshold for PKS 2155–304 On-Off pairs. The abscissa shows the energy threshold from On runs and the ordinate from Off runs. A straight line with Energy threshold (On) = Energy threshold (Off) was drawn to guide the eye. Left: H.E.S.S. II data set, combining four and five telescope runs. Right: H.E.S.S. I data set.

H.E.S.S. II

Figure 4.12 shows the significance map of the PKS 2155–304 FoV using the 26 On runs from the found pairs of the H.E.S.S. II data set. In this case the RingBackground method was used. As one can see, the source is detected with about $16\,\sigma$. Due to the highly significant detection fluctuations of the background are barely visible. Therefore in the following, maps with the source excluded are shown. Figure 4.13 (left) shows the same FoV as Figure 4.12 with the source excluded, now revealing fluctuations in the background. The map has no cluster of positive or negative significances and does not show any unusual characteristics. The entry distribution (Fig. 4.13, right) is also featureless and a Gaussian fitted to the data is close to the expectation with a width of 0.98 and a mean of -0.03. Overall this map produced with the standard tools is of good quality.

Using the On data and Off data from the runs found with the run pairing described above, we get the map shown in Figure 4.14. This map shows a gradient along the Right Ascension axis. The width of the entry distribution increased to 1.08 and the mean is almost unchanged with -0.04. By looking at a slice along the RA axis with a width of 1° centred around the source (white borders in Fig 4.14), we can understand where this gradient comes from. Figure 4.15 shows the slice through the On map and the On exposure maps for both the RingBackground and OnOffBackground method. The slight difference in the normalization of the exposures comes from a difference in the normalization calculation between the different methods. Both models describe the data well. The two bins with high deviation of the exposure model at a distance of zero from the expected source position correspond to γ rays from PKS 2155–304. There are two more bins visible with large deviation to the expectation curves, one left of the source corresponding to the island of positive significance at $22^{\mathrm{h}}2^{\mathrm{m}}$ and $-30°30'$ and the other one on the right corresponding to the island at $21^{\mathrm{h}}55^{\mathrm{m}}$ and $-30°15'$ For the Off map and Off exposure maps the slice can be seen in Figure 4.16. The data points from the RingBackground method (black) are well described by

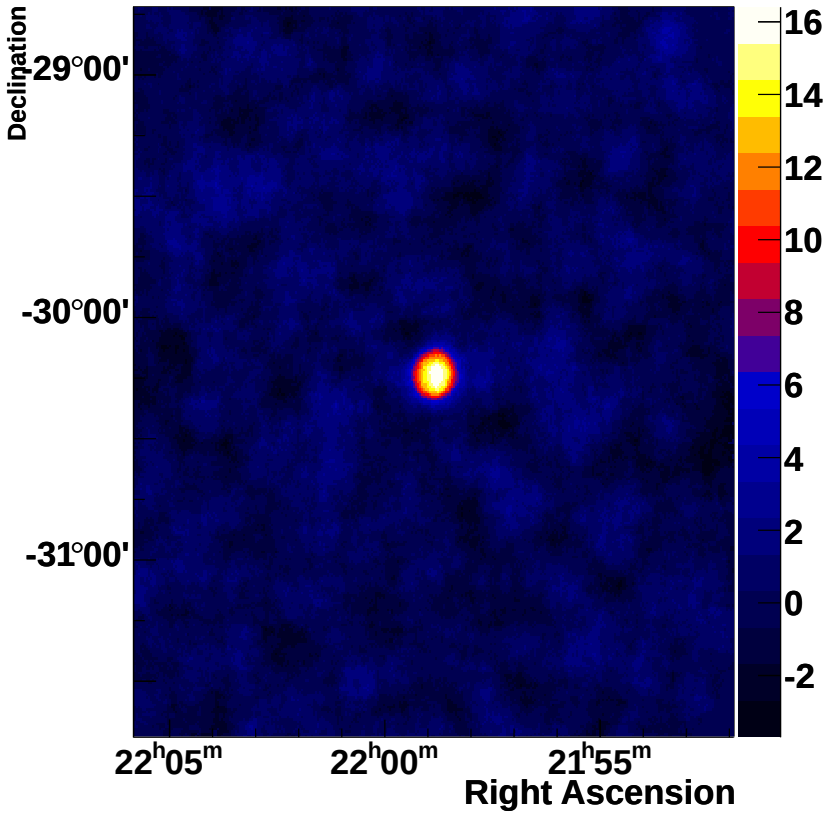

Figure 4.12: Significance map of PKS 2155–304 produced with the RingBackground method.

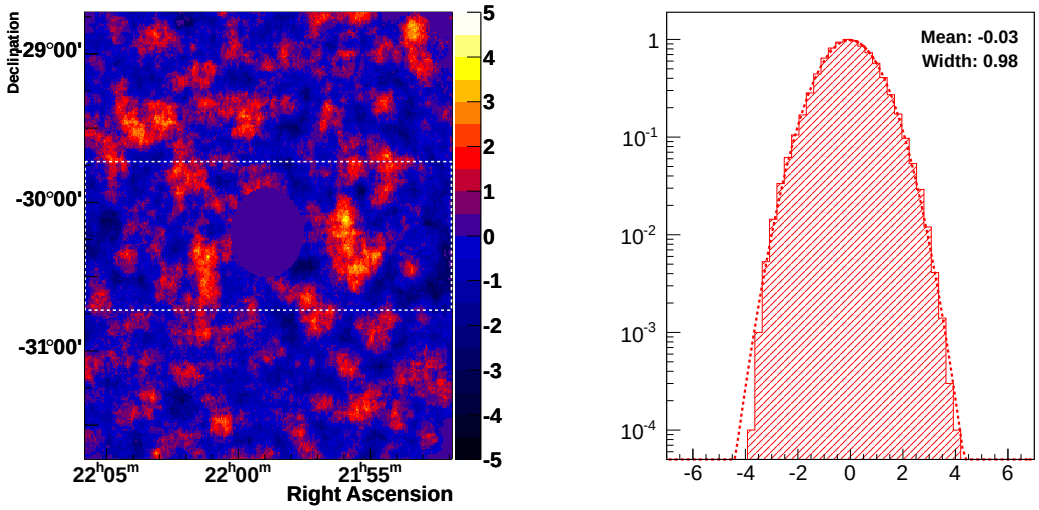

Figure 4.13: Left: Excluded significance map of the PKS 2155–304 field of view in RA-Dec coordinates. The data used is the H.E.S.S. II data set and the map was produced by using the RingBackground method. Right: Entry distribution of the map shown on the left. The dashed line is a Gaussian fitted to the distribution.

the exposure model (black line). However, the OnOffBackground data show a large deviation from the model. Especially at negative distance values the exposure overestimates the data. This leads to the observed gradient within the significance map.

When analysing the runs with all five telescopes and runs with one of the small telescopes missing (four telescope data set) separately, one can see a different behaviour. Figure 4.17 on the left side (the excluded significance map for the four telescope data set) clearly showing a gradient across the FoV. On the right side (five telescope data set) no gradient is visible. This can be understood due to the fact that the γ-ray acceptance for an asymmetric array is not radially symmetric; however, this is assumed in the HAP analysis. If the telescope missing is different from run to run the effect gets averaged out and the resulting map appears flat. In the case of the analysed data in 17 out of the 19 four-telescope runs CT1 was missing resulting in the observed gradient. This is also visible in the slice shown in Figure 4.18, where the data from five telescope runs (red) is well described by the exposure model. But the data from four telescope runs shows that the exposure is overestimating the data at negative distances from the source position. As a consequence for the Galactic Centre analysis one has to take care that in the case of four telescope runs no array configuration is dominant in the run pairing.

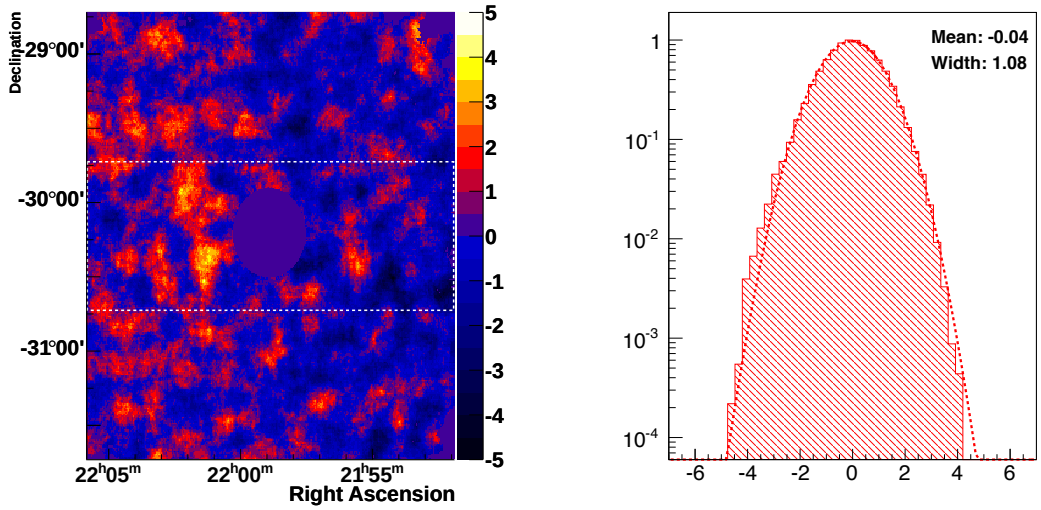

Figure 4.14: Left: Excluded significance map of the PKS 2155–304 field of view in RA-Dec coordinates. The data used is the H.E.S.S. II data set and the map was produced by using the OnOffBackground method. Right: Entry distribution of the map shown on the left. The dashed line is a Gauss fitted to the distribution.

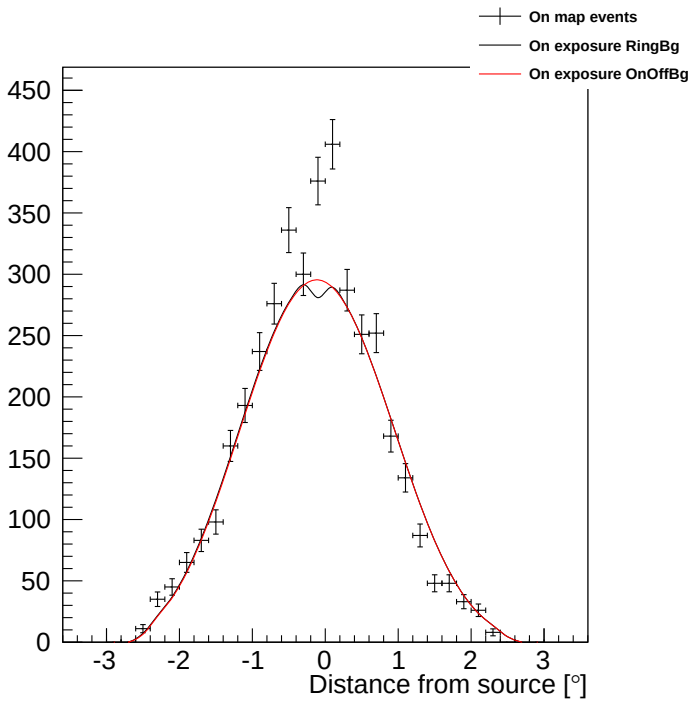

Figure 4.15: Slice along the RA axis of the On map (data points, see Fig 4.14) and the On exposure maps (solid line) for both the RingBackground (black) and OnOffBackground (red) method. All data shown here are from the H.E.S.S. II data set, including four and five telescope runs.

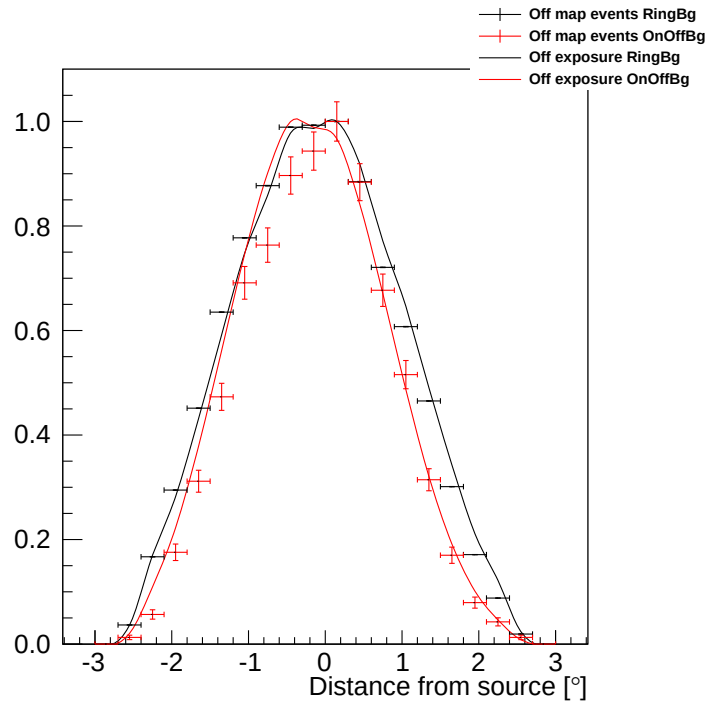

Figure 4.16: Slice along the RA axis of the Off map (data points) and the Off exposure maps (solid line) for both the RingBackground (black) and OnOffBackground (red) method. The maximum of the models was rescaled to 1 for better visualisation (the data were scaled accordingly). All data shown here are from the H.E.S.S. II data set, including four and five telescope runs.

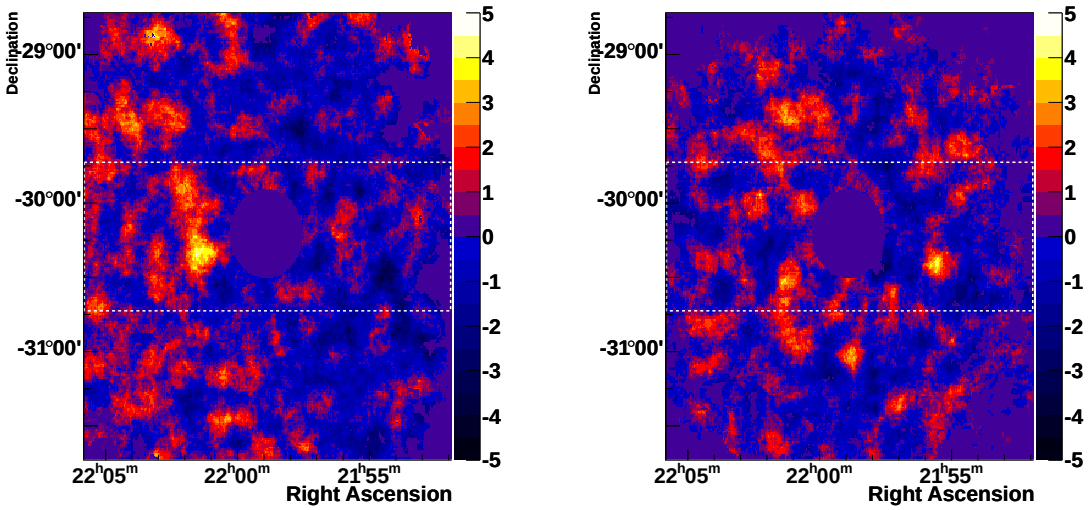

Figure 4.17: Excluded significance map of the PKS 2155–304 field of view in RA-Dec coordinates. The data used is the H.E.S.S. II data set and the map was produced by using the OnOffBackground method. Left: Runs with four telescopes only. Right: Runs with all five telescopes.

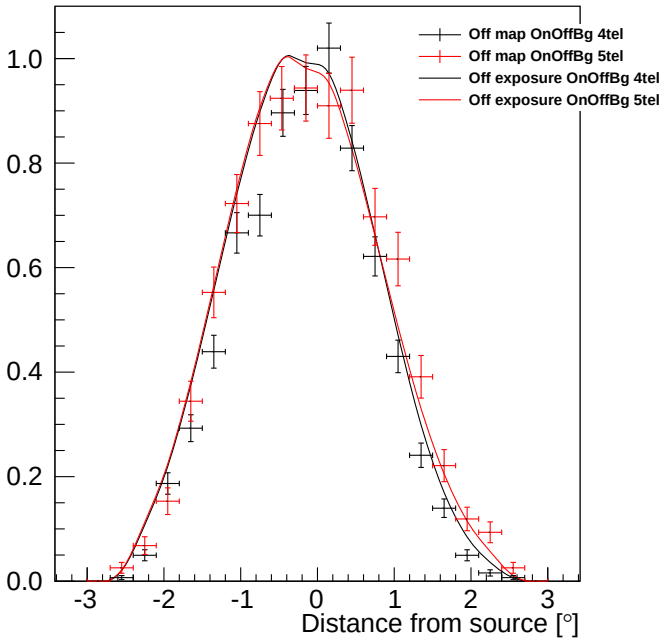

Figure 4.18: Slice through the off maps corresponding to the maps shown in Figure 4.17. In red shown the data for the five telescope runs and in black for the four telescope data set. Solid lines show the exposure prediction and points the measured number of counts.

H.E.S.S. I

All H.E.S.S. I tests were carried out in the same way as the H.E.S.S. II case. Figure 4.19 (left) shows an excluded significance map for the PKS 2155–304 FoV using the RingBackground method. The map shows no unusual features and the entry distribution (Fig. 4.19, right) is overall in good agreement with the expectation of Poisson-fluctuated background. The mean of −0.05 indicates only a slight overestimation of the background.

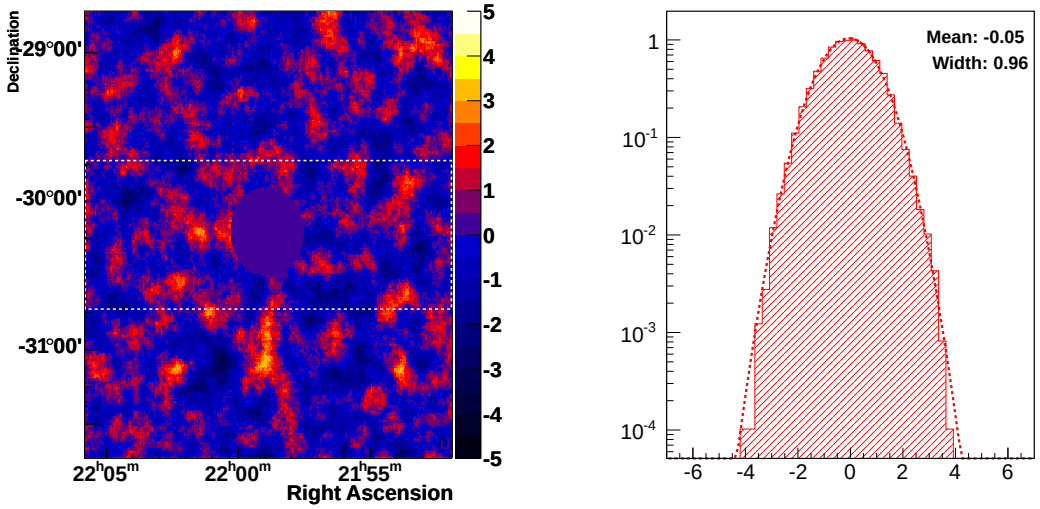

Figure 4.19: Left: Excluded significance map of the PKS 2155–304 field of view in RA-Dec coordinates. The data used is the H.E.S.S. I data set and the map was produced by using the RingBackground method. Right: Entry distribution of the map shown on the left. The dashed line is a Gaussian fitted to the distribution.

The significance map using the On-Off technique (Fig. 4.20, left) does not show any unusual features and is compatible with the result obtained using only five telescopes in the H.E.S.S. II data set. The entry distribution (Fig. 4.20, right) of the excluded significance map shown in Figure 4.20 is in good agreement with the expectation.

The slice through the On map and On exposure maps can be seen in Figure 4.21. Again the exposure curves describe the data points well. Only two points, where the counts of the source fall in, are significantly above the curve which is expected. The Off data from the RingBackground (Fig. 4.22, black points) are well described by the exposure curve (black line). The Off data from the OnOffBackground (red points) show some deviation from the exposure curve, especially close to the source position. However this deviation is still in good agreement with statistical fluctuations.

In the cases of H.E.S.S. I the On-Off analysis gives results of comparable quality to the standard RingBackground method, leading to the conclusion that the developed run pairing is able to find runs with good agreement in background level.
For H.E.S.S. II data with five telescopes also a good agreement was found, however, for data with only four telescopes it is important to have a mix of array configurations, otherwise a gradient is observed. For the Galactic Centre analysis this has to be kept in mind.

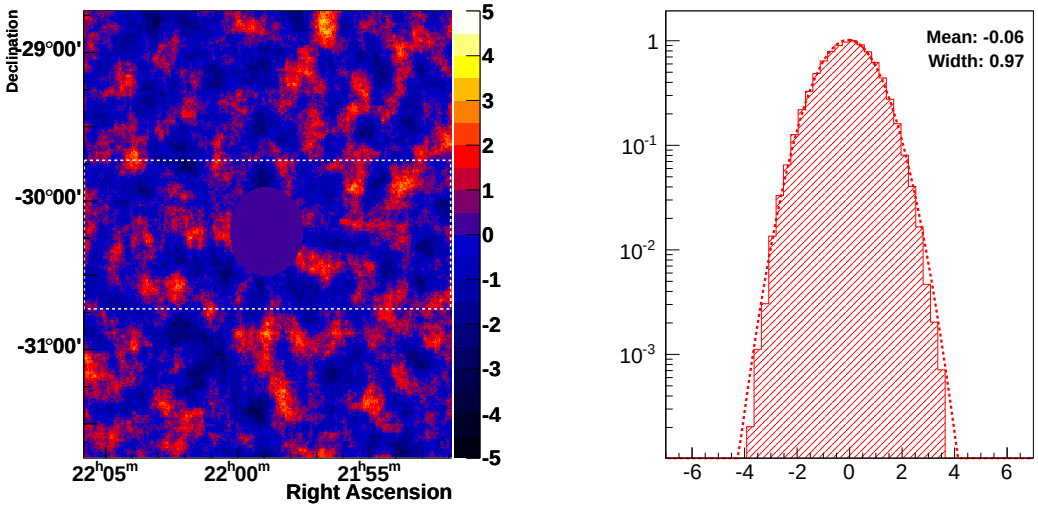

Figure 4.20: Left: Excluded significance map of the PKS 2155–304 field of view in RA-Dec coordinates. The data used is the H.E.S.S. I data set and the map was produced by using the OnOffBackground method. Right: Entry distribution of the map shown on the left. The dashed line is a Gauss fitted to the distribution.

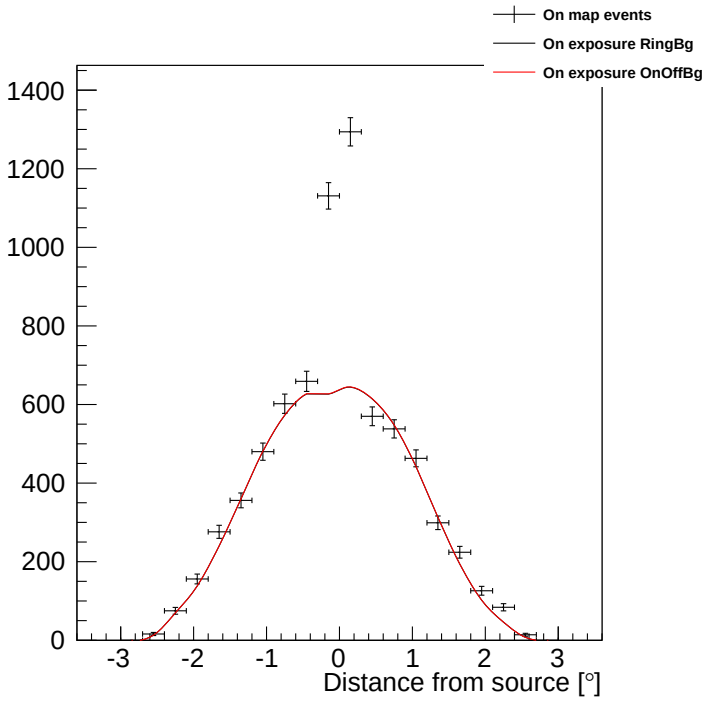

Figure 4.21: Slice along the RA axis of the On map (data points) and the On exposure maps (solid line) for both the RingBackground (black) and OnOffBackground (red) method. All data shown here are from the H.E.S.S. I data set.

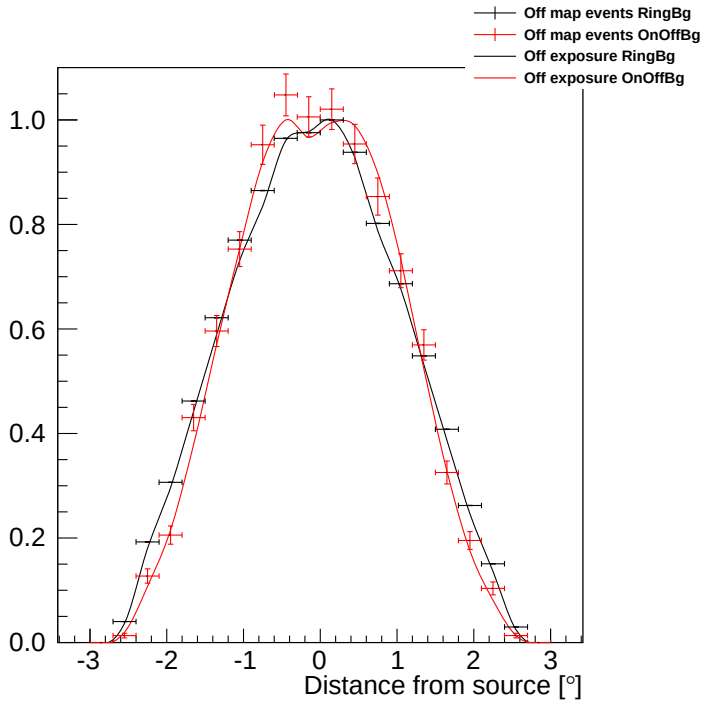

Figure 4.22: Slice along the RA axis of the Off map (data points) and the Off exposure maps (solid line) for both the RingBackground (black) and OnOffBackground (red) method. The maximum of the models was rescaled to 1 for better visualisation (the data were scaled accordingly). All data shown here are from the H.E.S.S. I data set.

4.7.3 Spectrum reconstruction

The standard spectrum fitting tool included in the HAP software is not able to perform multiple fits simultaneously. Furthermore there are problems with the handling of the instrument response when analysing On-Off run pairs, which were not taken dedicatedly. However both these characteristics are needed in order to perform the Dark Matter search in the Galactic Centre presented in this work. For this reason a tool that is able to accomplish this task was developed.

In order to perform multiple fits at once the likelihood function of each RoI is added up and maximized (for details on the used Likelihood method see Section 4.8). The instrument response is treated in the following way: First the energy migration matrix for the On run is calculated and weighted with the livetime and effective area.
The counts of the Off run are scaled in each bin (i) of reconstructed energy by the ratio of livetime and effective area from the On-Off pair:

$$N_i = N_i(\text{measured}) \times \frac{T_{\text{On};i} \times A_{\text{On};i}}{T_{\text{Off};i} \times A_{\text{Off};i}} \tag{4.8}$$

This procedure is similar to the way background counts are scaled with the help of α when using the ReflectedBackground method.
As a last step the measured On/Off counts and weighted energy migration matrix are summed from different runs to be able to analyse the entire data set.

To verify that the developed fitting tool produces results compatible to the standard tool provided by HAP, FitSpectrum, several tests were performed. For both data sets (H.E.S.S. I and H.E.S.S. II) the same tests were performed,. Therefore they are only described with the help of the H.E.S.S. II data set, while results for both are given at the end of this section. Only statistical errors will be taken into account.
Some of the functions used in the developed tool are adapted from HAP. For the different tests the source PKS 2155–304 and the above mentioned data set were used. The On data set was analysed using the ReflectedBackground method and the spectrum was reconstructed using FitSpectrum (this is the standard procedure and is used as a reference). Figure 4.23 shows the unfolded spectrum points and the best fit using FitSpectrum. The spectrum was fitted with a power law in the energy range 0.15 – 10 TeV and the best fit values were determined to be 3.160 ± 0.145 for the spectral index and a differential flux of $(1.120 \pm 0.175) \times 10^{-12}\,\mathrm{TeV}^{-1}\mathrm{cm}^{-2}\mathrm{s}^{-1}$ at 1 TeV (data point "FS" in Figure 4.24). When using the developed tool, the fit is converging to the same numbers within numerical precision (data point "M" in Figure 4.24).

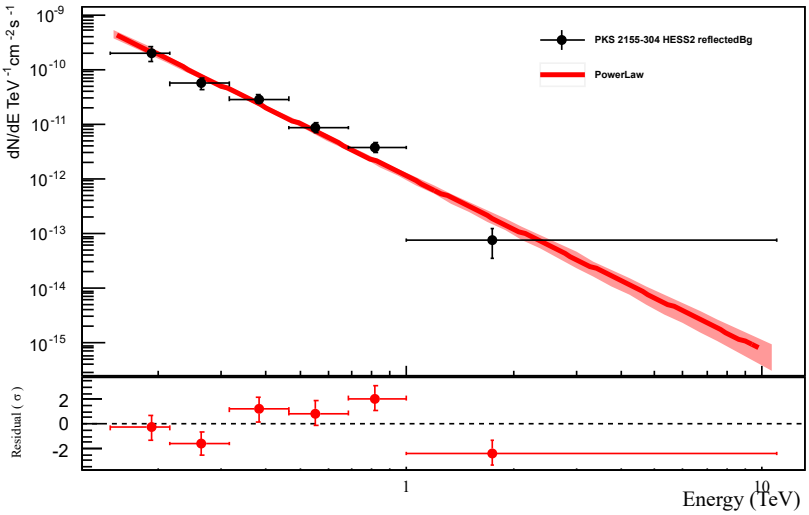

Figure 4.23: Spectrum of PKS 2155–304 using the H.E.S.S. II data set. The spectrum was fitted with a power law using forward folding.

To test the impact of fitting multiple spectra at once, the data set was split into three zenith bands (0 – 20°, 20 – 30° and 30 – 40°) which will later also be used for the line search. Fitting these zenith bands simultaneously gives the result 3.200 ± 0.149 for the spectral index and a flux of $(1.090 \pm 0.179) \times 10^{-12}\,\mathrm{TeV}^{-1}\mathrm{cm}^{-2}\mathrm{s}^{-1}$ at 1 TeV (data point "refZ" in Figure 4.24). Both results are well in agreement within their statistical errors. Typical systematic errors for spectral reconstruction are of the order of 30 % for the spectral index and 0.2 for the spectral index of a power law (Aharonian et al., 2006c). However, it has to be noted that these errors are for less advanced reconstruction techniques and might overestimate the expected systematics within this analysis. With a difference of 0.04 for the spectral index and ≈ 3 % for the flux normalisation the results are in good agreement.

The HAP code responsible for the calculation of the energy migration matrix is not able to calculate the matrix for several regions in the FoV in an efficient way. Therefore an implementation

within the developed tool was made which is able to perform this task. Using this code for the generation of instrument responses and the On and Off counts provided by the ReflectedBackground method, gives the fit result 3.110 ± 0.140 for the spectral index and a differential flux of $(1.130 \pm 0.178) \times 10^{-12}\,\mathrm{TeV}^{-1}\mathrm{cm}^{-2}\mathrm{s}^{-1}$ at 1 TeV (data point “refZmyIR” in Figure 4.24). This result is also in agreement with the previous fits. The difference comes from slight differences in the parametrisation of the analysis region and differences in the binning used.

As the next step the On and Off counts from the ReflectedBackground method were replaced by the output from the OnOffBackground method. The fit was performed in the three zenith bands mentioned above and using the developed implementation of the instrument response extraction. The fit result for the differential flux is $(1.160 \pm 0.173) \times 10^{-12}\,\mathrm{TeV}^{-1}\mathrm{cm}^{-2}\mathrm{s}^{-1}$ at 1 TeV and for the spectral index 3.140 ± 0.134 (data point ”OnOff" in Figure 4.24). Compared to the standard result this is a difference of $\approx 4\,\%$ for the flux normalisation and 0.02 for the spectral index again in good agreement.

All fit results for the H.E.S.S. II data set are shown in Figure 4.24. As one can see, all fits are in good agreement. The results for the H.E.S.S. I data set can be seen in Figure 4.25, all fits were performed in the energy range 0.3 – 10 TeV. It is unclear where the difference in spectral parameters between the H.E.S.S. I and H.E.S.S. II data set comes from. It could be that the source was in a different state at the times of observation or some unknown systematic effect within the look-up tables is causing the difference. Unfortunately it is currently not possible to analyse H.E.S.S. II data using the H.E.S.S. I look-up tables. More studies are needed to answer this question.

As already seen with significance maps in the previous sections the On-Off technique and analyse tools developed in this thesis are able to reproduce the results from H.E.S.S. standard analyses. They will be used in the following analysis of Galactic Centre data.

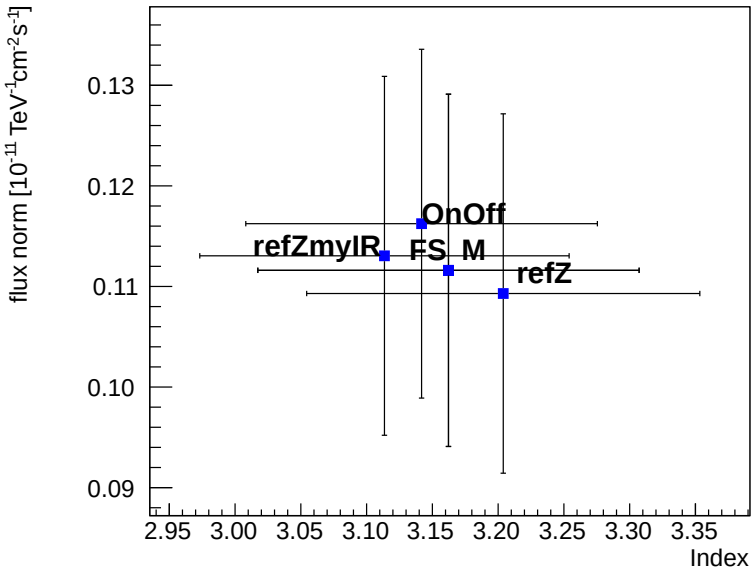

Figure 4.24: Fit results for the different fits of the H.E.S.S. II PKS 2155–304 data set. The data point with the label "FS" is the result of the HAP software. The data point labelled "M" is the result of my code using the instrument response and counts from the ReflectedBackground method. The data point with the label "refZ" corresponds to the fit performed in three zenith bands. The point with the label "refZmyIR" is the result of a fit performed in three zenith bands using my tool for the extraction of instrument responses. The point labelled "OnOff" is the fit result of the OnOffBackground method. All errors shown are statistical errors only.

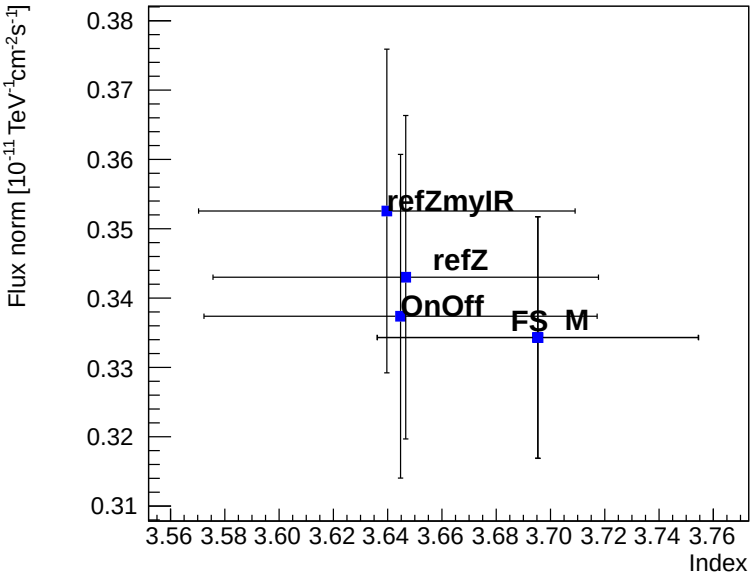

Figure 4.25: Fit results for the different fits of the H.E.S.S. I PKS 2155–304 data set. The data point with the label "FS" is the result of the HAP software. The data point labelled "M" is the result of my code using the instrument response and counts from the ReflectedBackground method. The data point with the label "refZ" corresponds to the fit performed in three zenith bands. The point with the label "refZmyIR" is the result of a fit performed in three zenith bands using my tool for the extraction of instrument responses. The point labelled "OnOff" is the fit result of the OnOffBackground method. All errors shown are statistical errors only.

4.8 Development of a maximum likelihood method

In order to find the model which describes the data best, a maximum likelihood method will be used. The basic idea behind this method is that the likelihoods to measure a set of values are given by the product of the likelihood of measuring each individual value, assuming the measured events are independent.

To get a rough idea: consider tossing a coin N times, where each outcome is independent of the previous one. If it is a regular coin, we expect to see both sides $N/2$ times. The likelihood of a certain outcome after N coin toss is given by the product of the likelihood of each individual toss. Now consider tossing different coins which are marked such that the sides do not show up equally often. Solving this problem becomes significantly harder. If we know how the coins are marked, we can use this information again to describe the observations.
For an experiment like H.E.S.S. the coin toss represents the individual events recorded during data taking and the marked coins represent the instrument response function which is changing with the observation conditions.

In the following I will derive the used likelihood function and further statistical methods used in this work. The content of this section follows mostly Metzger (2010) and Olive et al. (2014).

4.8.1 Principle of the maximum likelihood method

The idea behind the maximum likelihood method is that the likelihood to observe a set of events $\vec{x}$ is given by the product of the likelihoods for each single event (x_i). If all events are independent, the unbinned likelihood function can be written as:

$$\mathcal{L}_D(\vec{x}; M) = \prod_{i=1}^{N} \mathrm{PDF}(x_i; M(\vec{\theta})), \tag{4.9}$$

where the probability to measure x_i is given by the probability density function (PDF), which depends on the model $M(\vec{\theta})$. N denotes the number of events. By varying the model parameters $\vec{\theta}$ one can find the most likely model, i.e. the one that yields the maximum likelihood. In a counting experiment like H.E.S.S. the number of events is not a fixed value, but it is a Poisson distributed number. Therefore the likelihood function has to be extended:

$$\mathcal{L}_D(\vec{x}; M) = \frac{A^N \times e^{-A}}{N!} \times \prod_{i=1}^{N} \mathrm{PDF}(x_i; M(\vec{\theta})). \tag{4.10}$$

Here A is the expected number of observed events, which is derived from the model $M(\vec{\theta})$.

4.8.2 The likelihood function

The previously introduced likelihood function is valid for unbinned data. If the number of events is very large, it can be advantageous to bin the data and use a likelihood function formulated in

terms of the binned data. The likelihood to measure N events in the bin (i, j, k) can be written as:

$$\mathscr{L}(i,j,k) = \frac{(\mu_{i,j,k})^{N_{i,j,k}} \times e^{-\mu_{i,j,k}}}{N_{i,j,k}!}, \tag{4.11}$$

with $\mu_{i,j,k}$ being a prediction of the model $M(\overrightarrow{\theta})$ in the bin (i, j, k), with i the index for bins in reconstructed energy, j for zenith bands and k for region of interest. The likelihood function for the entire event sample is given by the sum over the likelihoods from all bins:

$$\mathscr{L}_D(\overrightarrow{x}; M) = \prod_{i,j,k} \frac{(\mu_{i,j,k})^{N_{i,j,k}} \times e^{-\mu_{i,j,k}}}{N_{i,j,k}!}. \tag{4.12}$$

In the application of this method to search for a Dark Matter signal the model $M(\overrightarrow{\theta})$ contains two components: one describing the background measured in the region of interest and one describing the actual Dark Matter line signal. In the following both components are discussed.

Signal Model

As discussed in Chapter 2 a search for a line-like signal from Dark Matter annihilation was performed. The expected photon flux in true energy is given by (see Section 2.7 for the derivation of Equation 4.13):

$$\frac{\mathrm{d}\Phi}{\mathrm{d}E} = \frac{1}{4\pi} \frac{\langle\sigma v\rangle}{2M_\chi^2} \frac{\mathrm{d}N_\gamma}{\mathrm{d}E} \underbrace{\int_{\text{fov, los}} \int \rho^2 \mathrm{d}s\mathrm{d}\Omega}_{\text{J-Factor}} \tag{4.13}$$

However the fit is performed in reconstructed energy. Therefore the expected photon flux has to be forward folded. The number of expected signal counts in reconstructed energy in the bin (i,j,k) is given by the integral:

$$\begin{aligned}\mu_{\text{signal}}(i,j,k) = \frac{1}{4\pi} \frac{\langle\sigma v\rangle}{2M_\chi^2} \times \underbrace{\int_{E_1}^{E_2} \int_0^\infty \mathscr{M}(E_{\text{true}}, E_{\text{reco}}) \times \frac{\mathrm{d}N_\gamma}{\mathrm{d}E_{\text{true}}} \mathrm{d}E_{\text{true}} \mathrm{d}E_{\text{reco}}}_{\text{i,j}} \\ \times \underbrace{\int_{\text{fov, los}} \int \rho^2 \mathrm{d}s\mathrm{d}\Omega}_{\text{J-Factor (k)}},\end{aligned} \tag{4.14}$$

with E_1, E_2 the edges of the reconstructed energy bin (i) and $\mathscr{M}(E_{\text{true}}, E_{\text{reco}})$ the energy migration matrix weighted by livetime and effective area. The calculation of the J-Factor was already introduced in Section 2.7.1. $\frac{\mathrm{d}N_\gamma}{\mathrm{d}E}$ is given by a delta function which is located at the Dark Matter particle mass.

$$\frac{\mathrm{d}N_\gamma}{\mathrm{d}E} = 2\delta(E_\gamma - m_\chi) \tag{4.15}$$

The factor 2 comes from the fact that a pair of photons is produced in every annihilation. Therefore the only free parameters in our model are the Dark Matter particle mass and the velocity-weighted

annihilation cross section. In the method presented here the particle mass will be scanned in equidistant steps leaving only the cross section as a free parameter of the signal model.

Background Model

Due to the selection of the analysis regions used within this work and the exclusion of known sources, only background from diffuse cosmic rays is expected. Therefore it is sufficient to use the number of measured events in the background regions from the Off runs as an estimate for the number of background events in the On region. This means that the background model $\mu_{\text{background}}(i,j,k)$ is a histogram binned in energy, zenith and RoI. The measured event distribution has to be scaled by the difference in livetime (T) between On and Off runs and the ratio of the area (A) of the analysis region in order to take exclusion regions into account. The expected number of background events can then be written as:

$$\mu_{\text{background,expected}}(i,j,k) = \mu_{\text{background,measured}}(i,j,k) \times \frac{T_{\text{On}}}{T_{\text{Off}}} \times \frac{A_{\text{On}}}{A_{\text{Off}}} \tag{4.16}$$

From the excluded significance maps shown in Chapter 4 we know that the background is overestimated and carries some additional systematic uncertainties. In order to take this into account, the normalization of the background is taken as a free parameter in the fit, which is expected to remain close to 1. As we have seen, the width of the entry distribution of the excluded significance maps was not the value of 1, expected for the case of purely statistical uncertainties. Assuming a systematic error of size σ_{syst} to be present, the total width of the significance distribution can be written as

$$\sigma = \sqrt{\sigma_{\text{stat}}^2 + \sigma_{\text{syst}}^2} = \sqrt{1 + \sigma_{\text{syst}}^2}, \tag{4.17}$$

with the statistical error σ_{stat} set to 1. The value of σ_{syst} will be derived from the Galactic Centre maps before the likelihood fit is performed. In order to take this into account we can extend the likelihood function with a nuisance term (Rolke et al., 2005). Under the assumption that the systematic error is Gaussian-distributed, the term

$$\mathscr{L}_S = \frac{1}{\sqrt{2\pi}\sigma_\alpha} \times e^{-\frac{(1-\alpha)^2}{2\sigma_\alpha^2}} \tag{4.18}$$

is multiplied to the likelihood, where α is the normalisation of the background and $\sigma_\alpha = \sigma_{\text{syst}}$ the error derived from the maps.

Construction of the likelihood function

Putting all the pieces together, we obtain the likelihood function:

$$\mathscr{L} = \prod_{i,j,k} \underbrace{\frac{(\mu_{i,j,k})^{N_{\text{On};i,j,k}} \times e^{-(\mu_{i,j,k})}}{N_{\text{On};i,j,k}!}}_{\mathscr{L}_D(\text{On})} \times \underbrace{\frac{(\mu_{b;i,j,k})^{N_{\text{Off}};i,j,k} \times e^{-(\mu_{b;i,j,k})}}{N_{\text{Off};i,j,k}!}}_{\mathscr{L}_D(\text{Off})} \times \underbrace{\frac{1}{\sqrt{2\pi}\sigma_\alpha} \times e^{-\frac{(1-\alpha)^2}{2\sigma_\alpha^2}}}_{\mathscr{L}_S}, \tag{4.19}$$

where $\mathscr{L}_D$(On/Off) describes the measurement in the On/Off region and $\mathscr{L}_S$ the background systematics. The model $\mu_{i,j,k}$ is the sum of the signal prediction and the background prediction:

$$\mu_{i,j,k} = \mu_{\text{signal}}(i,j,k) + \alpha\mu_{\text{background,expected}}(i,j,k). \tag{4.20}$$

Minimizing $-\ln(\mathscr{L})$ is equivalent to maximizing the likelihood function $\mathscr{L}$, but has the benefit that the product is converted into a sum and that from a computing point of view minimizing is easier than maximizing:

$$\begin{aligned} -\ln(\mathscr{L}) = \sum_{i,j,k} & -N_{\text{On};i,j,k}\ln(\mu_{i,j,k}) + \mu_{i,j,k} + \ln(N_{\text{On};i,j,k}!) \\ & - N_{\text{Off};i,j,k}\ln(\mu_{b;i,j,k}) + \mu_{b;i,j,k} + \ln(N_{\text{Off};i,j,k}!) \\ & + \ln(\sqrt{2\pi\sigma_\alpha}) + \frac{(1-\alpha)^2}{2\sigma_\alpha^2}. \end{aligned} \tag{4.21}$$

The constant terms $\ln(N_{\text{On};i,j,k}!)$, $\ln(N_{\text{Off};i,j,k}!)$ and $\ln(\sqrt{2\pi\sigma_\alpha})$ can be dropped since they do not influence the position of extrema, simplifying the equation to

$$\begin{aligned} -\ln(\mathscr{L}) = \sum_{i,j,k} & -N_{\text{On};i,j,k}\ln(\mu_{i,j,k}) + \mu_{i,j,k} \\ & - N_{\text{Off};i,j,k}\ln(\mu_{b;i,j,k}) + \mu_{b;i,j,k} \\ & + \frac{(1-\alpha)^2}{2\sigma_\alpha^2}. \end{aligned} \tag{4.22}$$

At this point the Likelihood function has three free parameters, the Dark Matter mass, the velocity-weighted annihilation cross section and the background normalization α. The Dark Matter mass will be scanned in range 0.178 – 23.71 TeV in 18 logarithmically spaced steps. This leaving two fit parameters $\langle\sigma v\rangle$ and α. To find the minimum of this equation the minimizer Minuit was used within ROOT.

4.8.3 Test statistic and significance estimation

The question we wish to answer is: do we detect a Dark Matter signal and if yes, how significant? This question can be answered with the help of the test statistic, which is defined as:

$$TS = -2\ln\frac{\sup\mathscr{L}(H_1)}{\sup\mathscr{L}(H_0)} = -2(\ln\sup\mathscr{L}(H_1) - \ln\sup\mathscr{L}(H_0)), \tag{4.23}$$

where $\sup\mathscr{L}(H_0)$ is the independently maximized likelihood of the null hypothesis (all events are considered background) and $\sup\mathscr{L}(H_1)$ the maximized likelihood of the hypothesis that the observation is not compatible with pure background. According to Wilk's theorem (Wilks, 1938) the TS value is distributed like a χ^2 distribution for the limit of large statistics with degrees of freedom $n = d(H_1) - d(H_0) = 2 - 1$, where $d(H)$ is the number of degrees of freedom of the used model. The significance of H_1 is then given by $N_\sigma \simeq \sqrt{TS}$.
At a given test mass, a value of $TS \geq 25$ is taken as a discovery threshold for a putative Dark

Matter signal. In case of $TS < 25$, the null hypothesis H_0 is accepted, and an upper limit on the velocity-weighted annihilation cross section is calculated.

4.8.4 Limit calculation

In order to derive upper limits for the velocity-weighted annihilation cross section the confidence interval has to be calculated. The upper bound of a 90 % confidence interval is equal to the upper limit at 95 %. This corresponds to $\Delta TS = 2.71$ for the test statistic defined in Equation 4.23 with one degree of freedom. It can be calculated by scanning the equation varying the likelihood function of H_1 starting from $\langle \sigma v \rangle = 0$ until the desired TS value is reached.

Expected limits are calculated from 1000 Monte Carlo samples generated from the measured On and Off count distribution. For each simulated sample upper limits are derived. The median limit is used as expected limit and from the distribution of limits 68 % and 95 % containment intervals are calculated. In order to reduce the impact of fluctuations at high energies, where only few events are measured, a template distribution was generated and used in the Monte Carlo simulation. The template is the scaled mean count distribution from the measured distributions of the nine RoI from one zenith band. Figure 4.26 shows this distribution for the H.E.S.S. II data set in the zenith band from 0° to 20°. As one can see, the distributions have the same shape for each RoI. Furthermore the impact of the increased statistics can be seen above 1 TeV where the shape of the distribution is dominated by Poisson fluctuations.

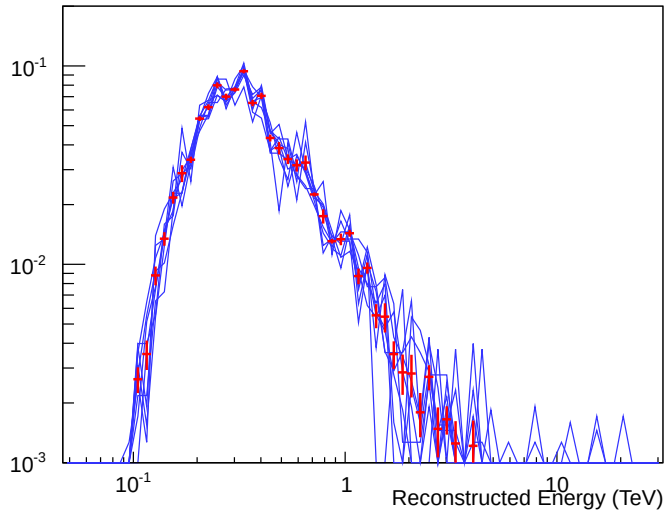

Figure 4.26: Measured Off-count distributions from the H.E.S.S. II data set in the first zenith band (0° to 20°). The blue lines show the distributions from the 9 regions of interest (scaled in order to take different exposures and areas into account). The data points are connected by a line to guide the eye. The red points show the template distribution with errors.

4.8.5 Combined likelihood for H.E.S.S. I and H.E.S.S. II data

Combining measurements of different experiments is a common strategy in particle physics. It helps to increase the statistics of a search and therefore the sensitivity. An example for the application of such a combined analysis is the measurement of the Higgs boson at the LHC where the data taken by ATLAS and CMS were combined (Aad et al., 2016). The two phases of the H.E.S.S. experiment behave too differently for simple stacking of the data, however in a maximum likelihood analysis the data sets can be combined by multiplying the individual likelihoods.

4.9 Analysis requirements - update

As discussed in Section 2.8, several requirements have to be fulfilled in order to perform a sensitive analysis. They were formulated as:

- A good energy resolution in order to resolve a line-like signal
- High sensitivity in the GeV to TeV energy range
- Good background suppression
- Careful selection of the analysis region

As we have seen in the previous chapter the first three requirements can be fulfilled by using an ImPACT based event reconstruction with TMVA for γ/hadron separation.
As shown in this chapter a large analysis region round the Galactic Centre can be analysed by using the introduced On-Off technique for background estimation. With the help of a test analysis it was shown that the developed run pairing is able to find suitable Off runs.
Due to the used likelihood method it is possible to combine data from both phases of the H.E.S.S. experiment increasing the total livetime.
In the following chapter the results of the Dark Matter line-signal search will be shown.

Chapter 5

Results of the Galactic Centre analysis

5.1 Run pairing statistics

The run pairing for the H.E.S.S. I data set resulted in 98 run pairs which means that a suitable Off run could be found for 45 % of all On runs. This results in a decrease of a factor 3 in observation time compared to previous publications (Abramowski et al., 2013). The use of the On-Off analysis improves the effective J-Factor ($J_{\mathrm{On}} - J_{\mathrm{Off}}$) by a factor of 2-3 and further; due to the improved high-level analysis the limits are expected to be in the same range or better. For the H.E.S.S. II data set 77 pairs were found (34 % of all On runs have a fitting Off run). The lower fraction of run pairs found for the H.E.S.S. II data set is due to the much smaller Off run sample. The mean zenith angle of the runs in both data sets is ≈17°. The energy threshold is 150 GeV for the H.E.S.S. II data set and 200 GeV in the case of the H.E.S.S. I data set. All numbers are summarized in Table 5.1. The run lists can be found in Appendix D.1.

Table 5.1: Statistics of the run pairing result for both Galactic Centre data sets.

	H.E.S.S. I	H.E.S.S. II
Run pairs	98	77
Observation time On	40.8 h	30.2 h
Observation time Off	43.7 h	31.4 h
Energy threshold	200 GeV	150 GeV
Mean zenith angle	16.°4	17.°4

5.2 Results of the OnOffBackground analysis

The analysis of the H.E.S.S. data was carried out as described previously. For both data sets excluded significance maps were produced.
The H.E.S.S. I map can be seen in Figure 5.1 (left). No unexpected features are observed and

the entry distribution (Figure 5.1, right) is well normalized with a width of 1.00 and a mean of -0.03. The width of 1.00 leads to a $\sigma_\alpha = 0$. However using 0 in the likelihood function would lead to a freeze of $\alpha = 1$. In order to prevent this, σ_α is set to 0.2. This is a rather conservative assumption.

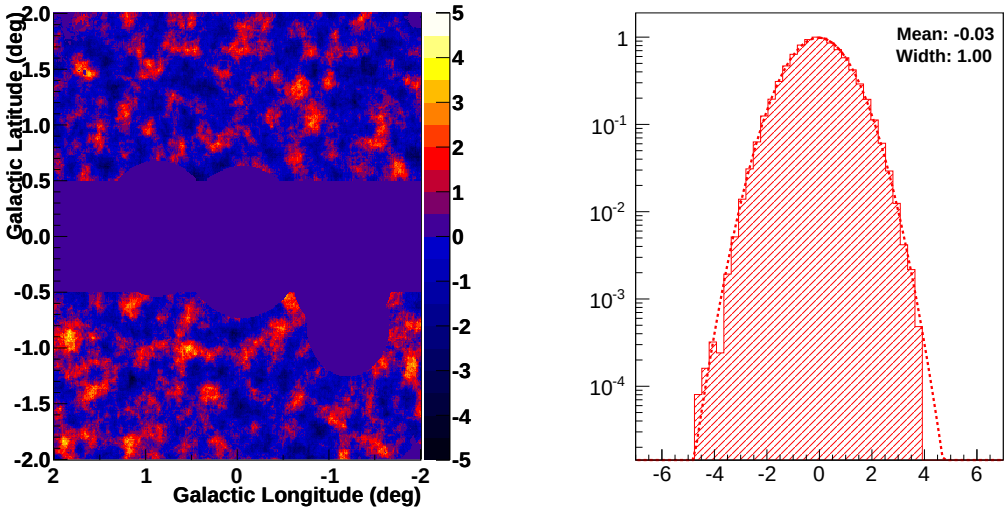

Figure 5.1: Left: Excluded significance map of the GC region from H.E.S.S. I data set. Right: Entry distribution of the map shown on the left. The dashed line is a Gauss fitted to the distribution.

The H.E.S.S. II data show a similar behaviour, the map (Figure 5.2, left) is without significant hotspots or deficits, no gradient is observed. The entry distribution (Figure 5.2, right) has a mean of -0.08 and a width of 1.06. This leads to a $\sigma_\alpha = 0.35$. As already seen in the test analysis of PKS 2155–304, the used On-Off method is capable of producing maps of good quality. With these results both data sets can be analysed without further concern.

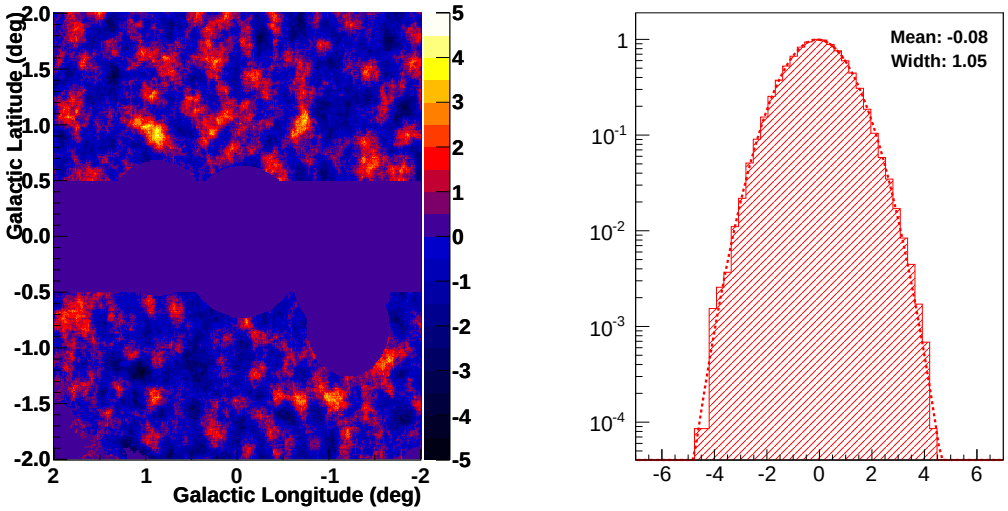

Figure 5.2: Left: Excluded significance map of the GC region from H.E.S.S. II data set. Right: Entry distribution of the map shown on the left. The dashed line is a Gauss fitted to the distribution.

Table 5.2 shows the measured On and Off counts in every RoI for the H.E.S.S. I data set. The fact that in every RoI more events were measured in the Off regions is partially due to the longer observation times in these regions. This however will not lead to any problems in the likelihood fit, since the difference in livetime is taken into account. Furthermore the background normalization is a free parameter to account for possible differences in the background rate. The H.E.S.S. II data set shows a similar behaviour (see Table 5.3). To ensure that the likelihood fit performs in a stable way the data are re-binned to 8 bins per decade in energy in the spectral fit. This ensured that even in RoIs with low statistic, every bin in the analysed energy range should have $\geq$5 counts.

Table 5.2: H.E.S.S. I event statistics for the different RoI. The number of Off counts is not weighted with the livetime or effective area.

RoI number	number On counts	number Off counts
1	137	175
2	460	575
3	554	665
4	634	716
5	675	765
6	695	832
7	701	938
8	735	914
9	775	900
Total	5366	6480

Table 5.3: H.E.S.S. II event statistic for the different RoI. The number of Off counts is not weighted with the livetime or effective area.

RoI number	number On counts	number Off counts
1	229	276
2	775	886
3	921	1178
4	1016	1198
5	1061	1281
6	1156	1414
7	1156	1342
8	1087	1427
9	1157	1419
Total	7497	10 421

5.3 Limits

For each test energy (0.178, 0.237, 0.316, 0.422, 0.562, 0.75, 1, 1.334, 1.778, 2.371, 3.162, 4.217, 5.62, 7.499, 10, 13.335, 17.783, 23.714 TeV) the velocity-weighted annihilation cross section was fitted for both data sets individually as well as for the combined data set. The fit was repeated

for all four considered Dark Matter profiles. No significant Dark Matter signal was found in the analysed energy range for both H.E.S.S. I and H.E.S.S. II as well as for the combined data set. Therefore upper limits for the velocity-weighted annihilation cross section ($\langle\sigma v\rangle$) were calculated. Figure 5.3 shows the measured On count distribution and the expected counts ($\mu_{\text{background}} + \mu_{\text{signal}}$) for a 5-sigma line at 1 TeV.

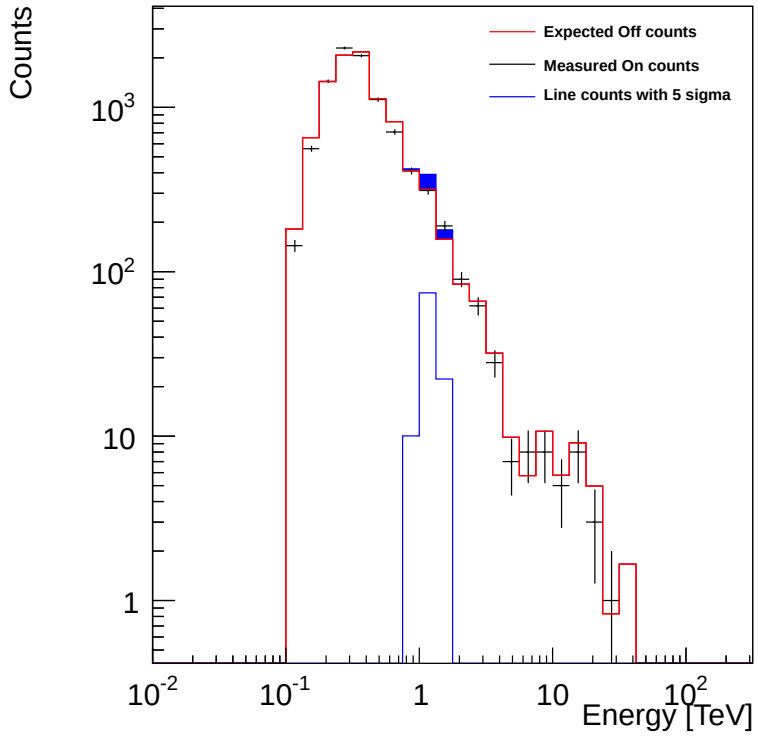

Figure 5.3: Count distribution for the H.E.S.S. II data set, all RoI and zenith bands are stacked. The expected counts from background are shown in red. In blue: counts from a Dark Matter Line with particle mass of 1 TeV with a detection significance of 5 sigma. In black: the measured On counts.

Figure 5.4 shows the limits for all three data sets for the Cored (left) and the Cusped (right) Einasto Dark Matter Halo profiles (see Fig. 2.16). Results for the NFW profiles are shown in Appendix D.6. The limits at 0.178 TeV and 0.237 TeV are very close to the energy threshold (or even below for the H.E.S.S. I data set) and are therefore subject to a large systematic uncertainty. However, they are in agreement with previous publications. Overall the limits behave as expected. With rising energy they improve due to the increasing effective area and livetime. Figure 5.5 shows the effective area × livetime for two regions of interest. At the lowest energies only a fraction of runs contributes due to their energy threshold, while at approximately 1 TeV all runs reach the peak in effective area. At the highest energies the limits worsen again. This is due to the factor of $\frac{1}{M_\chi^2}$ in the expected γ-ray flux from annihilating Dark Matter (see Eq. 4.13). The rather large fluctuations between neighbouring limits are due to the overall low number of counts per bin. This can be seen when comparing the H.E.S.S. I and H.E.S.S. II limits. The fluctuations in the H.E.S.S. II data set are much smaller due to a higher number of total counts. Most limits from the

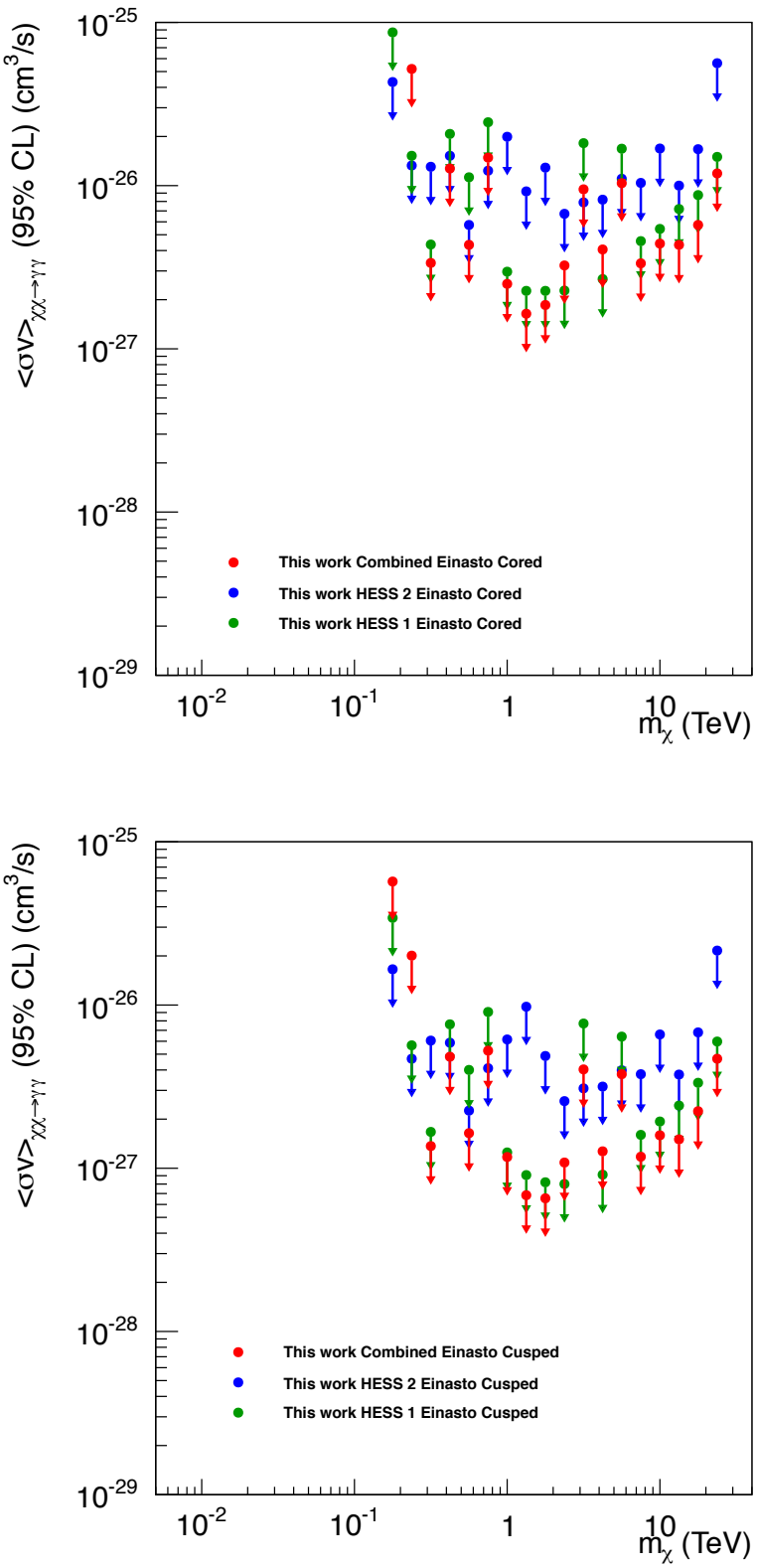

Figure 5.4: Upper limits on the velocity-weighted annihilation cross section assuming an Einasto shaped Dark Matter halo profile for all three data sets. The result for the Cored profile is shown at the top and for the Cusped at the bottom.

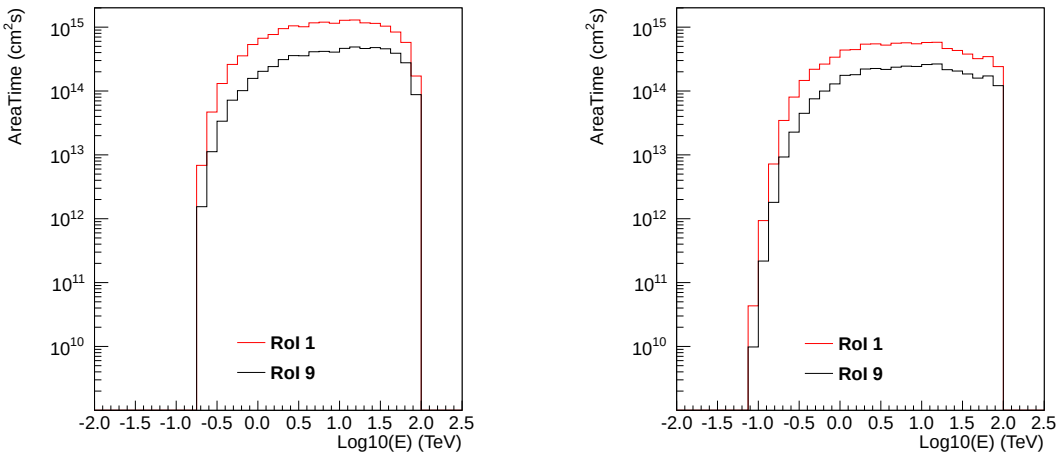

Figure 5.5: Effective area times livetime of the Galcatic Centre data sets. Shown are the curves for RoI 1 and 9. Left: H.E.S.S. I data set. Right: H.E.S.S. II data set.

H.E.S.S. II data set are less strict than the H.E.S.S. I limits. This has two reasons: a lower exposure and a difference in how the exposure is distributed within the Galactic Centre. Due to the larger FoV the coverage of the region of interest is better for the H.E.S.S. I data set (see Fig. 5.6). As shown by the map for H.E.S.S. II most observations were taken above the Galactic plane resulting in a comparably low exposure below the plane. For the H.E.S.S. I data the exposure is more evenly distributed resulting in a better over all coverage.

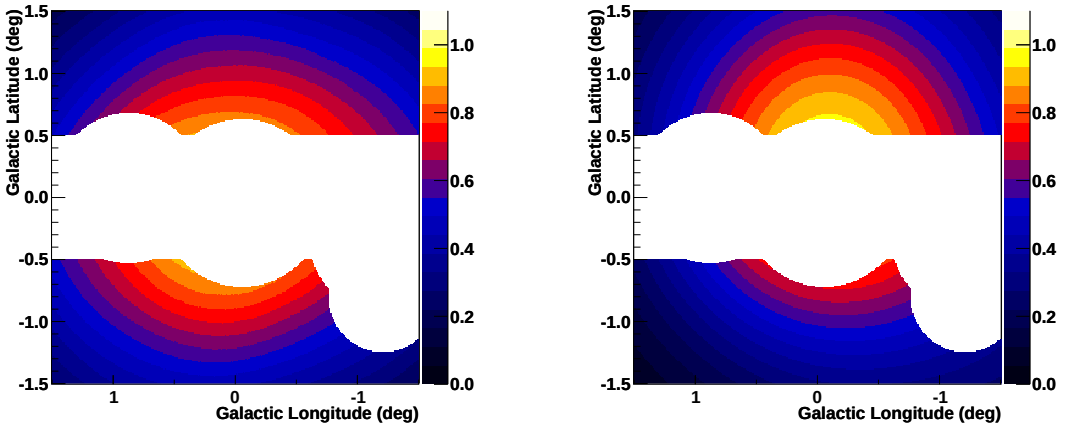

Figure 5.6: Exposure for the Galactic Centre for the H.E.S.S. I (left) and H.E.S.S. II (right) data set. Both maps are normalized to a maximum of 1.

When combining both data sets (see Figure 5.4, red data points), the limits become more restrictive. However, some of the limits for the combined data set are worse than the limits of the individual analyses. This behaviour can be understood, when considering how the two individual log-likelihood functions add up. Figure 5.7 shows examples of log-likelihood profiles for two different Dark Matter particle masses. The top figure (m_χ =3.162 TeV) shows the log-likelihood profiles for the H.E.S.S. I and H.E.S.S. II analyses with a large offset along the abscissa. The log-likelihood profile of the combined analysis (red) is resulting in a better limit compared to only one of the

individual sets. In the bottom figure (m_χ =13.335 TeV) the combined log-likelihood results in a narrower profile, and, correspondingly smaller uncertainties on $\langle \sigma v \rangle$ and therefore better limits. This comes from the fact that the log-likelihood profile of the H.E.S.S. I and H.E.S.S. II data set show only a relatively small offset along the abscissa.

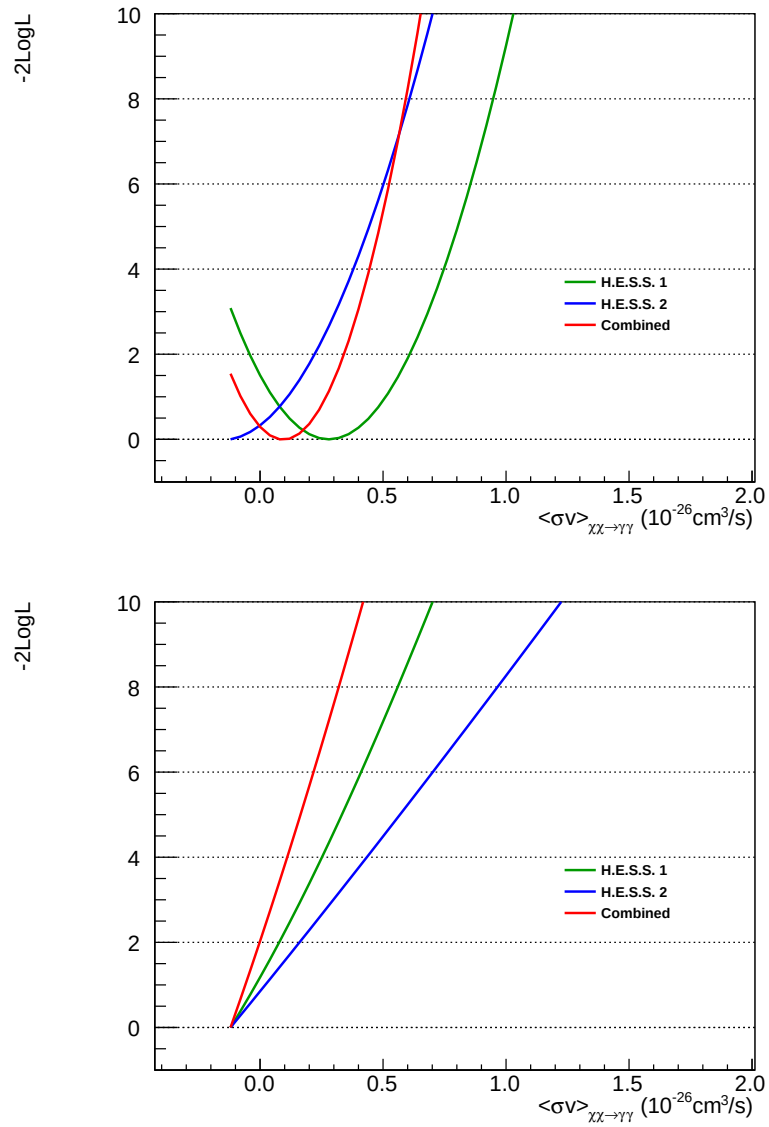

Figure 5.7: Log-likelihood profiles of the Galactic Centre for the H.E.S.S. I, the H.E.S.S. II and the Combined data set are shown. The minimum of the curves was set to 0 for better visualisation. Top: A Dark Matter mass of 3.162 TeV with the Cusped Einasto profile is assumed. Bottom: A Dark Matter mass of 13.335 TeV with the Cusped Einasto profile is assumed.

For all analyses expected limits were derived from simulations. For the combined data set using the Cored and Cusped Einasto DM halo profiles they can be seen in Figure 5.8. Shown are the expected limits and their 68 % and 95 % containment intervals. For the individual data sets as well as for the NFW profiles the limits and expectations can be found in Appendix D.2. As expected, the measured limits fluctuate around the mean expected limits.

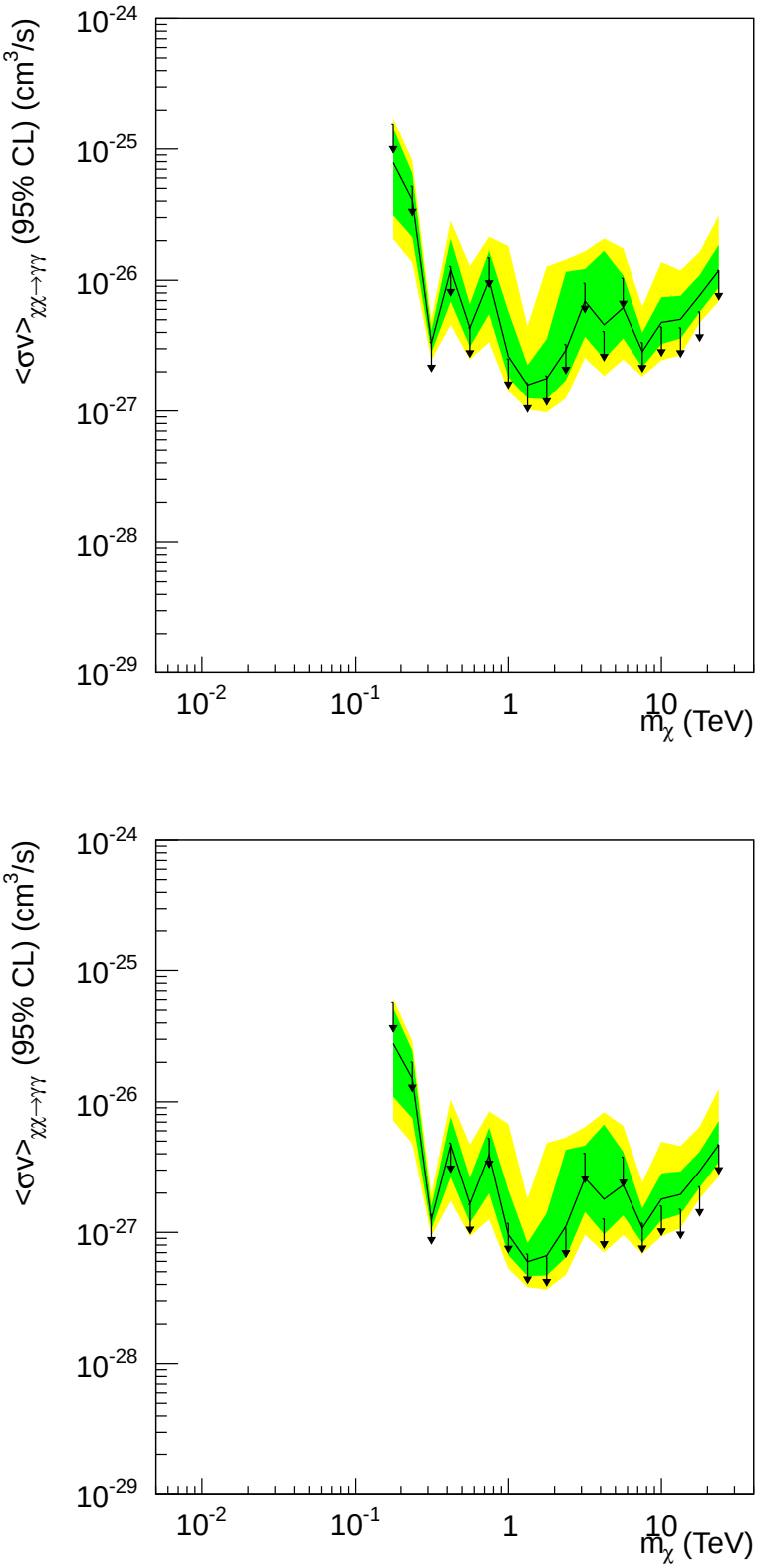

Figure 5.8: Upper limits on the velocity-weighted annihilation cross section assuming an Einasto shaped Dark Matter halo profile for the Combined data set. Shown are measured limits (black arrows), expected limits (black line), 68% containment interval (green) and 95 % containment interval (yellow). The result for the Cored profile is shown at the top and for the Cusped at the bottom.

The fit results for the background normalisation α for both the H.E.S.S. I and the H.E.S.S. II data sets using the Cusped Einasto profile can be seen in Figure 5.9. Only results for one Dark Matter profile are shown due to the fact that the difference for the fitted background normalisations between different profiles is of the order of 10^{-3} for both data sets. With a mean value $\alpha = 1.03$ the background in the H.E.S.S. I data set is slightly underestimated. Two values at 0.42 TeV and 0.75 TeV show large deviation from the mean value. This is coincidental with up fluctuations of the observed limits at the same energies.
In the H.E.S.S. II data set the mean background normalisation is $\alpha = 0.99$. The fluctuations of the fitted α values are smaller compared to the H.E.S.S. I data set, due to the larger statistics. Below an energy of 2 TeV fluctuations are visible and again coincidental with fluctuations of the fitted cross section limits.

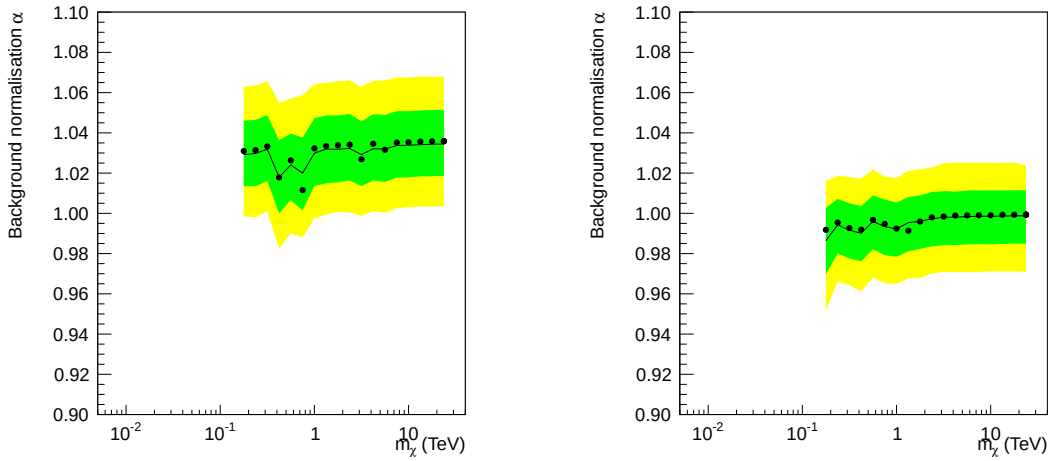

Figure 5.9: Background normalisation for the H.E.S.S. I and H.E.S.S. II data set assuming a Cusped Einasto shaped Dark Matter halo profile. Shown are measured normalisation (black dots), expected normalisation (black line), 68% containment interval (green) and 95 % containment interval (yellow). The result for the H.E.S.S. I data set is shown on the left and for the H.E.S.S. II data set on the right.

Figure 5.10 shows the limits using the combined data set and the Cusped Einasto profile in comparison with other analyses carried out in the past. Due to the small overlap in energy the comparison between the *Fermi*-LAT limits (black points) and the limits derived in this work (red) does not yield a lot of information. Limits above that energy are of the same order as the limits shown by *Fermi*-LAT.
The limits shown by Abramowski et al. (2013) (green) are difficult to compare due to the fact that an entirely different analysis approach was used. However, one can see that the limits derived in this work are lower for energies above ∼1 TeV. This is probably due to the increased sensitivity by using a larger On region which is split into sub-regions to be sensitive to the actual Dark Matter halo profile.
A better comparison is available looking at the expected limits derived in Rinchiuso et al. (2017). In this analysis also a likelihood approach with similar sub-RoI was used. Based on a livetime of about 254 h, the limits are expected to be a factor of $\sqrt{3}$ better. For two identical analyses the limits scale with the squared root ratio of the livetimes. However, due to the fact that a

ReflectedBackground method was used, the Off regions contain a rather large fraction of Dark Matter, which has to be corrected in the $\langle \sigma v \rangle$ calculation. This can result in an increase of the expected limits by a factor $2-3$ depending on the exact Off region choice. There are further differences in Further differences analysis region, and in Rinchiuso et al. (2017) the events were analysed using Model++ and the analyses presented here are using the true energy resolution instead of a Gaussian function (as used in Rinchiuso et al. (2017)). The observed limits are a factor of $2-3$ better above 8 TeV compared to the expectation of Rinchiuso et al. (2017). In the energy range of $2-8$ TeV the limits are of the same order. Below this energy the faster falling effective area (due to only analysing events with four telescopes) results in worse limits. It is not fully understood why the observed limits behave in this way.

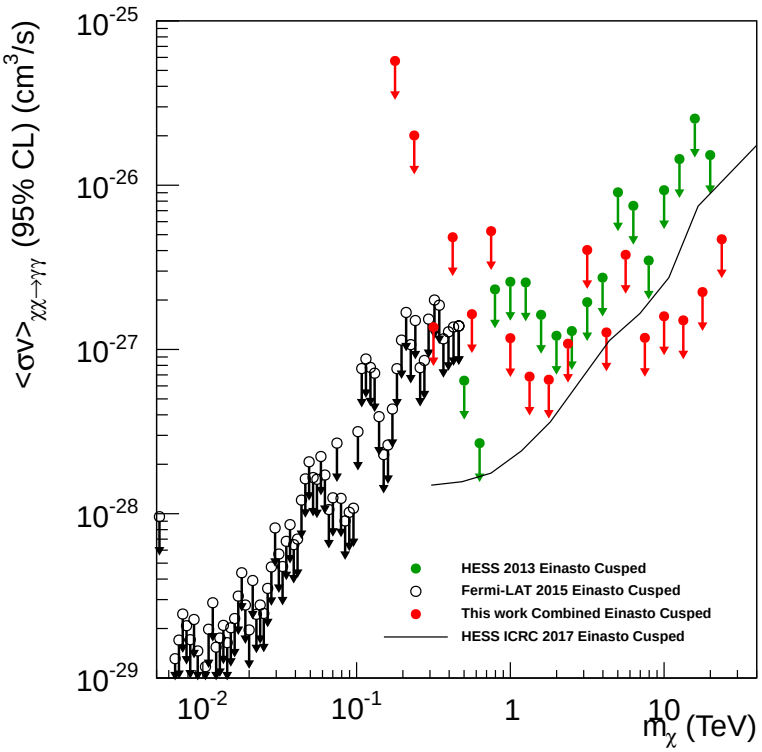

Figure 5.10: Upper limits on the velocity-weighted annihilation cross section assuming a Cusped Einasto shaped Dark Matter halo profile. *Fermi*-LAT (black points) data are taken from Ackermann, Ajello, et al. (2015), H.E.S.S. (green points) data are taken from Abramowski et al. (2013), expected limits for H.E.S.S. (black line) are taken from Rinchiuso et al. (2017). Limits for the combined data set from this work are shown in red.

For the H.E.S.S. II data set a study was performed to investigate how a different choice of RoI impacts the resulting cross section. For this 1000 Monte Carlo realisations of the data set were simulated and limits were derived just using the innermost RoI, then taking the first two and so on until all regions were analysed. This is equivalent to increasing the analysed region in steps of $0.^{\circ}1$, until the region reached the size shown in Figure 4.1. This was done for the Cored and Cusped Einasto profile. The result can be seen in Figure 5.11. The data points show the median upper limit and the error bars indicate the 68 % containment interval for the cross section of a

Dark Matter particle mass of 1 TeV. For the Cored profile (red) the limits decrease proportionally to $\frac{1}{r}$. This is expected for a constant profile due to expected limits scaling with $\sqrt{\text{counts}}$, which is comparable with the dependence on livetime. The function

$$\langle \sigma v \rangle = a + \frac{b}{r} \tag{5.1}$$

was fitted to the data to illustrate this behaviour. Not taken into account by this model is the inhomogeneous exposure. However, the decrease from the innermost RoI to the outermost is about 50 %. This should lead only to a small deviation compared to the simple model, especially as the decrease is also smooth.

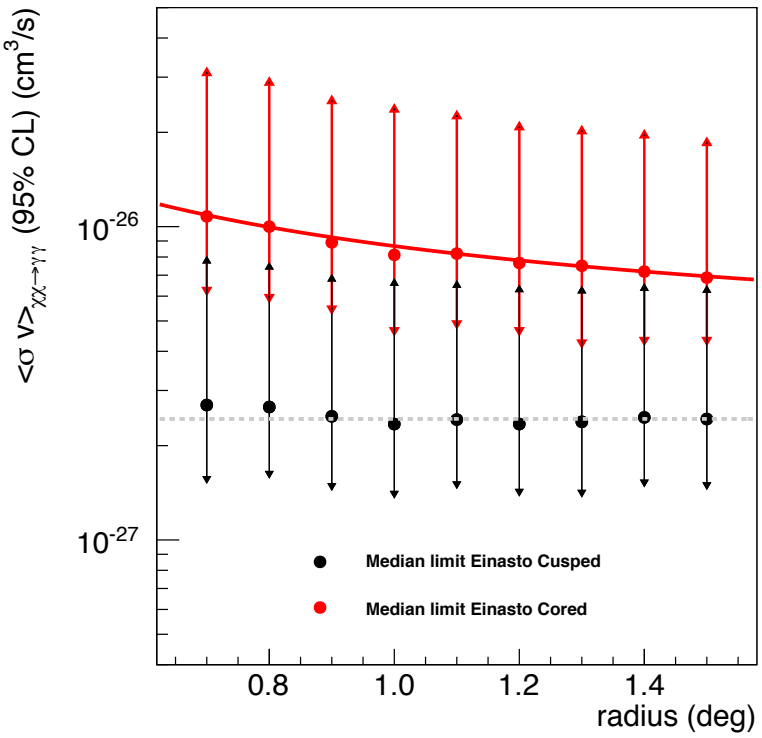

Figure 5.11: Expected limits depending on the analysed RoI size. The data points show the median upper limit and the error bars give the 68 % containment interval for the cross section of a Dark Matter particle with 1 TeV mass depending on the outer radius of the analysed region. The data points of the Cored DM profile (red) were fitted with a function $\propto \frac{1}{r}$ (solid black line). The data points of the Cusped DM profile (black) were fitted with a constant (grey dashed line).

For the data points corresponding to the Cusped profile (black) no simple physically motivated model was found. To guide the eye, a constant value was fitted to the data. For this profile shape two effects work against each other. With the increase of the RoI one would expect the limits to improve as in the case of a Cored profile. However, due to the decreasing Dark Matter density, the impact of regions with larger distance to the Galactic Centre is declining, until no further improvement can be seen. This second effect is amplified due to the decreasing exposure with increasing distance to the Galactic Centre. Taking a close look at the data one could see a hint for

improving limits at the first four data points, however this is far from significant.
A similar study was performed in a Monte Carlo study for CTA using the ReflectedBackground method (Römmelt, 2015), where a growing RoI was considered. Three problems arise when comparing the results:

- Due to the different background method the effective J-Factor behaves differently.
- Only a growing (instead of multiple) RoI was considered, therefore only the average J-Factor contributes.
- The study was performed for continuous γ-ray emission instead of line emission.

The result of this study can be seen, in Figure 5.12. As one can clearly see the shape of the limits

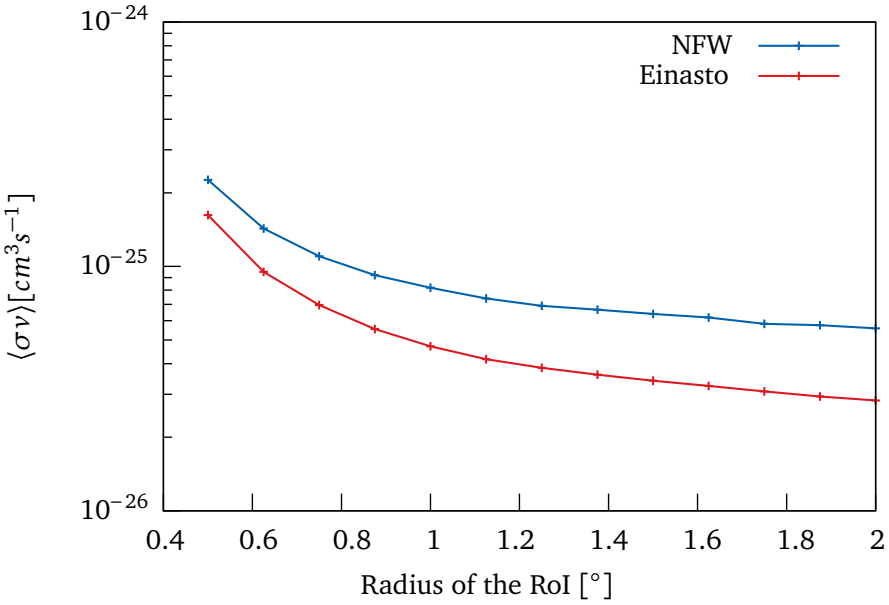

Figure 5.12: Upper limits on $\langle\sigma v\rangle$ depending on the radius of the RoI. Limits for Cusped Einasto and NFW profiles are shown. Figure modified from Römmelt (2015).

derived in Römmelt (2015) is similar to the shape of the results for the Cored profile derived in this work (see Fig. 5.11 red data points). This might seem odd, since different profile shapes are used. However due to the fact that in Römmelt (2015) a growing RoI was used. The J-Factor is with every step averaged over a larger region. Therefore it is behaving like a constant density profile, where between the individual RoI sizes the normalization slightly changes. Which leads to a similar behaviour as the results shown for a Cored profile in this work.

Chapter 6

Summary

There are several ways to improve the analysis presented in this thesis. The most obvious is to enlarge the used data set by adding newly taken data and by trying to improve the run pairing to find more Off runs. The limit for the velocity-weighted annihilation cross section is proportional to $\frac{1}{\sqrt{t}}$. Due to the already performed optimization for the run pairing, it is not expected to gain more than a factor of $\sqrt{2}$ with this improvement. The impact of additional data is hard to estimate, since it is unknown, whether in the pairing process the new data behaves in the same way or if additional corrections have to be applied. Due to a larger period of time from which the data are taken, differences in the telescope behaviour because of ageing become larger. This might introduce additional systematics.

Another possibility to improve the analysis is to combine the H.E.S.S. results with data from other experiments. Within the maxumum likelihood analysis presented here this is possible. *Fermi*-LAT as well as other Cherenkov telescopes would be good candidates for this, because they overlap in the analysed energy range. Using *Fermi*-LAT data would especially improve the limits at lower energies.

Furthermore it might be possible to create an all sky background model which can be used as a template making the run pairing unnecessary. This would allow to use all the available data from the Galactic Centre. However, this method would be limited by the accuracy of the background template. The background systematics in H.E.S.S. is of the order of 1 – 2 % for the Ring- and ReflectedBackground method. From the various skymaps shown one can assume that the systematic of the used On-Off method is in the same order. Figure 6.1 shows the accumulated number of counts per square degree. For H.E.S.S. II the systematic error would exceed the statistical error of 1 % after about 35 h. If in the H.E.S.S. II analysis runs with four telescopes are allowed as well, the time will increase up to a factor of 2, due to the lower count rate with one missing telescope. For H.E.S.S. I this limit would only be reached only after 200 h because of the even lower event rate. This is a rather rough estimation and can easily change by a factor of two or more due to changes in the RoI. Extending the analysis in this way would lead to an improvement of the limits by a factor of about $\sqrt{5}$.

With the next generation of Cherenkov telescopes coming, namely the Cherenkov Telescope Array (CTA), new possibilities for the search of Dark Matter arise. CTA is currently in the pre-construction

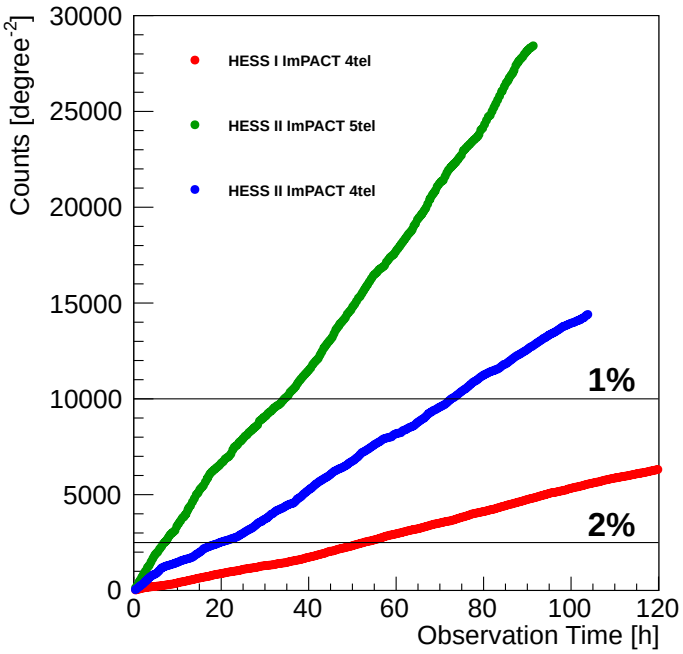

Figure 6.1: Accumulated number of counts per square degree. The data used are the observations included in the background study. The H.E.S.S. I data shown (red) include only events seen by four telescopes. The H.E.S.S. II data (blue) include only runs with four telescopes and events with at least four telescopes participating. The H.E.S.S. II data (green) includes only runs with five telescopes and events with at least four telescopes participating. Two horizontal lines give the number of counts needed to have the statistical error as small as a systematic error of 1 % or 2 %.

phase with prototype telescopes being tested (CTA Consortium, 2017). It is planned to build two arrays, one on La Palma (CTA North) and one in Chile (CTA South). The array will consist of three different telescope types optimised for different energy ranges. This will lead to improved sensitivity, energy and angular resolution in a range of 20 GeV to 300 TeV.
One of the major scientific topics of CTA will be the search for Dark Matter (CTA Consortium et al., 2017). Due to a large FoV ($\approx 8°$) more extended RoI can be analysed using the ReflectedBackground method with a larger effective J-Factor at the same time. It is expected that the sensitivity improves by one order of magnitude compared to current Cherenkov telescopes like H.E.S.S. This will improve limits by a factor of $\sqrt{10} \approx 3$, not taking the larger FoV into account. Further improvement from better background rejection and more advanced analysis techniques are expected. According to the search strategy proposed in CTA Consortium et al. (2017) it is not planned to take On-Off run pairs with CTA. However, as shown in this work, it is possible to find run pairs for a mixed telescope array. This leads to the conclusion that the method used in this work can also be used for CTA data. Furthermore the science program of CTA is proposing to use a very similar Likelihood method as used here.
In new analysis tools developed for CTA (e.g. ctools Knödlseder et al. (2016)) a full modelling of the data is done. With the help of accurate background models such an analysis does not need control regions for background estimation and therefore opens up new perspectives for Dark Matter searches in the Galactic Centre allowing more possibilities for the selection of the analysis region.

Appendix A

Trigger

Table A.1: The different trigger pattern and read-out pattern for all events within an observation run of the H.E.S.S. II phase with four telescopes active (Run 95625, mean zenith angle 32°). The missing telescope is CT4. Multi 4 corresponds to events with all four telescopes participating.

trigger type	total triggers	CT5 mono read-outs	CT1-5 stereo read-outs	CT1-4 stereo read-outs	dropped	multi 4 read-outs
CT5 mono	81.4%	95.6%	0.0%	0.0%	4.4%	0.0%
CT1-CT5 stereo	14.7%	7.0%	88.6%	3.8%	0.6%	11.6%
CT1-CT4 stereo	3.9%	0.0%	0.0%	52.0%	48.0%	0.0%
Sum	100%	78.9%	13.1%	2.6%	5.5%	1.7%
Multi 4	2.2%	2.4%	93.2%	4.2%	0.2%	77.2%

Table A.2: The different trigger pattern and read-out pattern for all events within an observation run with all four telescopes active (Run 67311, mean zenith angle 18°). Multi 4 corresponds to events with all four telescopes participating.

trigger type	total triggers	CT1-CT4 stereo read-outs	dropped	multi 4 read-outs
CT1-CT4 stereo	100.0%	94.9%	5.1%	17.5%
Multi 4	19.6%	99.1%	0.9%	89.6%

Appendix B

Parameter Correlations

Tables can be found on the following pages. Table B.1 for the H.E.S.S. II data set with four telescopes and Table B.2 for the H.E.S.S. I data set.

Table B.1: Correlation coefficients for the H.E.S.S. II data set with four telescopes active. For the parameter 3 to 6 the mean value over all telescopes is used. For parameter 9 and 11 the mean value for the four small telescopes is used.

	Air Temperature	Relative humidity	Zenith angle	Azimuth angle	Radiometer Temperature	Broken pixel fraction	event rate	NSB rate CT5	NSB rate CT1-CT4	Muon efficiency CT5	Muon efficiency CT1-CT4
(1) Air Temperature	1	−0.14	0.32	−0.03	0.60	0.08	0.18	0.18	0.30	0.05	−0.19
(2) Relative humidity		1	0.10	−0.05	0.10	−0.09	−0.04	0.15	−0.01	0.25	−0.15
(3) Zenith angle			1	−0.15	0.19	−0.06	0.31	0.34	0.34	0.17	0.03
(4) Azimuth angle				1	0.03	0.03	0.01	−0.10	−0.05	0.03	0.07
(5) Radiometer Temperature					1	0.03	0.15	0.03	0.24	0.07	0.23
(6) Broken pixel fraction						1	0.05	0.01	0.03	0.01	−0.02
(7) event rate							1	0.26	0.31	−0.06	0.16
(8) NSB rate CT5								1	0.88	0.10	0.13
(9) NSB rate CT1-CT4									1	0.21	0.39
(10) Muon efficiency CT5										1	−0.13
(11) Muon efficiency CT1-CT4											1

Table B.2: Correlation coefficients for the H.E.S.S. I data set. For the parameter 3 to 6 the mean value over all telescopes is used.

	Air Temperature	Relative humidity	Zenith angle	Azimuth angle	Radiometer Temperature	Broken pixel fraction	event rate	NSB rate CT1-CT4	Muon efficiency CT1-CT4
(1) Air Temperature	1	−0.16	−0.05	−0.09	0.68	0.29	−0.13	0.07	−0.02
(2) Relative humidity		1	−0.01	0.06	0.15	0.01	0.18	0.11	0.13
(3) Zenith angle			1	−0.02	0.04	−0.17	0.49	0.09	0.03
(4) Azimuth angle				1	−0.09	0.01	0.02	0.02	0.02
(5) Radiometer Temperature					1	0.13	−0.04	0.06	0.04
(6) Broken pixel fraction						1	−0.11	0.21	−0.06
(7) event rate							1	0.22	0.57
(8) NSB rate CT1-CT4								1	0.21
(9) Muon efficiency CT1-CT4									1

Appendix C

BG rate dependence

C.1 H.E.S.S. I data set

Plots for the H.E.S.S. I data set. All plots show one of the studied parameters on the abscissa and $\frac{\text{BG rate}_{\text{measured}}}{\text{BG rate}_{\text{expected}}}$ on the ordinate.

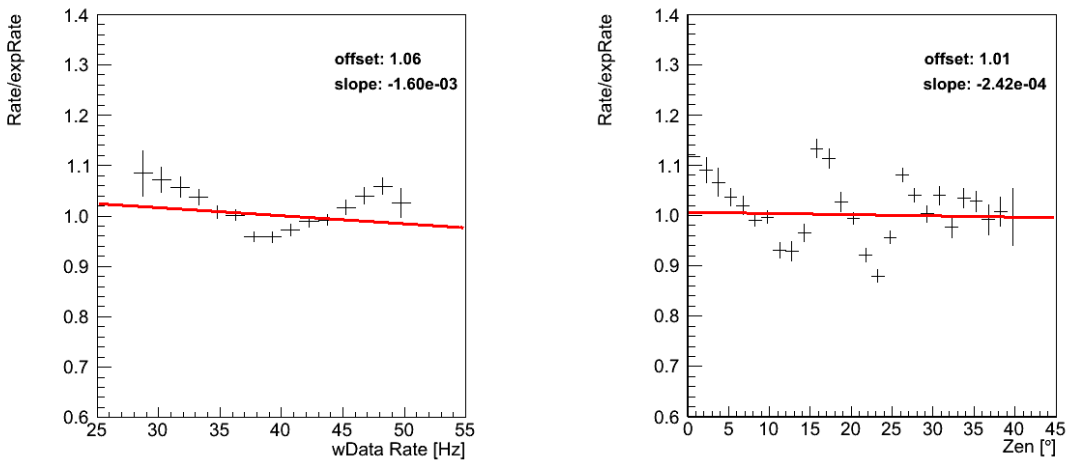

Figure C.1: Left: $\frac{\text{BG rate}_{\text{measured}}}{\text{BG rate}_{\text{expected}}}$ depending on event rate in H.E.S.S. I data. Right: $\frac{\text{BG rate}_{\text{measured}}}{\text{BG rate}_{\text{expected}}}$ depending on zenith angle in H.E.S.S. I data.

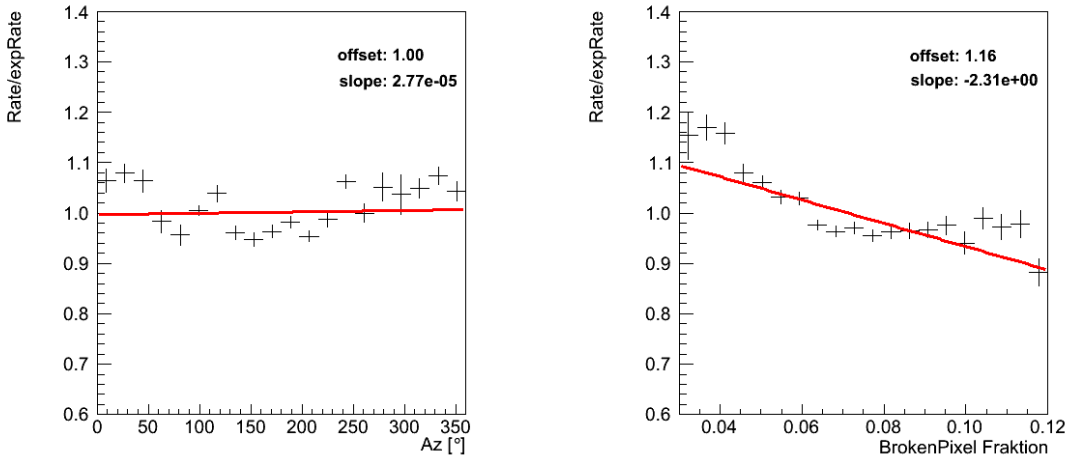

Figure C.2: Left: $\frac{\text{BG rate}_{\text{measured}}}{\text{BG rate}_{\text{expected}}}$ depending azimuth angle in H.E.S.S. I data. Right: $\frac{\text{BG rate}_{\text{measured}}}{\text{BG rate}_{\text{expected}}}$ depending on the averaged broken pixel fraction in CT1-CT4 in H.E.S.S. I data.

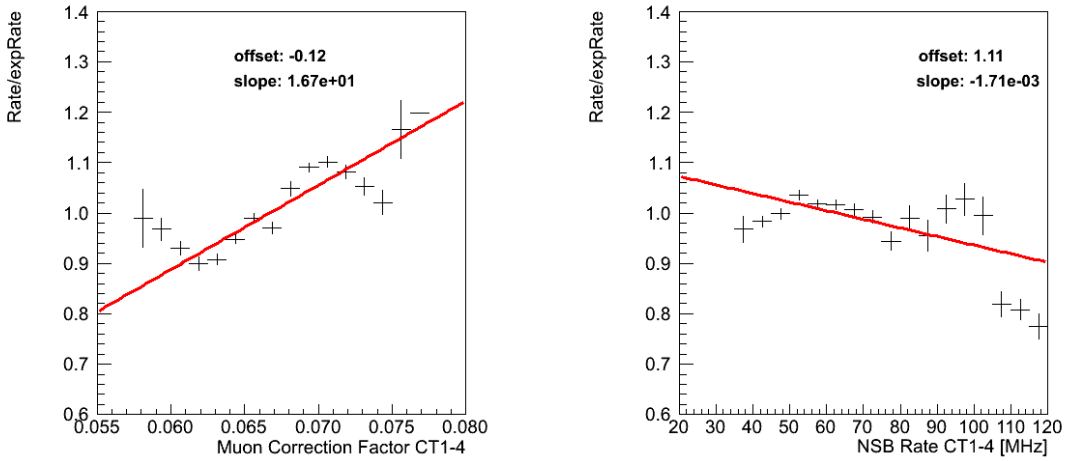

Figure C.3: Left: $\frac{\text{BG rate}_{\text{measured}}}{\text{BG rate}_{\text{expected}}}$ depending on the averaged muon efficiency factor of CT1-CT4 in H.E.S.S. I data. Right: $\frac{\text{BG rate}_{\text{measured}}}{\text{BG rate}_{\text{expected}}}$ depending on the averaged NSB rate in CT1-CT4 in H.E.S.S. I data.

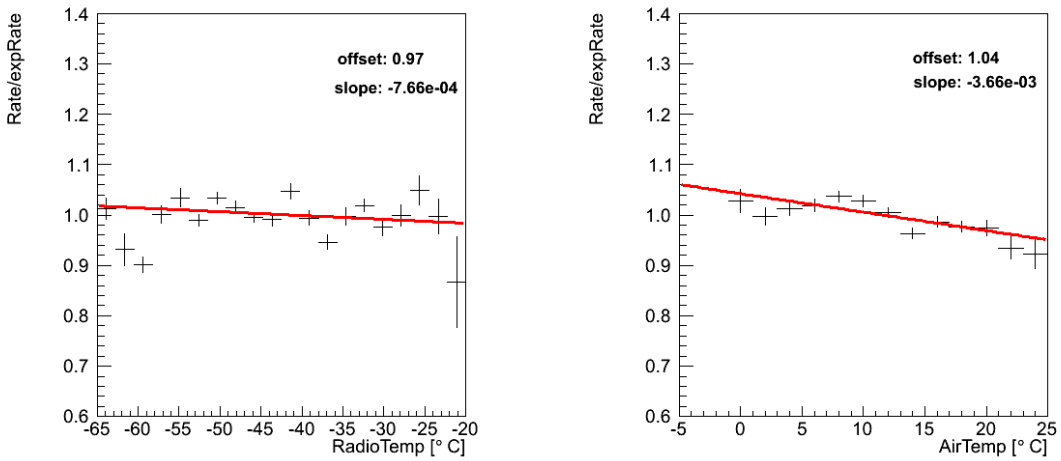

Figure C.4: Left: $\frac{\text{BG rate}_{\text{measured}}}{\text{BG rate}_{\text{expected}}}$ depending on the averaged radiometer temperature in CT1-CT4 in H.E.S.S. I data. Right: $\frac{\text{BG rate}_{\text{measured}}}{\text{BG rate}_{\text{expected}}}$ depending on the air temperature at ground in H.E.S.S. I data.

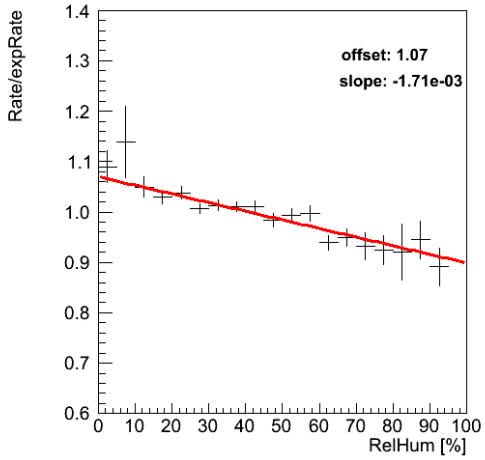

Figure C.5: $\frac{\text{BG rate}_{\text{measured}}}{\text{BG rate}_{\text{expected}}}$ depending on the relative humidity at ground in H.E.S.S. I data.

C.2 H.E.S.S. II four telescope data set

Plots for the H.E.S.S. II four telescope data set. All plots show one of the studied parameters on the abscissa and $\frac{\text{BG rate}_{\text{measured}}}{\text{BG rate}_{\text{expected}}}$ on the ordinate.

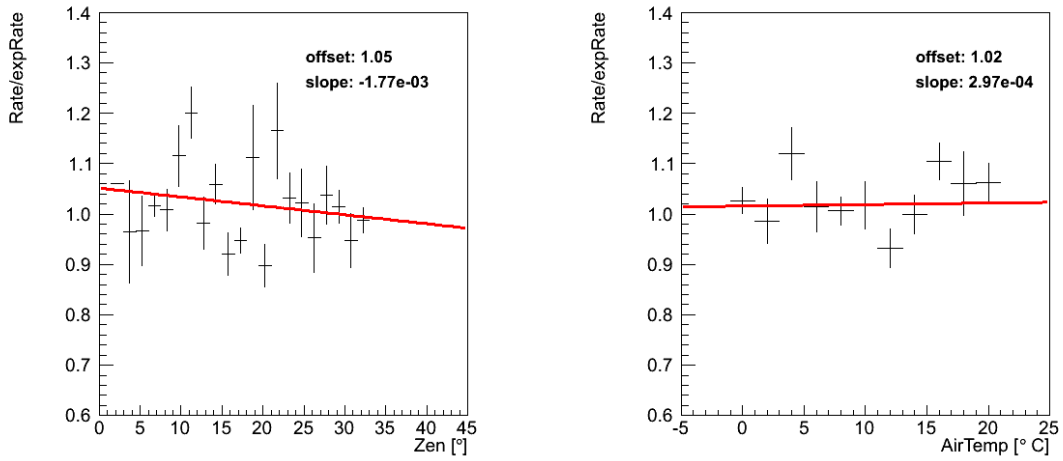

Figure C.6: Left: $\frac{\text{BG rate}_{\text{measured}}}{\text{BG rate}_{\text{expected}}}$ depending on the zenith angle in H.E.S.S. II four telescope data. Right: $\frac{\text{BG rate}_{\text{measured}}}{\text{BG rate}_{\text{expected}}}$ depending on the air temperature at ground in H.E.S.S. II four telescope data.

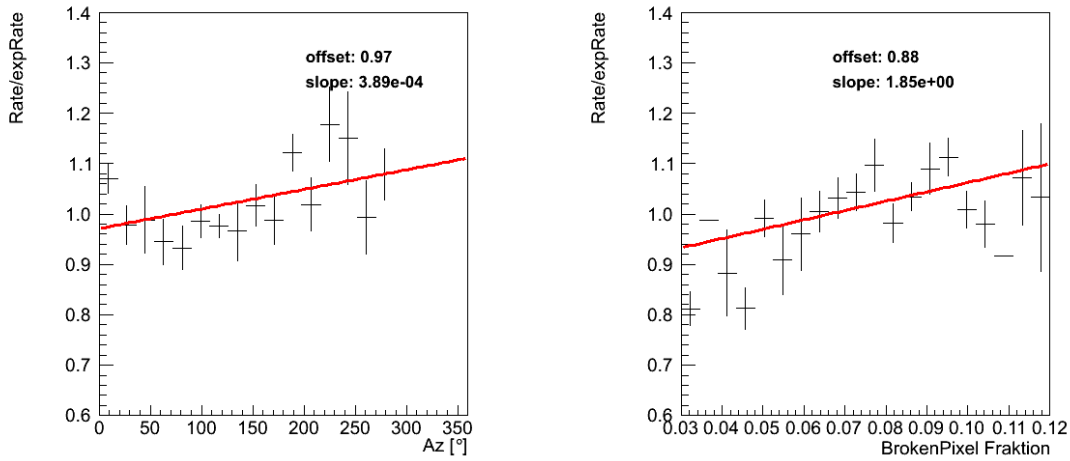

Figure C.7: Left: $\frac{\text{BG rate}_{\text{measured}}}{\text{BG rate}_{\text{expected}}}$ depending on the azimuth angle in H.E.S.S. II four telescope data. Right: $\frac{\text{BG rate}_{\text{measured}}}{\text{BG rate}_{\text{expected}}}$ depending on the averaged broken pixel fraction in CT1-CT5 in H.E.S.S. II four telescope data.

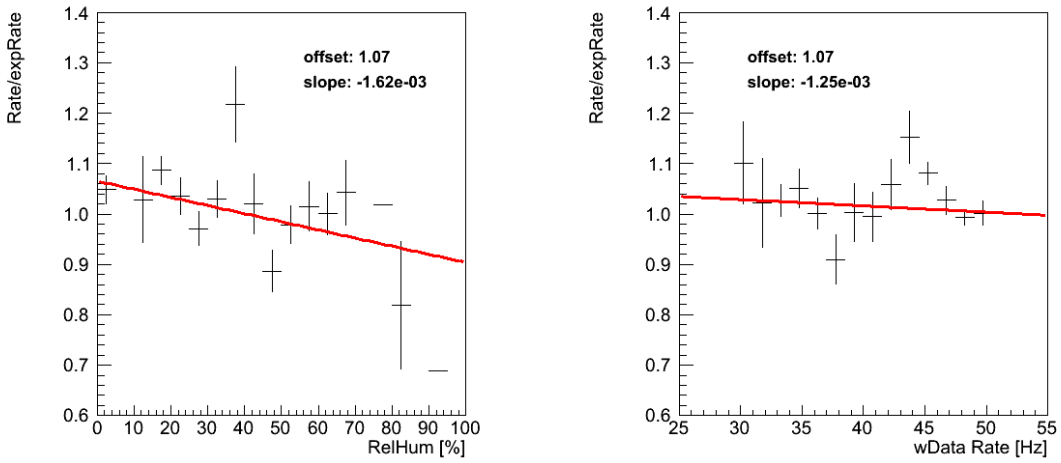

Figure C.8: Left: $\frac{\text{BG rate}_{\text{measured}}}{\text{BG rate}_{\text{expected}}}$ depending on the relative humidity in H.E.S.S. II four telescope data. Right: $\frac{\text{BG rate}_{\text{measured}}}{\text{BG rate}_{\text{expected}}}$ depending on the average broken pixel fraction in CT1-CT5 in H.E.S.S. II data.

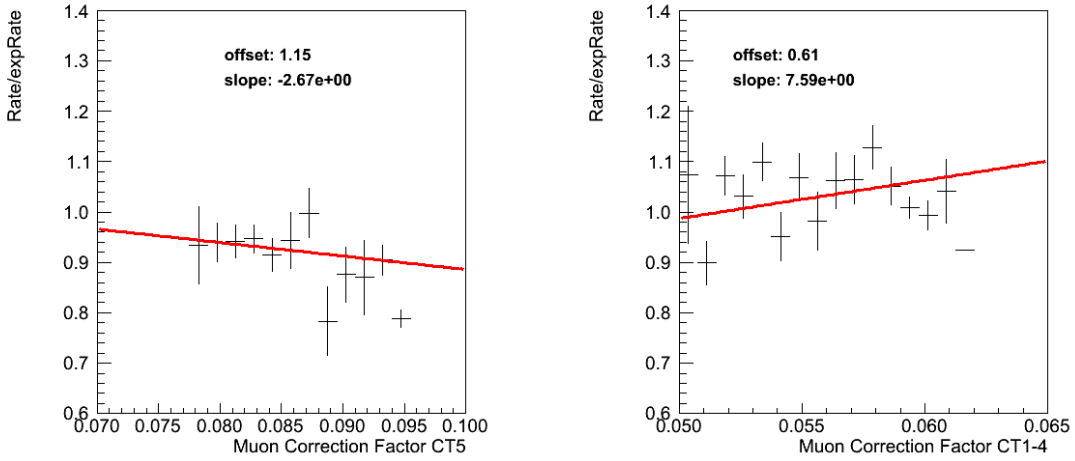

Figure C.9: Left: $\frac{\text{BG rate}_{\text{measured}}}{\text{BG rate}_{\text{expected}}}$ depending on the muon efficiency factor in CT5 for H.E.S.S. II four telescope data. Right: $\frac{\text{BG rate}_{\text{measured}}}{\text{BG rate}_{\text{expected}}}$ depending on the averaged muon efficiency factor CT1-CT4 for H.E.S.S. II four telescope data.

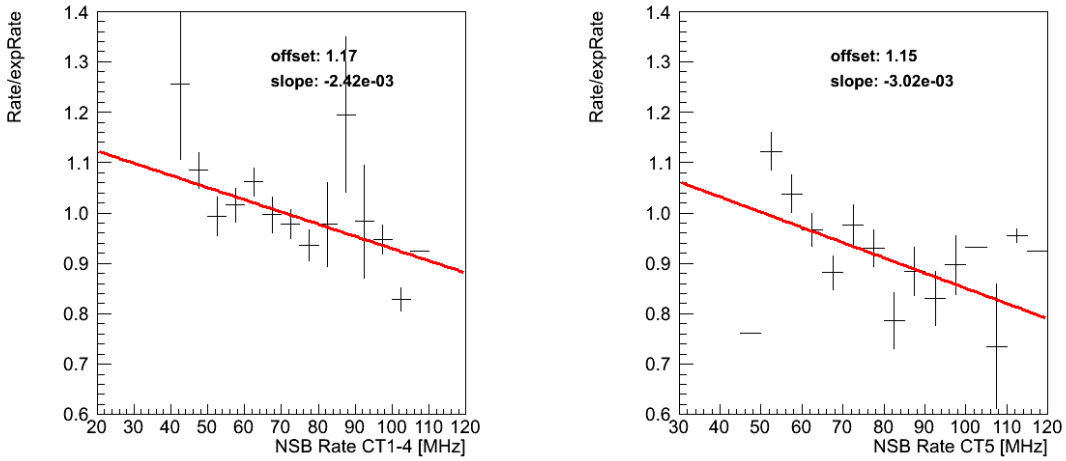

Figure C.10: Left: $\frac{\text{BG rate}_{\text{measured}}}{\text{BG rate}_{\text{expected}}}$ depending on the averaged NSB rate in CT1-CT4 in H.E.S.S. II four telescope data. Right: $\frac{\text{BG rate}_{\text{measured}}}{\text{BG rate}_{\text{expected}}}$ depending on the NSB rate in CT5 in H.E.S.S. II four telescope data.

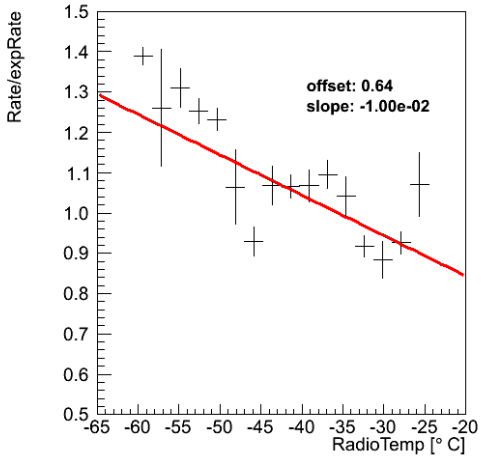

Figure C.11: $\frac{\text{BG rate}_{\text{measured}}}{\text{BG rate}_{\text{expected}}}$ depending on the averaged radiometer temperature in CT1-CT5 for H.E.S.S. II four telescope data.

C.3 H.E.S.S. II five telescope data set

Plots for the H.E.S.S. II five telescope data set. The slope of the line fit is the weighting coefficient for the pairing function used to find On-Off run pairs.

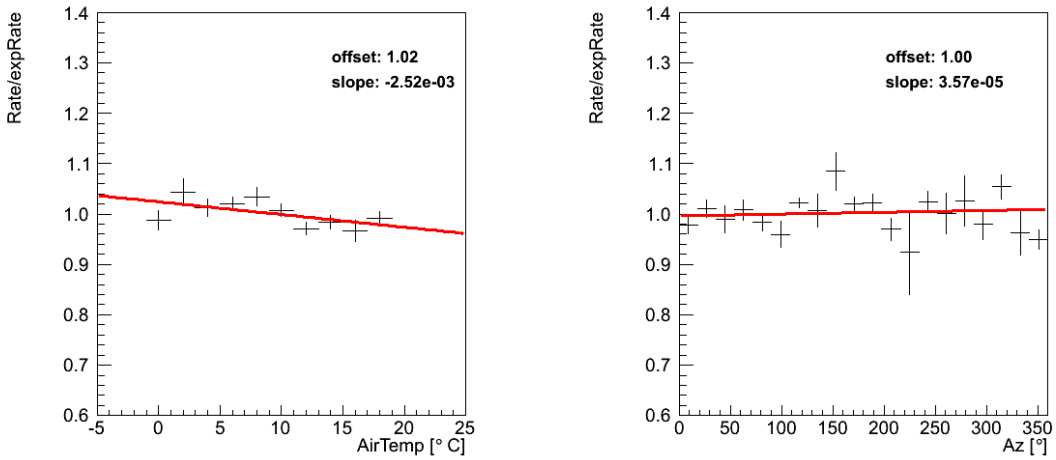

Figure C.12: Left: $\frac{\text{BG rate}_{\text{measured}}}{\text{BG rate}_{\text{expected}}}$ depending on the air temperature at ground in H.E.S.S. II five telescope data. Right: $\frac{\text{BG rate}_{\text{measured}}}{\text{BG rate}_{\text{expected}}}$ depending on azimuth angle in H.E.S.S. II five telescope data.

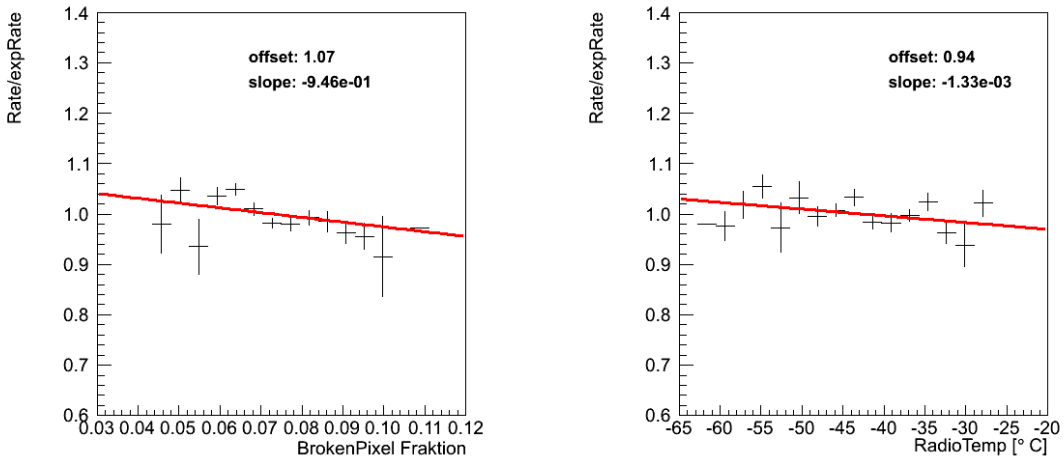

Figure C.13: Left: $\frac{\text{BG rate}_{\text{measured}}}{\text{BG rate}_{\text{expected}}}$ depending on the averaged broken pixel fraction in CT1-CT5 in H.E.S.S. II five telescope data. Right: $\frac{\text{BG rate}_{\text{measured}}}{\text{BG rate}_{\text{expected}}}$ depending on the average radiometer temperature in CT1-CT5 in H.E.S.S. II five telescope data.

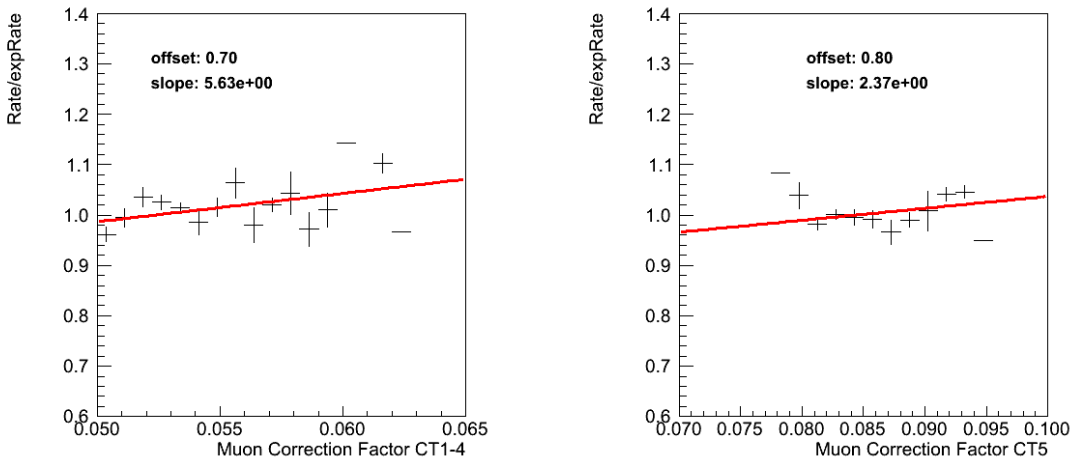

Figure C.14: Left: $\frac{\text{BG rate}_{\text{measured}}}{\text{BG rate}_{\text{expected}}}$ depending on the average muon efficiency in CT1-CT4 in H.E.S.S. II five telescope data. Right: $\frac{\text{BG rate}_{\text{measured}}}{\text{BG rate}_{\text{expected}}}$ depending on the muon efficiency in CT5 in H.E.S.S. II five telescope data.

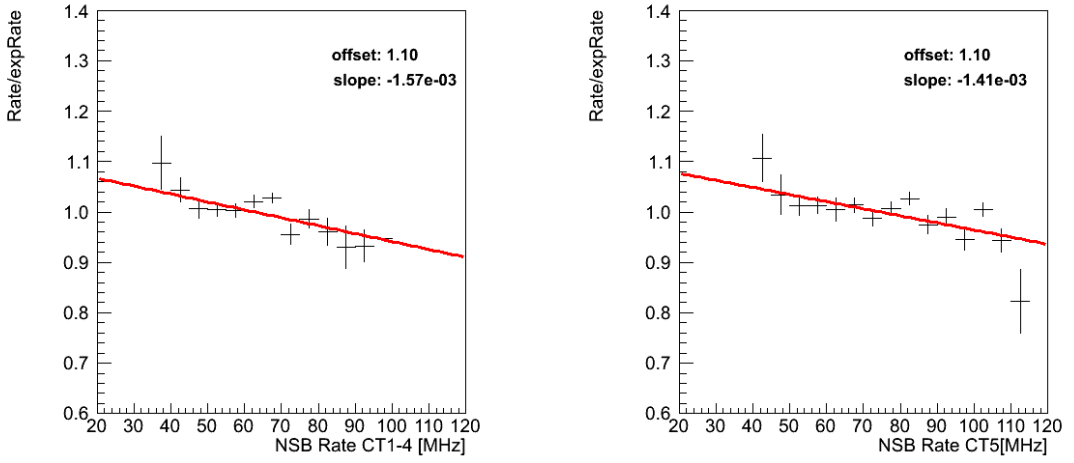

Figure C.15: Left: $\frac{\text{BG rate}_{\text{measured}}}{\text{BG rate}_{\text{expected}}}$ depending on the averaged NSB rate in CT1-CT4 in H.E.S.S. II five telescope data. Right: $\frac{\text{BG rate}_{\text{measured}}}{\text{BG rate}_{\text{expected}}}$ depending on the NSB rate in CT5 in H.E.S.S. II five telescope data.

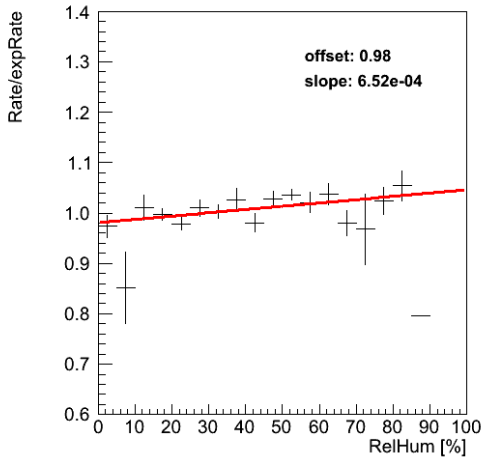

Figure C.16: $\frac{\text{BG rate}_{\text{measured}}}{\text{BG rate}_{\text{expected}}}$ depending on the relative humidity at ground in H.E.S.S. II five telescope data.

Appendix D

Results

D.1 Galactic Centre run lists

Table D.1: Galactic Centre run lists H.E.S.S. I. All runs have the telescope pattern 30.

On	Off	On	Off	On	Off
32666	43372	33458	33003	31579	38277
33467	35942	34949	32493	34951	32466
38863	38480	38865	32978	38932	32459
45472	56670	45491	32463	45493	32486
32695	32517	45378	44505	47030	45977
47031	45928	47064	32465	47066	32458
50653	48333	50682	45953	50683	45998
50654	51317	58887	33006	34310	33005
33137	32979	57804	32519	58751	32980
41036	32343	34209	68518	40801	32368
63745	30906	63755	63711	74253	35935
74371	68855	74377	68484	31106	38259
31383	38169	31425	58200	32586	42817
33135	36067	33136	36068	33138	36017
33536	33004	58860	32977	38960	32959
34187	38675	34188	58424	34313	32976
34314	32405	34950	32440	34976	33114
34977	32515	35001	32973	38832	38225
38959	32464	74384	35932	67161	33002
40743	49033	40744	49031	40745	40254
40759	35556	40826	32399	40827	32438
57805	32518	58829	32488	40851	45054
40878	49009	40881	45464	40909	45247
40940	49762	40942	48204	40972	45056
41004	52025	41073	42918	41074	48352
45381	70445	47027	46158	47033	45246
50680	46454	50681	44755	58728	33008
58802	32925	58805	33172	58911	33009
58912	32492	58913	58226	58933	35933
74247	68486	74382	68485	58934	35894
58935	68517	66784	68487	67094	35892
66785	31753	66786	31760	67114	35940
67162	32974	67215	32975		

Table D.2: Galactic Centre run lists H.E.S.S. II. For all runs the analysed telescope pattern is given in the list.

On		Off		On		Off	
95357	62	95743	62	95401	62	95147	62
96359	62	96229	62	96486	60	95776	46
96494	62	95145	62	95399	62	95193	62
96395	62	95239	62	96598	62	95194	62
96357	62	96228	62	96529	62	105860	62
96599	62	98636	62	97200	62	109205	62
97201	62	109206	62	97202	62	109208	62
96597	62	109152	62	97341	62	95745	62
96490	62	95744	62	97166	62	95496	62
106181	58	95625	46	106183	58	95627	46
106184	58	95777	46	106359	62	109204	62
97199	62	108965	62	107641	62	95294	62
109700	60	101452	58	109758	60	101453	58
109759	60	105818	58	109435	60	107531	46
109761	60	108737	58	109861	60	101481	58
106413	54	97351	58	106412	54	95774	46
110973	60	101296	58	111077	60	95631	46
95356	62	95148	62	95994	62	95293	62
96150	46	95630	46	97065	58	95779	46
96487	60	95551	46	110974	60	97131	54
96151	62	95832	62	96152	62	95833	62
96392	62	98216	62	96390	62	95324	62
96391	62	95197	62	97165	62	95150	62
97476	62	108891	62	97477	62	109151	62
97498	62	108650	62	97501	62	109036	62
106182	58	95547	46	106353	62	107488	62
106356	62	95149	62	106358	62	95198	62
106414	54	95626	46	109461	60	109670	60
109462	60	113245	60	109464	60	108738	58
109465	60	108708	54	109466	60	110243	60
109619	60	95624	46	109620	60	96687	60
109621	60	109668	60	109622	60	105855	58
109623	60	111085	60	111026	60	101073	58
109624	60	109671	60	109625	60	109672	60
109628	60	109217	58	110519	60	109669	60
110521	60	110997	60	110654	60	101323	58
110656	60	111086	60	111196	60	109770	60
111199	60	108739	58	111200	60	109828	60
111201	60	107480	60	111204	60	108712	54

D.2 Cross section limits

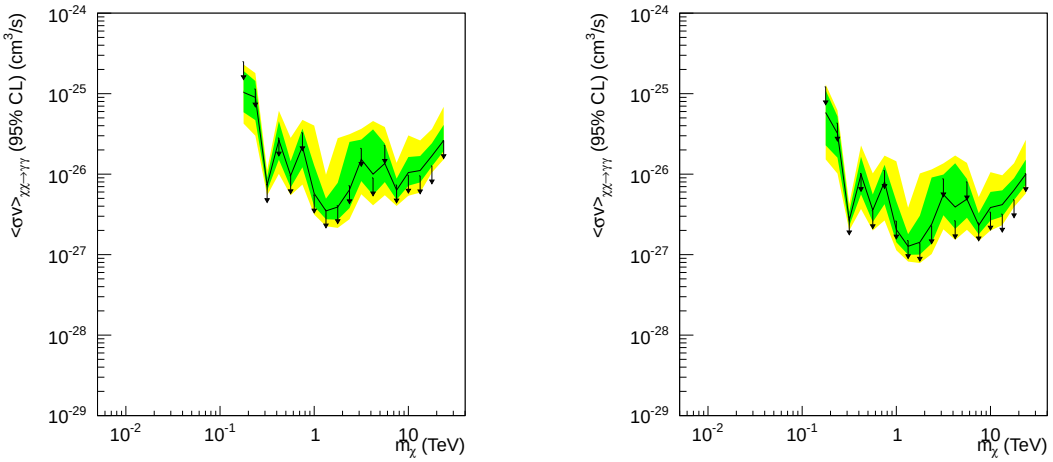

Figure D.1: Upper limits on the velocity-weighted annihilation cross section assuming a NFW shaped Dark Matter halo profile for the Combined data set. Shown are measured limits (black arrows), expected limits (black line), 68 % containment interval (green) and 95 % containment interval (yellow). The result for the Cored profile is shown on the left and for the Cusped on the right.

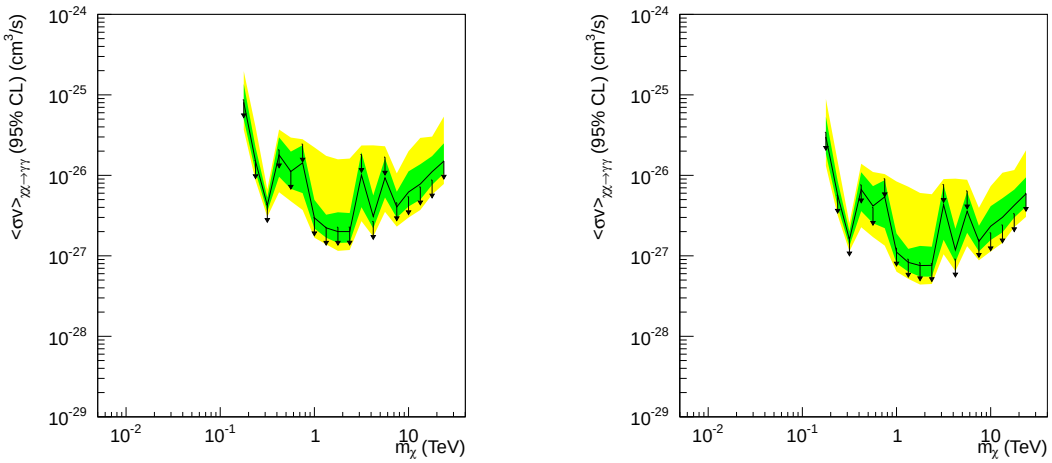

Figure D.2: Upper limits on the velocity-weighted annihilation cross section assuming an Einasto shaped Dark Matter halo profile for H.E.S.S. I data. Shown are measured limits (black arrows), expected limits (black line), 68 % containment interval (green) and 95 % containment interval (yellow). The result for the Cored profile is shown on the left and for the Cusped on the right.

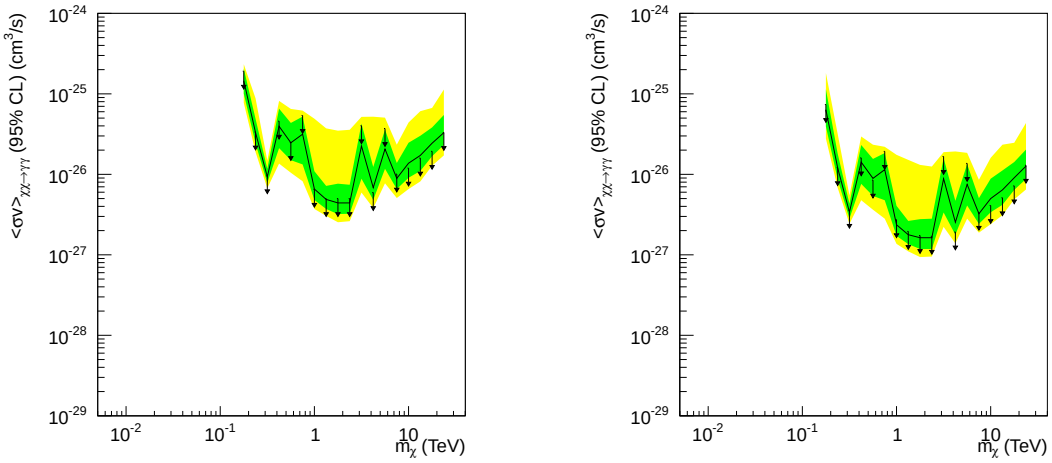

Figure D.3: Upper limits on the velocity-weighted annihilation cross section assuming a NFW shaped Dark Matter halo profile for H.E.S.S. I data. Shown are measured limits (black arrows), expected limits (black line), 68 % containment interval (green) and 95 % containment interval (yellow). The result for the Cored profile is shown on the left and for the Cusped on the right.

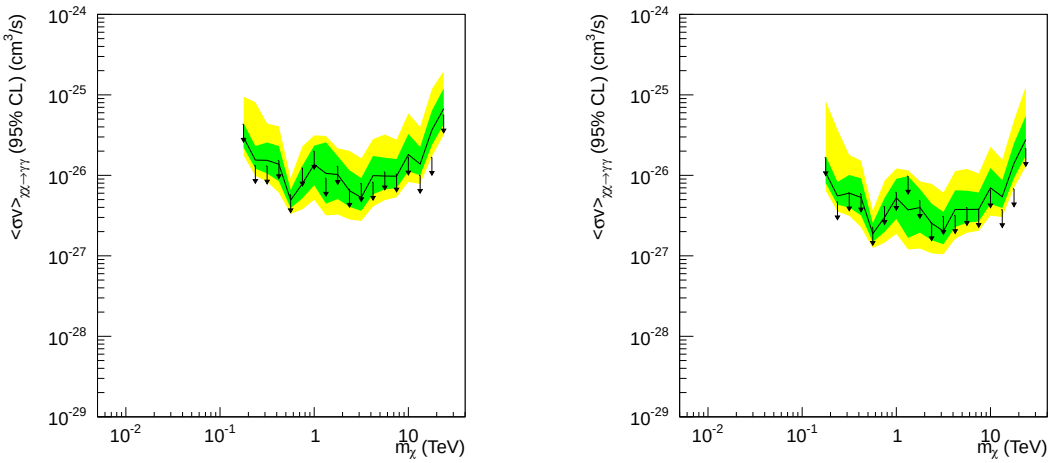

Figure D.4: Upper limits on the velocity-weighted annihilation cross section assuming an Einasto shaped Dark Matter halo profile for H.E.S.S. II data. Shown are measured limits (black arrows), expected limits (black line), 68 % containment interval (green) and 95 % containment interval (yellow). The result for the Cored profile is shown on the left and for the Cusped on the right.

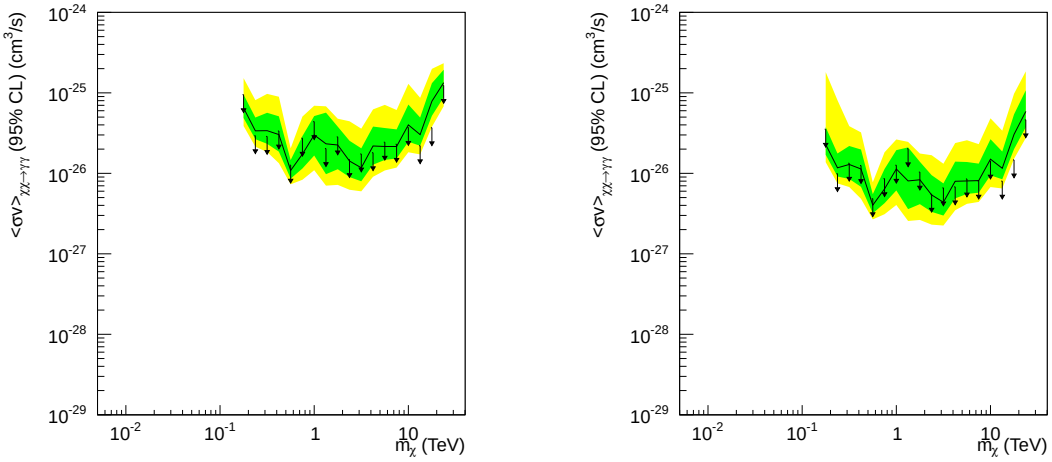

Figure D.5: Upper limits on the velocity-weighted annihilation cross section assuming a NFW shaped Dark Matter halo profile for H.E.S.S. II data. Shown are measured limits (black arrows), expected limits (black line), 68 % containment interval (green) and 95 % containment interval (yellow). The result for the Cored profile is shown on the left and for the Cusped on the right.

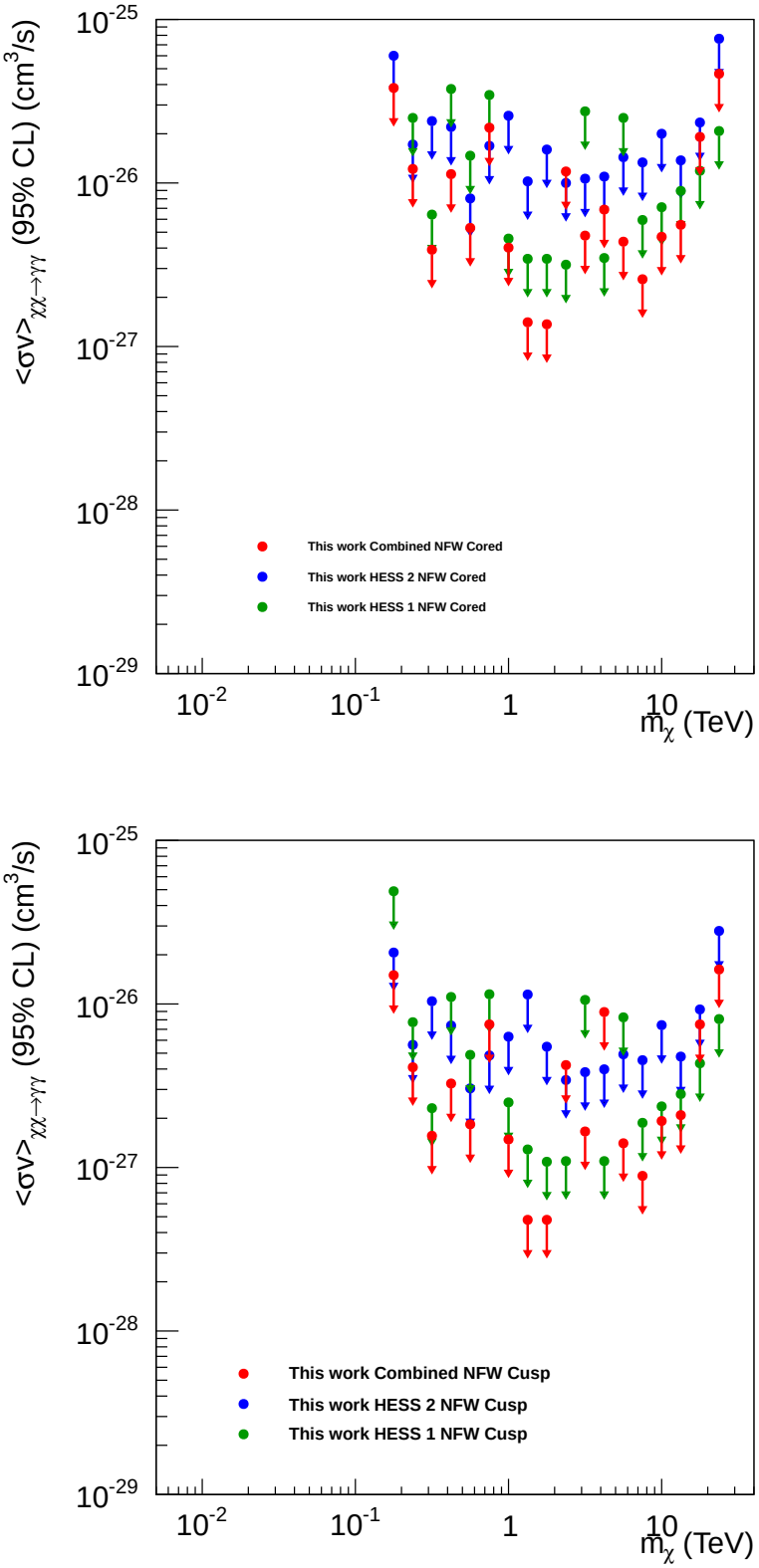

Figure D.6: Upper limits on the velocity-weighted annihilation cross section assuming a NFW shaped Dark Matter halo profile for all three data sets. The result for the Cored profile is shown at the top and for the Cusped at the bottom.

Bibliography

Aad, G., Abbott, B., Abdallah, J., et al. (2016). *Measurements of the Higgs boson production and decay rates and constraints on its couplings from a combined ATLAS and CMS analysis of the LHC pp collision data at $\sqrt{s} = 7$ and 8 TeV*. In: *Journal of High Energy Physics*, 8, 45. DOI: 10.1007/JHEP08(2016)045. arXiv: 1606.02266.

Aartsen, M. G., Abraham, K., Ackermann, M., et al. (2016). *All-flavour search for neutrinos from dark matter annihilations in the Milky Way with IceCube/DeepCore*. In: *European Physical Journal C*, 76, 531. DOI: 10.1140/epjc/s10052-016-4375-3. arXiv: 1606.00209.

Abbott, B. P., Abbott, R., Abbott, T. D., et al. (2017). *A gravitational-wave standard siren measurement of the Hubble constant*. In: *Nature*, 551, pp. 85–88. DOI: 10.1038/nature24471. arXiv: 1710.05835.

Abdalla, H., Abramowski, A., Aharonian, F., Ait Benkhali, F., Akhperjanian, A. G. & al., et (2016a). *H.E.S.S. Limits on Linelike Dark Matter Signatures in the 100 GeV to 2 TeV Energy Range Close to the Galactic Center*. In: *Physical Review Letters*, 117 (15), 151302. DOI: 10.1103/PhysRevLett.117.151302. arXiv: 1609.08091.

Abdalla, H., Abramowski, A., Aharonian, F., Ait Benkhali, F., Akhperjanian, A. G. & al., et (2016b). *Search for Dark Matter Annihilations towards the Inner Galactic Halo from 10 Years of Observations with H.E.S.S.* In: *Physical Review Letters*, 117 (11), 111301. DOI: 10.1103/PhysRevLett.117.111301. arXiv: 1607.08142.

Abdalla, H., Abramowski, A., Aharonian, F., Ait Benkhali, F., Akhperjanian, A. G., Andersson, T., Angüner, E. O. & al., et (2017a). *Characterising the VHE diffuse emission in the central 200 parsecs of our Galaxy with H.E.S.S.* arXiv: 1706.04535.

Abdalla, H., Abramowski, A., Aharonian, F., Ait Benkhali, F., Akhperjanian, A. G., Andersson, T., Angüner, E. O. & al., et (2017b). *Gamma-ray blazar spectra with H.E.S.S. II mono analysis: The case of PKS 2155-304 and PG 1553+113*. In: *Astronomy & Astrophysics*, 600, A89. DOI: 10.1051/0004-6361/201629427. arXiv: 1612.01843.

Abdalla, H., Abramowski, A., Aharonian, F., et al. (in preparation). *Performance of the H.E.S.S. II array of Imaging Atmospheric Cherenkov Telescopes*.

Abramowski, A., Acero, F., Aharonian, F., et al. (2011). *Search for a Dark Matter Annihilation Signal from the Galactic Center Halo with H.E.S.S.* In: *Physical Review Letters*, 106 (16), 161301. DOI: 10.1103/PhysRevLett.106.161301. arXiv: 1103.3266.

Abramowski, A., Acero, F., Aharonian, F., et al. (2013). *Search for Photon-Linelike Signatures from Dark Matter Annihilations with H.E.S.S.* In: *Physical Review Letters*, 110 (4), 041301. DOI: 10.1103/PhysRevLett.110.041301. arXiv: 1301.1173.

Abramowski, A., Aharonian, F., Ait Benkhali, F., et al. (2014). *Search for dark matter annihilation signatures in H.E.S.S. observations of dwarf spheroidal galaxies*. In: *Phys. Rev. D*, 90 (11), 112012. DOI: 10.1103/PhysRevD.90.112012. arXiv: 1410.2589.

Abramowski, A., Aharonian, F., Ait Benkhali, F., et al. (2015). *Constraints on an Annihilation Signal from a Core of Constant Dark Matter Density around the Milky Way Center with H.E.S.S.* In: *Physical Review Letters*, 114 (8), 081301. DOI: 10.1103/PhysRevLett.114.081301. arXiv: 1502.03244.

Abramowski, A., Aharonian, F., Benkhali, F. A., Akhperjanian, A. G. & al., et (2016). *Acceleration of petaelectronvolt protons in the Galactic Centre*. In: *Nature*, 531, pp. 476–479. DOI: 10.1038/nature17147. arXiv: 1603.07730.

Ackermann, M., Ajello, M., Albert, A., et al. (2015). *Updated search for spectral lines from Galactic dark matter interactions with pass 8 data from the Fermi Large Area Telescope*. In: *Physical Review D*, 91 (12), 122002. DOI: 10.1103/PhysRevD.91.122002. arXiv: 1506.00013.

Ackermann, M., Albert, A., Anderson, B., et al. (2015). *Searching for Dark Matter Annihilation from Milky Way Dwarf Spheroidal Galaxies with Six Years of Fermi Large Area Telescope Data*. In: *Physical Review Letters*, 115 (23), 231301. DOI: 10.1103/PhysRevLett.115.231301. arXiv: 1503.02641.

Adhikari, R., Agostini, M., Ky, N. A., et al. (2017). *A White Paper on keV sterile neutrino Dark Matter*. In: *JCAP*, 1, 025. DOI: 10.1088/1475-7516/2017/01/025. arXiv: 1602.04816.

Aharonian, F., Akhperjanian, A. G., Aye, K.-M., et al. (2004). *Very high energy gamma rays from the direction of Sagittarius A**. In: *Astronomy & Astrophysics*, 425, pp. L13–L17. DOI: 10.1051/0004-6361:200400055. arXiv: astro-ph/0406658.

Aharonian, F., Akhperjanian, A. G., Aye, K.-M., et al. (2005). *H.E.S.S. observations of PKS 2155-304*. In: *Astronomy & Astrophysics*, 430, pp. 865–875. DOI: 10.1051/0004-6361:20041853. arXiv: astro-ph/0411582.

Aharonian, F., Akhperjanian, A. G., Bazer-Bachi, A. R., et al. (2006a). *Discovery of very-high-energy γ-rays from the Galactic Centre ridge*. In: *Nature*, 439, pp. 695–698. DOI: 10.1038/nature04467. arXiv: astro-ph/0603021.

Aharonian, F., Akhperjanian, A. G., Bazer-Bachi, A. R., et al. (2006b). *Observations of the Crab nebula with HESS*. In: *Astronomy & Astrophysics*, 457, pp. 899–915. DOI: 10.1051/0004-6361:20065351. arXiv: astro-ph/0607333.

Aharonian, F., Akhperjanian, A. G., Bazer-Bachi, A. R., et al. (2006c). *The H.E.S.S. Survey of the Inner Galaxy in Very High Energy Gamma Rays*. In: *Astrophys. J.* 636, pp. 777–797. DOI: 10.1086/498013. eprint: astro-ph/0510397.

Albert, A., André, M., Anghinolfi, M., et al. (2017a). *Results from the search for dark matter in the Milky Way with 9 years of data of the ANTARES neutrino telescope*. In: *Physics Letters B*, 769, pp. 249–254. DOI: 10.1016/j.physletb.2017.03.063. arXiv: 1612.04595.

Albert, A., André, M., Anghinolfi, M., et al. (2017b). *Search for dark matter annihilation in the earth using the ANTARES neutrino telescope*. In: *Physics of the Dark Universe*, 16, pp. 41–48. DOI: 10.1016/j.dark.2017.04.005.

Aleksić, J., Ansoldi, S., Antonelli, L. A., et al. (2014). *Optimized dark matter searches in deep observations of Segue 1 with MAGIC*. In: *JCAP*, 2, 008. DOI: 10.1088/1475-7516/2014/02/008. arXiv: 1312.1535.

Aprile, E., Arisaka, K., Arneodo, F., et al. (2011). *Dark Matter Results from 100 Live Days of XENON100 Data*. In: *Physical Review Letters*, 107 (13), 131302. DOI: 10.1103/PhysRevLett.107.131302. arXiv: 1104.2549.

Bekenstein, J. & Milgrom, M. (1984). *Does the missing mass problem signal the breakdown of Newtonian gravity?* In: *Astrophys. J.* 286, pp. 7–14. DOI: 10.1086/162570.

Berge, D., Funk, S. & Hinton, J. (2007). *Background modelling in very-high-energy γ-ray astronomy*. In: *Astronomy & Astrophysics*, 466, pp. 1219–1229. DOI: 10.1051/0004-6361:20066674. arXiv: astro-ph/0610959.

Bertone, G. & Hooper, D. (2016). *A History of Dark Matter*. arXiv: 1605.04909.

Bringmann, T., Bergström, L. & Edsjö, J. (2008). *New gamma-ray contributions to supersymmetric dark matter annihilation*. In: *Journal of High Energy Physics*, 1, 049. DOI: 10.1088/1126-6708/2008/01/049. arXiv: 0710.3169.

Catena, R. & Ullio, P. (2010). *A novel determination of the local dark matter density*. In: *JCAP*, 8, 004. DOI: 10.1088/1475-7516/2010/08/004. arXiv: 0907.0018.

Čerenkov, P. A. (1937). *Visible Radiation Produced by Electrons Moving in a Medium with Velocities Exceeding that of Light*. In: *Physical Review*, 52, pp. 378–379. DOI: 10.1103/PhysRev.52.378.

Cirelli, M., Corcella, G., Hektor, A., et al. (2011). *PPPC 4 DM ID: a poor particle physicist cookbook for dark matter indirect detection*. In: *JCAP*, 3, 051. DOI: 10.1088/1475-7516/2011/03/051. arXiv: 1012.4515.

Clowe, D., Bradač, M., Gonzalez, A. H., Markevitch, M., Randall, S. W., Jones, C. & Zaritsky, D. (2006). *A Direct Empirical Proof of the Existence of Dark Matter*. In: *Astrophys. J., Lett.* 648, pp. L109–L113. DOI: 10.1086/508162. arXiv: astro-ph/0608407.

Conrad, J. M. & Shaevitz, M. H. (2016). *Sterile Neutrinos: An Introduction to Experiments*. arXiv: 1609.07803.

Corley, S. & Lowe, D. A. (2001). *Solving the hierarchy problem with brane crystals*. In: *Physics Letters B*, 505, pp. 197–205. DOI: 10.1016/S0370-2693(01)00344-6. eprint: hep-ph/0101021.

CTA Consortium (2017). *Cherenkov Telescope Array: The Next Generation Gamma-ray Observatory*. arXiv: 1709.05434.

CTA Consortium, : Acharya, B. S., et al. (2017). *Science with the Cherenkov Telescope Array*. arXiv: 1709.07997.

Davis, J. H. (2014). *Fitting the Annual Modulation in DAMA with Neutrons from Muons and Neutrinos*. In: *Physical Review Letters*, 113 (8), 081302. DOI: 10.1103/PhysRevLett.113.081302. arXiv: 1407.1052.

Diemand, J., Kuhlen, M., Madau, P., Zemp, M., Moore, B., Potter, D. & Stadel, J. (2008). *Clumps and streams in the local dark matter distribution*. In: *Nature*, 454, pp. 735–738. DOI: 10.1038/nature07153. arXiv: 0805.1244.

Edsjö, J. (2014). *Darkmatter particle physics*. Presented at: *HAP Workshop on data analysis for indirect dark matter searches*.

Einasto, J. (1965). *On the Construction of a Composite Model for the Galaxy and on the Determination of the System of Galactic Parameters*. In: *Trudy Astrofizicheskogo Instituta Alma-Ata*, 5, pp. 87–100.

Einstein, A. (1915). *Die Feldgleichungen der Gravitation*. In: *Sitzungsberichte der Königlich Preußischen Akademie der Wissenschaften (Berlin)*. http://adsabs.harvard.edu/abs/1915SPAW.....844E, pp. 844–847.

Einstein, A. (1936). *Lens-Like Action of a Star by the Deviation of Light in the Gravitational Field*. In: *Science*, 84, pp. 506–507. DOI: 10.1126/science.84.2188.506.

El Aisati, C., Gustafsson, M., Hambye, T. & Scarna, T. (2016). *Dark matter decay to a photon and a neutrino: The double monochromatic smoking gun scenario*. In: *Phys. Rev. D*, 93 (4), 043535. DOI: 10.1103/PhysRevD.93.043535. arXiv: 1510.05008.

Famaey, B. & McGaugh, S. S. (2012). *Modified Newtonian Dynamics (MOND): Observational Phenomenology and Relativistic Extensions*. In: *Living Reviews in Relativity*, 15, 10. DOI: 10.12942/lrr-2012-10. arXiv: 1112.3960.

Finzi, A. (1963). *On the validity of Newton's law at a long distance*. In: *MNRAS*, 127, p. 21. DOI: 10.1093/mnras/127.1.21.

Fixsen, D. J. (2009). *The Temperature of the Cosmic Microwave Background*. In: *Astrophys. J.* 707, pp. 916–920. DOI: 10.1088/0004-637X/707/2/916. arXiv: 0911.1955.

Funk, S., Hinton, J., Hermann, G., et al. (2005). *The Central Trigger System of the H.E.S.S. Telescope Array*. In: *High Energy Gamma-Ray Astronomy*. Vol. 745, pp. 753–757. DOI: 10.1063/1.1878496.

Funk, S. (2005). *A new population of very high-energy γ-ray sources detected with H.E.S.S. in the inner part of the Milky Way*. PhD thesis.

Giavitto, G., Ashton, T., Balzer, A., et al. (2015). *A major electronics upgrade for the H.E.S.S. Cherenkov telescopes 1-4*. In: *34th International Cosmic Ray Conference (ICRC2015)*. Vol. 34. arXiv: 1509.01232.

Gillessen, S. (2004). *Sub-Bogenminuten-genaue Positionen von TeV-Quellen mit H.E.S.S.* PhD thesis. Ruprecht-Karls-Universität Heidelberg. DOI: 10.11588/heidok.00004754.

Glück, B. (2011). *A Detailed Study of the Pulsar Wind Nebula HESS J0835–455 (Vela X) in TeV γ-Rays*. PhD thesis. Friedrich-Alexander-Universität Erlangen-Nürnberg. URL: http://opus4.kobv.de/opus4-fau/files/1647/BernhardGlueckDissertation.pdf.

Governato, F., Zolotov, A., Pontzen, A., et al. (2012). *Cuspy no more: how outflows affect the central dark matter and baryon distribution in Λ cold dark matter galaxies*. In: *MNRAS*, 422, pp. 1231–1240. DOI: 10.1111/j.1365-2966.2012.20696.x. arXiv: 1202.0554.

Hahn, J., de los Reyes, R., Bernlöhr, K., et al. (2014). *Impact of aerosols and adverse atmospheric conditions on the data quality for spectral analysis of the H.E.S.S. telescopes*. In: *Astroparticle Physics*, 54, pp. 25–32. DOI: 10.1016/j.astropartphys.2013.10.003. arXiv: 1310.1639.

Hahn, J., Gast, H., de los Reyes, R., Deil, C., Bernlöhr, K., Kosack, K., Marandon, V. & P., H. (2013). *Heidelberg Data Quality Selection*. In: *H.E.S.S. internal note*.

Hegyi, D. J. & Olive, K. A. (1983). *Can galactic halos be made of baryons?* In: *Physics Letters B*, 126, pp. 28–32. DOI: 10.1016/0370-2693(83)90009-6.

Heitler, W. (1954). *Quantum theory of radiation*.

H.E.S.S. Collaboration (2017). *H.E.S.S. Website*. http://www.mpi-hd.mpg.de/hfm/HESS/.

Hess, V. F. (1912). *Über Beobachtungen der durchdringenden Strahlung bei sieben Freiballonfahrten*. In: *Physikalische Zeitschrift*, 13, pp. 1084–1091.

Hillas, A. M. (1985). *Cerenkov light images of EAS produced by primary gamma*. In: *International Cosmic Ray Conference*, 3.

Hoecker, A., Speckmayer, P., Stelzer, J., et al. (2007). *TMVA - Toolkit for Multivariate Data Analysis*. In: *ArXiv Physics e-prints*. arXiv: physics/0703039.

Hofmann, W. & H.E.S.S. Collaboration (2001). *Status of the H.E.S.S. project*. In: *International Cosmic Ray Conference*, 7, p. 2785.

Holler, M. (2014). *Photon Reconstruction for the H.E.S.S. 28 m Telescope and Analysis of Crab Nebula and Galactic Centre Observations*. PhD thesis. Universität Potsdam. URL: http://opus.kobv.de/ubp/volltexte/2014/7209/.

Hooper, D. & Profumo, S. (2007). *Dark matter and collider phenomenology of universal extra dimensions*. In: *Phys. Rep.* 453, pp. 29–115. DOI: 10.1016/j.physrep.2007.09.003. eprint: hep-ph/0701197.

Hubble, E. (1929). *A Relation between Distance and Radial Velocity among Extra-Galactic Nebulae*. In: *Proceedings of the National Academy of Science*, 15, pp. 168–173. DOI: 10.1073/pnas.15.3.168.

Ishigure, Y., Kakizaki, M. & Santa, A. (2016). *Thermal relic abundance of the lightest Kaluza-Klein particle in phenomenological universal extra dimension models*. arXiv: 1611.06760.

Jahn, C. V. (2013). *Systematic Studies of an On-Off-Analysis of H.E.S.S. data in Search for a Signal from the Dark Matter Halo of the Milky Way*. PhD thesis. Friedrich-Alexander-Universität Erlangen-Nürnberg. URL: http://opus4.kobv.de/opus4-fau/files/3750/ConstanzeJahnDissertation.pdf.

Jungman, G., Kamionkowski, M. & Griest, K. (1996). *Supersymmetric dark matter*. 267, pp. 195–373. DOI: 10.1016/0370-1573(95)00058-5. eprint: hep-ph/9506380.

Kahlhoefer, F. (2017). *Review of LHC dark matter searches*. In: *International Journal of Modern Physics A*, 32, 1730006. DOI: 10.1142/S0217751X1730006X. arXiv: 1702.02430.

Kaluza, T. (1921). *Zum Unitätsproblem der Physik*. In: *Sitzungsberichte der Königlich Preußischen Akademie der Wissenschaften (Berlin)*. http://homepage.uibk.ac.at/~c705204/pdf/kaluza-1921.pdf, pp. 966–972.

Kieffer, M. (2015). *Recherche indirecte de matière noire avec l'expérience H.E.S.S.* PhD thesis. Université Pierre et Marie Curie - Paris VI. URL: https://tel.archives-ouvertes.fr/tel-01314129.

Klasen, M., Pohl, M. & Sigl, G. (2015). *Indirect and direct search for dark matter*. In: *Progress in Particle and Nuclear Physics*, 85, pp. 1–32. DOI: 10.1016/j.ppnp.2015.07.001. arXiv: 1507.03800.

Klein, O. (1926). *Quantentheorie und fünfdimensionale Relativitätstheorie*. In: *Zeitschrift fur Physik*, 37, pp. 895–906. DOI: 10.1007/BF01397481.

Knödlseder, J., Mayer, M., Deil, C., et al. (2016). *GammaLib and ctools. A software framework for the analysis of astronomical gamma-ray data*. In: *Astronomy & Astrophysics*, 593, A1. DOI: 10.1051/0004-6361/201628822. arXiv: 1606.00393.

Li, T.-P. & Ma, Y.-Q. (1983). *Analysis methods for results in gamma-ray astronomy*. In: *Astrophys. J.* 272, pp. 317–324. DOI: 10.1086/161295.

Lisanti, M. (2017). *Lectures on Dark Matter Physics*. In: *New Frontiers in Fields and Strings (TASI 2015) - Proceedings of the 2015 Theoretical Advanced Study Institute in Elementary Particle*

Physics. Edited by POLCHINSKI JOSEPH ET AL. Published by World Scientific Publishing Co. Pte. Ltd., 2017. ISBN #9789813149441, pp. 399-446, edited by Polchinski, J. et al., pp. 399–446. DOI: 10.1142/9789813149441_0007. arXiv: 1603.03797.

Lohse, T. (2014). *Dark Matter: Overview*. Presented at: *HAP Workshop on data analysis for indirect dark matter searches*.

Longair, M. S. (2011). *High Energy Astrophysics*. Cambridge, United Kingdom: Cambridge University Press.

Marrodán Undagoitia, T. & Rauch, L. (2016). *Dark matter direct-detection experiments*. In: *Journal of Physics & Nuclear Physics*, 43 (1), 013001. DOI: 10.1088/0954-3899/43/1/013001. arXiv: 1509.08767.

Merle, A. (2017). *keV sterile neutrino Dark Matter*. arXiv: 1702.08430.

Metzger, W. J. (2010). *Statistical methods in data analysis*. Nijmegen: Nijmegen Univ. Fys. Lab.

Mitchell, A. M. W. (2016). *Optical Efficiency Calibration for Inhomogeneous IACT Arrays and a Detailed Study of the Highly Extended Pulsar Wind Nebula HESS J1825−137*. PhD thesis.

Murayama, H. (2000). *Supersymmetry Phenomenology*. In: *Particle Physics*, edited by Senjanović, G. et al., p. 296. arXiv: hep-ph/0002232.

de Naurois, M. (2012). *Very High Energy astronomy from H.E.S.S. to CTA. Opening of a new astronomical window on the non-thermal Universe*. URL: https://tel.archives-ouvertes.fr/tel-00687872.

de Naurois, M. & Rolland, L. (2009). *A high performance likelihood reconstruction of γ-rays for imaging atmospheric Cherenkov telescopes*. In: *Astroparticle Physics*, 32, pp. 231–252. DOI: 10.1016/j.astropartphys.2009.09.001. arXiv: 0907.2610.

Navarro, J. F., Frenk, C. S. & White, S. D. M. (1996). *The Structure of Cold Dark Matter Halos*. In: *Astrophys. J.* 462, p. 563. DOI: 10.1086/177173. arXiv: astro-ph/9508025.

Ohm, S., van Eldik, C. & Egberts, K. (2009). *γ/hadron separation in very-high-energy γ-ray astronomy using a multivariate analysis method*. In: *Astroparticle Physics*, 31, pp. 383–391. DOI: 10.1016/j.astropartphys.2009.04.001. arXiv: 0904.1136.

Olive, K. A., Agashe, K., Amsler, C., et al. (2014). *Review of Particle Physics*. In: *Chinese Physics C*, 38 (9), 090001. DOI: 10.1088/1674-1137/38/9/090001.

Parsons, R. D. & Hinton, J. A. (2014). *A Monte Carlo template based analysis for air-Cherenkov arrays*. In: *Astroparticle Physics*, 56, pp. 26–34. DOI: 10.1016/j.astropartphys.2014.03.002. arXiv: 1403.2993.

Peacock, J. A. (1999). *Cosmological Physics*. Cambridge University Press.

Peccei, R. D. & Quinn, H. R. (1977). *Constraints imposed by CP conservation in the presence of pseudoparticles*. In: *Phys. Rev. D*, 16, pp. 1791–1797. DOI: 10.1103/PhysRevD.16.1791.

Planck Collaboration, Ade, P. A. R., Aghanim, N., et al. (2016). *Planck 2015 results. XIII. Cosmological parameters*. In: *Astronomy & Astrophysics*, 594, A13. DOI: 10.1051/0004-6361/201525830. arXiv: 1502.01589.

Pontzen, A. & Governato, F. (2014). *Cold dark matter heats up*. In: *Nature*, 506, pp. 171–178. DOI: 10.1038/nature12953. arXiv: 1402.1764.

Rinchiuso, L., Moulin, E., Viana, A., Van Eldik, C. & Veh J. for the H. E. S. S. collaboration (2017). *Dark matter gamma-ray line searches toward the Galactic Center halo with H.E.S.S. I*. arXiv: 1708.08358.

Rolke, W. A., López, A. M. & Conrad, J. (2005). *Limits and confidence intervals in the presence of nuisance parameters*. In: *Nuclear Instruments and Methods in Physics Research A*, 551, pp. 493–503. DOI: 10.1016/j.nima.2005.05.068. arXiv: physics/0403059.

Römmelt, N. (2015). *Optimierung der Suchstrategie für Dunkle Materie aus dem Galaktischen Zentrum*. Bachelor. Friedrich-Alexander-Universität Erlangen-Nürnberg. URL: https://ecap.nat.fau.de/wp-content/uploads/2017/05/2015_Roemmelt_Bachelor.pdf.

Rubin, V. C., Ford, W. K. J. & Thonnard, N. (1980). *Rotational properties of 21 SC galaxies with a large range of luminosities and radii, from NGC 4605 $R = 4$ kpc to UGC 2885 $R = 122$ kpc*. In: *Astrophys. J.* 238, pp. 471–487. DOI: 10.1086/158003.

Sackett, P. D. & Sparke, L. S. (1990). *The dark halo of the polar-ring galaxy NGC 4650A*. In: *Astrophys. J.* 361, pp. 408–418. DOI: 10.1086/169206.

Scarpa, R. (2006). *Modified Newtonian Dynamics, an Introductory Review*. In: *First Crisis in Cosmology Conference*, edited by Lerner, E. J. et al. Vol. 822, pp. 253–265. DOI: 10.1063/1.2189141. arXiv: astro-ph/0601478.

Schneider, P. (2008). *Extragalaktische Astronomie und Kosmologie*. Springer.

Servant, G. & Tait, T. M. P. (2003). *Is the lightest Kaluza-Klein particle a viable dark matter candidate?* In: *Nuclear Physics B*, 650, pp. 391–419. DOI: 10.1016/S0550-3213(02)01012-X. arXiv: hep-ph/0206071.

Silverwood, H., Weniger, C., Scott, P. & Bertone, G. (2015). *A realistic assessment of the CTA sensitivity to dark matter annihilation*. In: *JCAP*, 3, 055. DOI: 10.1088/1475-7516/2015/03/055. arXiv: 1408.4131.

Spengler, G. C. (2013). *Search for Dark Matter in the Milky Way Halo with the High Energy Stereoscopic System*. PhD thesis. Humboldt-Universität zu Berlin.

Springel, V., White, S. D. M., Frenk, C. S., et al. (2008). *Prospects for detecting supersymmetric dark matter in the Galactic halo*. In: *Nature*, 456, pp. 73–76. DOI: 10.1038/nature07411. arXiv: 0809.0894.

Stern, I. & Experiment, A. (2016). *ADMX Status*. In: *Proceedings of the 38th International Conference on High Energy Physics (ICHEP2016). 3-10 August 2016. Chicago, USA.* arXiv: 1612.08296.

Suzuki, N., Rubin, D., Lidman, C., et al. (2012). *The Hubble Space Telescope Cluster Supernova Survey. V. Improving the Dark-energy Constraints above $z > 1$ and Building an Early-type-hosted Supernova Sample*. In: *Astrophys. J.* 746, 85. DOI: 10.1088/0004-637X/746/1/85. arXiv: 1105.3470.

van Eldik, C. (2015). *Gamma rays from the Galactic Centre region: A review*. In: *Astroparticle Physics*, 71, pp. 45–70. DOI: 10.1016/j.astropartphys.2015.05.002. arXiv: 1505.06055.

Völk, H. J. & Bernlöhr, K. (2009). *Imaging very high energy gamma-ray telescopes*. In: *Experimental Astronomy*, 25, pp. 173–191.

Weniger, C. (2012). *A tentative gamma-ray line from Dark Matter annihilation at the Fermi Large Area Telescope*. In: *JCAP*, 8, 007. DOI: 10.1088/1475-7516/2012/08/007. arXiv: 1204.2797.

Wilks, S. S. (1938). *The Large-Sample Distribution of the Likelihood Ratio for Testing Composite Hypotheses*. In: *Annals Math. Statist.* 9 (1), pp. 60–62. DOI: 10.1214/aoms/1177732360.

Zwicky, F. (1933). *Die Rotverschiebung von extragalaktischen Nebeln*. In: *Helvetica Physica Acta*, 6, pp. 110–127.

Zwicky, F. (1937). *On the Masses of Nebulae and of Clusters of Nebulae*. In: *Astrophys. J.* 86, p. 217. DOI: 10.1086/143864.

Acknowledgements

Hier sitze ich vor der fast fertigen Arbeit. Die Analyse ist vollendet, Plots gemacht und die letzten Absätze geschrieben. Es war ein langer Weg, etwas mehr als vier Jahre hat es gedauert, um ans Ziel zu kommen und endlich ist es soweit.
Aber wie ein weiser Mensch einst sagte: „Es geht nicht darum das Ende des Weges zu erreichen, sondern um die Freunde, die wir unterwegs finden."
Ich denke, ich habe viele Freunde in meiner Zeit hier am ECAP gefunden und viele Menschen, denen ich sehr dankbar bin, dass sie mich über all die Jahre begleitet haben. Ihr wart für mich da, wenn der Weg einer Geröllhalde glich, unterstützend und aufmunternd. Aber auch an den schönen Stellen, wenn es wie ein abendlicher Spaziergang am Strand war, fröhlich und ausgelassen.

Allen voran möchte ich Christopher danken, da er mir ermöglicht hat, diese Reise anzutreten. Danke für die vielen Diskussionen, die nicht immer nur um Dunkle Materie gingen, sondern manches Mal auch über triviale Dinge des Lebens.
Liebe γ-Gruppe, ihr seid ein toller Haufen. Wenn ich fachliche Probleme hatte, wart ihr immer da und habt euch Zeit zum Diskutieren genommen, allen voran sind hier Lars, Ira und Susanne zu nennen. Aber natürlich hat es sich bei uns nicht immer nur um die Arbeit gedreht, und so hatten wir viele interessante Unterhaltungen, egal ob bei Kaffee, in der Mittagspause oder einfach auf dem Flur, weil sich zufällig die Wege gekreuzt haben.
Bedanken möchte ich mich auch bei meinen Kollegen aus der Admingruppe; ich habe unglaublich viel bei euch lernen können und immer viel Freude an der abwechslungsreichen Arbeit gehabt, allen voran bei dir, Kay, du hattest immer ein offenes Ohr und eine helfende Hand, wenn ich mal wieder ein Problem mit einem unserer Server hatte.
Ich möchte mich auch bei meinen ehemaligen und aktuellen Bürokollegen bedanken. Alex, André, Katrin, Philipp, Carolin und Susanne. Ich war bestimmt nicht immer ein leichter Schreibtischnachbar. Danke für all die schönen Erinnerungen: Stundenlanges Kartenspielen, angeregte Diskussionen und zahlreiche Pilgerungen zur Kaffeemaschine.
Besonders hilfreich auf meinem Weg waren auch unsere Sekretärinnen Gabriele Eckner und Monika Fink. Ohne euch wäre ich mit Sicherheit an einem der vielen Formulare gescheitert.
2015 hatte ich einen kleinen Umweg eingeschlagen, da ich nach Namibia an die Teleskope durfte – es war eine großartige Zeit mit vielen interessanten Begegnungen. Danke Susana, Tim und der Crew in Namibia, ich denke gerne an die gemeinsamen BBQs und Sundowner zurück.
Auf den letzten Metern hab ich dankenswerterweise sehr viel Unterstützung in Form von Korrekturlesen erhalten, hier sind vor allem Ira, Lars, Susanne, Giacomo, Hildegard und Sebastian zu nennen. Danke für das Glattziehen von Formulierungen und Ausmerzen von Tippfehlern.
Danken möchte ich auch allen Freunden, die mir durch Dinge wie sportliche Aktivitäten, Spieleabende und gemeinsame Urlaube die nötige Ausdauer gegeben haben.
Zum Schluss möchte ich noch meinen Eltern und Geschwistern danken. Ihr wart immer für mich da, egal was ich gebraucht habe. Danke!

Danke euch allen und all denjenigen, die ich vergessen habe, namentlich zu erwähnen – ohne euch hätte ich es nicht geschafft, den Weg so weit zu gehen.

Erklärung

Hiermit bestätige ich, dass ich diese Arbeit selbstständig und nur unter Verwendung der angegebenen Hilfsmittel angefertigt habe.

Erlangen, den 19. Juli 2018

Johannes Veh